UNIVERSITÀ DEGLI STUDI DI ROMA
"TOR VERGATA"

FACOLTÀ DI SCIENZE MATEMATICHE, FISICHE E NATURALI
Dipartimento di Fisica

RPCs as trigger detector for the ATLAS experiment: performances, simulation and application to the level-1 di-muon trigger

Tesi di dottorato di ricerca in Fisica

presentata da

Andrea Di Simone

Relatori

Prof. *Rinaldo Santonico*

Prof.ssa *Anna Di Ciaccio*

Coordinatore del dottorato

Prof. *Piergiorgio Picozza*

Ciclo XVII

Anno Accademico 2003-2004

Contents

Introduction

The Large Hadron Collider is the proton-proton collider in construction at CERN. It will provide the highest ever realized energy in the center of mass, reaching the value of $\sqrt{s} = 14TeV$, thus giving the possibility to investigate a wide range of physics up to masses of $\sim 1TeV$. The most prominent issue is the search for the origin of the spontaneous symmetry-breaking mechanism in the electroweak sector of the Standard Model. ATLAS will be one of the four experiments installed at the LHC. It has been designed to be a general purpose experiment, and among its characteristics it has a large stand-alone muon spectrometer, which allows high precision measurements of the muon momentum. A general overview of the ATLAS experiment and of its muon spectrometer is given in chapters 1 and 2.

In the muon spectrometer different detectors are used to provide trigger functionality and precision momentum measurements. In the pseudorapidity range $|\eta| \leq 1$ the first level muon trigger is based on Resistive Plate Chambers, gas ionization detectors which are characterized by a fast response and an excellent time resolution $\sigma_t \leq 1.5ns$. The working principles of the Resistive Plate Chambers will be illustrated in chapter 3.

Given the long time of operation expected for the ATLAS experiment (~10 years), ageing phenomena have been carefully studied, in order to ensure stable long-term operation of all the subdetectors. Concerning Resistive Plate Chambers, a very extensive ageing test has been performed at CERN's Gamma Irradiation Facility on three production chambers. The results of this test are presented in chapter 4.

One of the most commonly used gases in RPCs operation is $C_2H_2F_4$ which, during the gas discharge can produce fluorine ions. Being F one of the most aggressive elements in nature, the presence of F^- ions on the plate surface is dangerous for the integrity of the surface itself. For this reason a significant effort has been put in the last years to understand the mechanisms of F^- production in RPCs

operated with $C_2H_2F_4$-based gas mixtures. The results of the measurements performed in the INFN-Roma2 ATLAS laboratories, in collaboration with the Dept. of Science and Chemical Technology of the Univeristy of Rome "Tor Vergata", are presented in chapter 5.

The old Geant3 software toolkit, which has been the *de facto* standard for high energy physics simulation in the last 15 years, is being progressively replaced by the completely re-written toolkit Geant4. The migration from Geant3 to Geant4 has required, in the case of the ATLAS experiment, a re-writing from scratch of most of the simulation software. In chapter 6 the work done on RPC Geant4 simulation will be described.

Many interesting physics processes to be observed in ATLAS will be characterized by the presence of pairs of muons in the final state. For this reason, the ATLAS first level muon trigger has been designed to allow to select di-muon events. While foreseen in the design of the trigger system, this possibility was never intensively tested with the final detector layout. In chapter 7 the first results of such a test will be summarized.

Chapter 1

The ATLAS experiment

1.1 The Large Hadron Collider

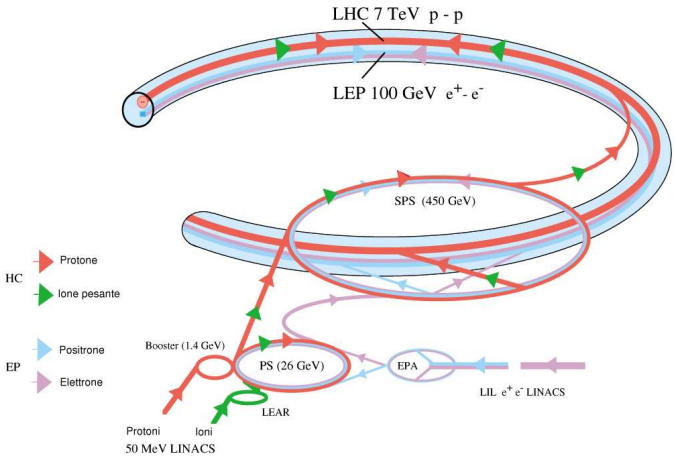

Figure 1.1: The LHC accelerator chain

The Large Hadron Collider (LHC), is a circular accelerator being built at CERN [1]. It will be hosted in the LEP tunnel, and will accelerate in two separate rings two proton beams up to a center of mass energy of 14 TeV. The machine is also designed to provide heavy ion collisions (Pb-Pb) at an energy of 1150 TeV in the center of mass, corresponding to 2.76 TeV/u and 7.0 TeV per charge. The design luminosity for pp operation is $10^{34} cm^{-2} s^{-1}$, and by modifying the existing antiproton ring (LEAR) into an ion accumulator, the peak luminosity in Pb-Pb operation can reach $10^{27} cm^{-2} s^{-1}$. Figure 1.1 shows a schematical view of the layout

of the machine. The two particle beams can cross in only four points (thus making their path length identical), which will therefore be the four collision points available for experiments. At the crossing point the angle between the beams will be $200\mu rad$.

The two high luminosity insertions in point 1 and point 5, diametrically opposed, will host the experiments ATLAS and CMS respectively. Two more experiments, one aimed at the study of heavy ions collisions (ALICE) and one designed to perform accurate studies on B physics (LHCb) will be located in point 2 and point 8.

***p-p* operation.** The beams in the LHC will contain 2835 bunches of 10^{11} protons each per beam. The existing CERN accelerator chain, illustrated in figure 1.1, will be used as injection system for the LHC. The bunches, with an energy of 26 GeV are formed in the PS, and are characterized by a 25ns spacing. Three trains of 81 bunches, corresponding to a total charge of 2.43 10^{13} protons, are then injected in the SPS on three consecutive PS cycles, thus filling 1/3 of the SPS circumference. The resulting beam is accelerated to 450 GeV before being transferred to the LHC. This cycle has to be repeated 12 times in order to fill both the LHC counter-rotating beams.

Heavy ion operation. In the case of Pb-Pb beams, the optimal bunch spacing would be 134.7ns at the LHC collision energies. In order to permit the proton experiments to trigger ion collisions, and ALICE to trigger on protons, it was decided to reduce this spacing to 125ns, which is multiple of the 25ns spacing used in proton operation. The primary source of ions is a lead linac, producing, at a rate of 10 Hz, a 60μs, 22μA pulse of Pb^{54+} at 4.2 MeV/u. Each pulse is injected in LEAR, where it is cooled in 0.1 s using electron cooling. After the injection of 20 pulses the beam, containing 1.2 10^{19} ions divided in four batches, is accelerated to 14.8 MeV/u and then sent to the PS. In the PS the four bunches, occupying a quarter of the machine's circumference, are accelerated to a momentum of 6.15 GeV/c/u, and the bunch spacing is tuned at 125 ns. The four bunches are transferred to the SPS in one single batch, and 13 consecutive such batches are stored in succession in the SPS, accelerated and then injected in the LHC. The injector cycle uses 152 PS cycles, 12 SPS cycles for a total filling time of 9.8 min for each LHC ring.

1.2 The Higgs boson at LHC

As shown in figure 1.3 the total production cross section for a Higgs boson is greater than $100\,fb$ in all its estimated mass range. This implies that in one year of data taking at the LHC more than 10^3 Higgs events will be produced at low luminosity and more than 10^4 during high luminosity operation. Figure 1.2 shows the Feynman diagrams of the principal production mechanisms for the Higgs boson.

The gluon fusion process has the highest cross section over all the mass range. For $m_H \sim 1TeV$ the Z or W fusion process becomes comparable with the gluon fusion. The production associated with a pair has smallest cross sections, but the decay channels of the top quark or of the W or Z boson can generate very clean experimental signatures.

The coupling of the Higgs boson to a particle has a dependence on the mass of the particle. As a consequence, the branching ratios of the Higgs are highest for decays in heavy particles. Figure 1.4 shows the branching ratios of the Higgs as a function of m_H. The Higgs decay channels, their backgrounds and their signatures can be summarized as follow, as a function of m_H:

- $m_H < 130GeV$. In this mass region $H \to b\bar{b}$ is the most favorite channel, being the $b\bar{b}$ the heaviest fermion pair accessible to the Higgs. This decay channel is affected by the background of $b\bar{b}$ coming from other processes. The associated production channels can be studied through the identification of the leptons produced in the decays of the t or of the W or Z bosons.
  The channel $H \to \gamma\gamma$ is rarer, but it has a clear experimental signature: these events are characterized by two isolated photons with high p_T. Its detection requires a good identification of photons and and a high energy resolution. The background for this channel is mainly due to $q\bar{q} \to \gamma\gamma$ and $gg \to \gamma\gamma$ processes.

- $130GeV < m_H < 2m_Z$. One of the most promising channels in this region is $H \to ZZ^* \to 4l$. The background for this kind of processes come from $t\bar{t} \to Wb + W\bar{b} \to l\nu + l\nu\bar{c} + l\nu + l\nu c$ and $Zb\bar{b} \to 4l$, and can be reduced requiring at least a pair l^+l^- with a mass compatible with m_Z and rejecting events with secondary vertices.
  At $m_H = 170GeV$ the dominant decay channel becomes $H \to WW^*$. In this case the signal $H \to WW^* \to l\nu l\nu$ will be studied, thus requiring a good resolution in transverse missing energy.

- $m_H \geq 2m_Z$. At these masses, the channel $H \rightarrow 4l$ becomes accessible. It has an extremely clean signature, thanks to the high p_T of the four leptons. At $m_H > 600GeV$, also the channels $H \rightarrow ZZ \rightarrow llνν$ and $H \rightarrow WW \rightarrow lν\,jet\,jet$ can be studied.

1.3 The ATLAS experiment

ATLAS (A Toroidal Lhc Apparatus) is one of the four experiments to be installed at the LHC. One of the main physics issues that the center of mass energy of the LHC will allow to investigate is the origin of the spontaneous symmetry-breaking mechanism in the electroweak sector of the Standard Model (SM). This symmetry-breaking is expected to cause the existence of a SM Higgs boson, or of a family of Higgs particles ($H^{\pm}$, h, H and A) if the Minimal Supersymmetric Standard Model (MSSM) is considered. The design of the ATLAS detector was therefore optimized to allow the identification of Higgs particles. Table 1.3 shows the Higgs main decay channels as a function of m_H. The MSSM predicts similar decays channels, plus processes as the one shown in table 1.3.

Decay channel	mass range	comments
$H \rightarrow bb$	$80 < m_H < 100GeV$	from WH, ZH and $t\bar{t}H$ using a $l^{\pm}$ tag and b-tagging
$H \rightarrow \gamma\gamma$	$90 < m_H < 150GeV$	
$H \rightarrow ZZ^* \rightarrow 4l$	$130 < m_H < 2m_Z$	
$H \rightarrow ZZ \rightarrow 4l$, $2l2\nu$	$m_H > 2m_Z$	
$H \rightarrow WW, ZZ \rightarrow$ $\rightarrow l\nu$ 2 jets, $2l$ 2 jets	up to 1 TeV	from WW, ZZ fusion using tagging of forward jets

Table 1.1: Higgs decay channels, as predicted by the SM

Decay channel		comments
$A \rightarrow \tau^+\tau^-$	$\rightarrow e\mu$ plus ν 's	
	$\rightarrow l$ plus hadrons plus ν 's	
$H^{\pm}$	$\rightarrow \tau^{\pm}\nu$	from $t\bar{t} \rightarrow H^{\pm}W^{\mp}b\bar{b}$ and
	$\rightarrow$ 2 jets	using an $l^{\pm}$ tag and b-tagging

Table 1.2: Examples of Higgs decay channels, as predicted by the MSSM

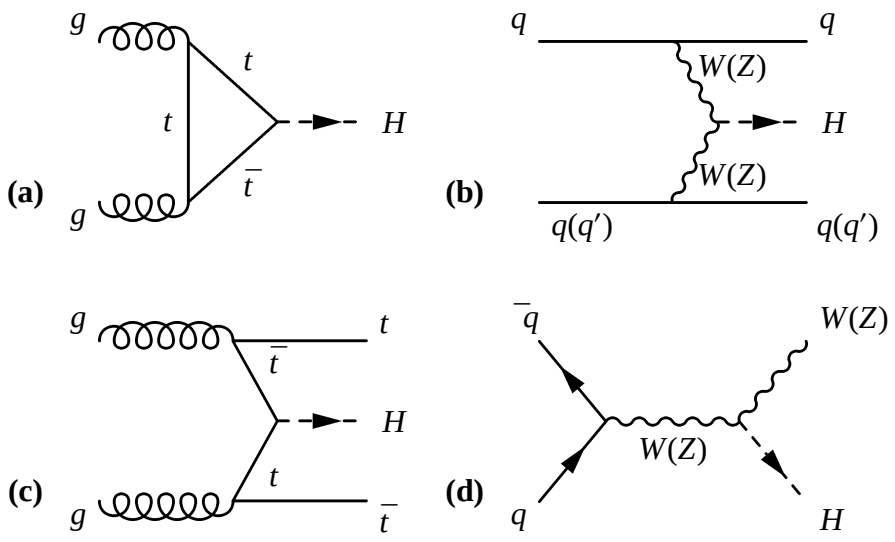

Figure 1.2: Feynman diagrams of the main production processes of the Higgs boson: gluon fusion (a), Z or W fusion (b), production associated with a $t\bar{t}$ pair (c) or with a Z or W boson (d).

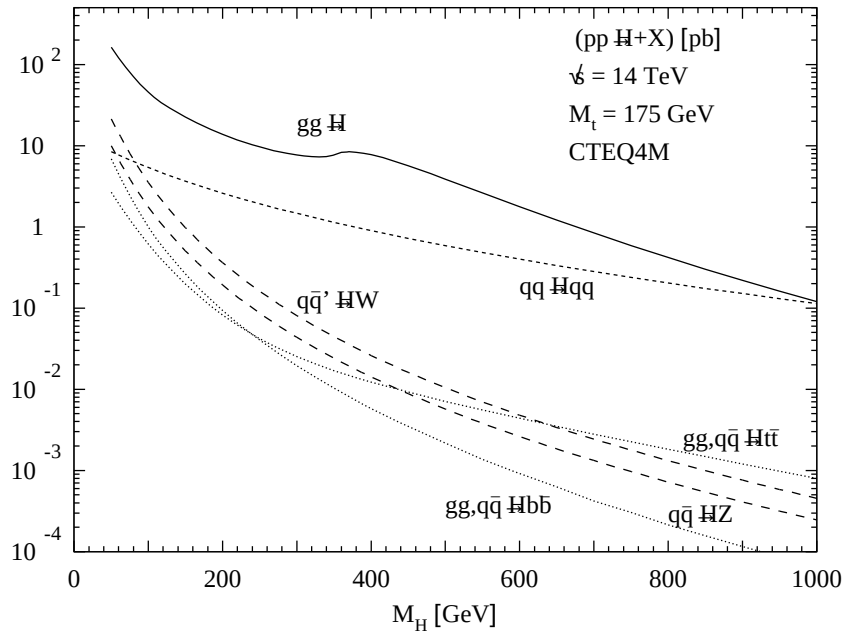

Figure 1.3: Production cross sections for the Higgs boson at LHC as a function of the mass of the boson.

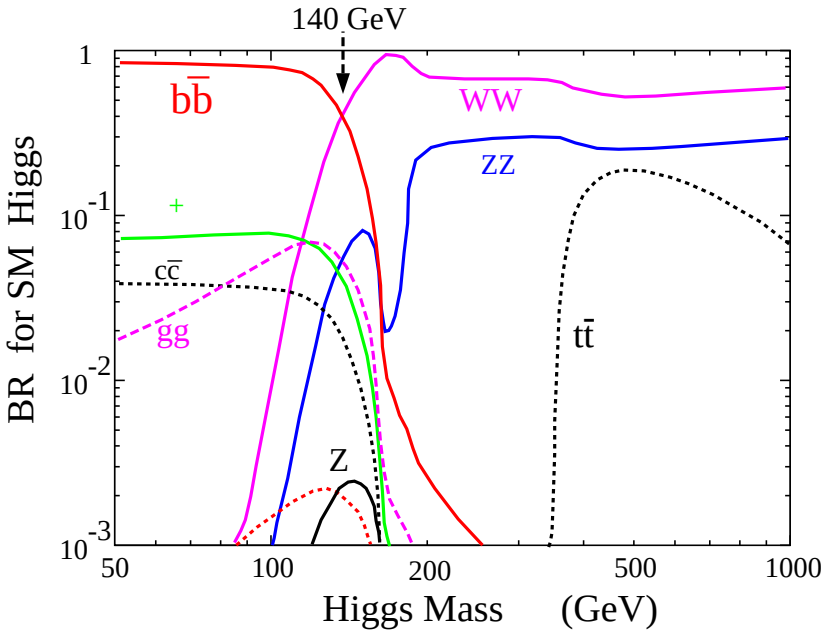

Figure 1.4: Higgs branching ratios as a function of the Higgs mass.

Figure 1.5 shows the expected significance of a Higgs signal as a function of m_H.

1.3.1 Glossary

In the ATLAS standard reference frame, the z-axis is oriented along the beam, while the x-y plane is perpendicular to the beam axis. The x positive direction is the one pointing to the center of the LHC, and the y axis is pointing upwards.

The angle measured around the beam axis is called ϕ, or *azimuthal*, and the angle with respect to the beam axis is called θ, or *polar*. The pseudorapidity η is defined as $\eta = -\ln\tan\frac{\theta}{2}$. In the following, transverse momentum (p_T), transverse energy (E_T) and transverse missing energy (E_T^{miss}) refer to the quantities measured in the x-y plane.

The detector is divided along z in three parts: side A is the side with $z > 0$, side C is at $z < 0$ and side B is the plane $z = 0$. Figure 1.6 shows the layout of the subdetectors in the ATLAS experiment.

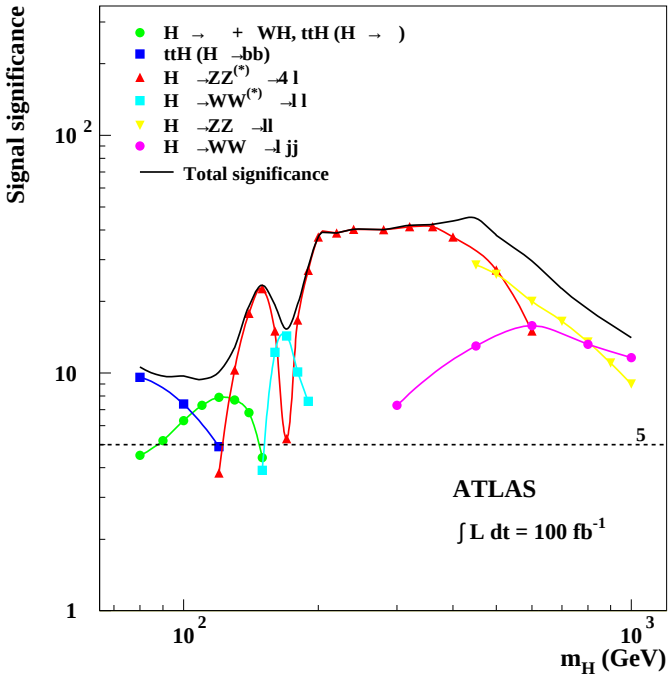

Figure 1.5: Expected discovery potential for the Higgs boson of the ATLAS experiment for an integrated luminosity of $100 fb^{-1}$, as a function of m_H.

1.3.2 Overall design

In order to achieve the necessary sensitivity to the physics processes to be studied at the LHC, the ATLAS detector ha been designed to provide:

- Electron and photon identification and measurements, using a very performant electromagnetic calorimetry.
- Accurate jet and missing transverse momentum measurements, using, in addition to electromagnetic calorimeters, the full-coverage hadronic calorimetry.
- Full event reconstruction at low luminosity.
- Efficient tracking also at high luminosity, with particular focus on high-p_T lepton momentum measurements.
- Large acceptance in pseudorapidity, and almost full coverage in ϕ.

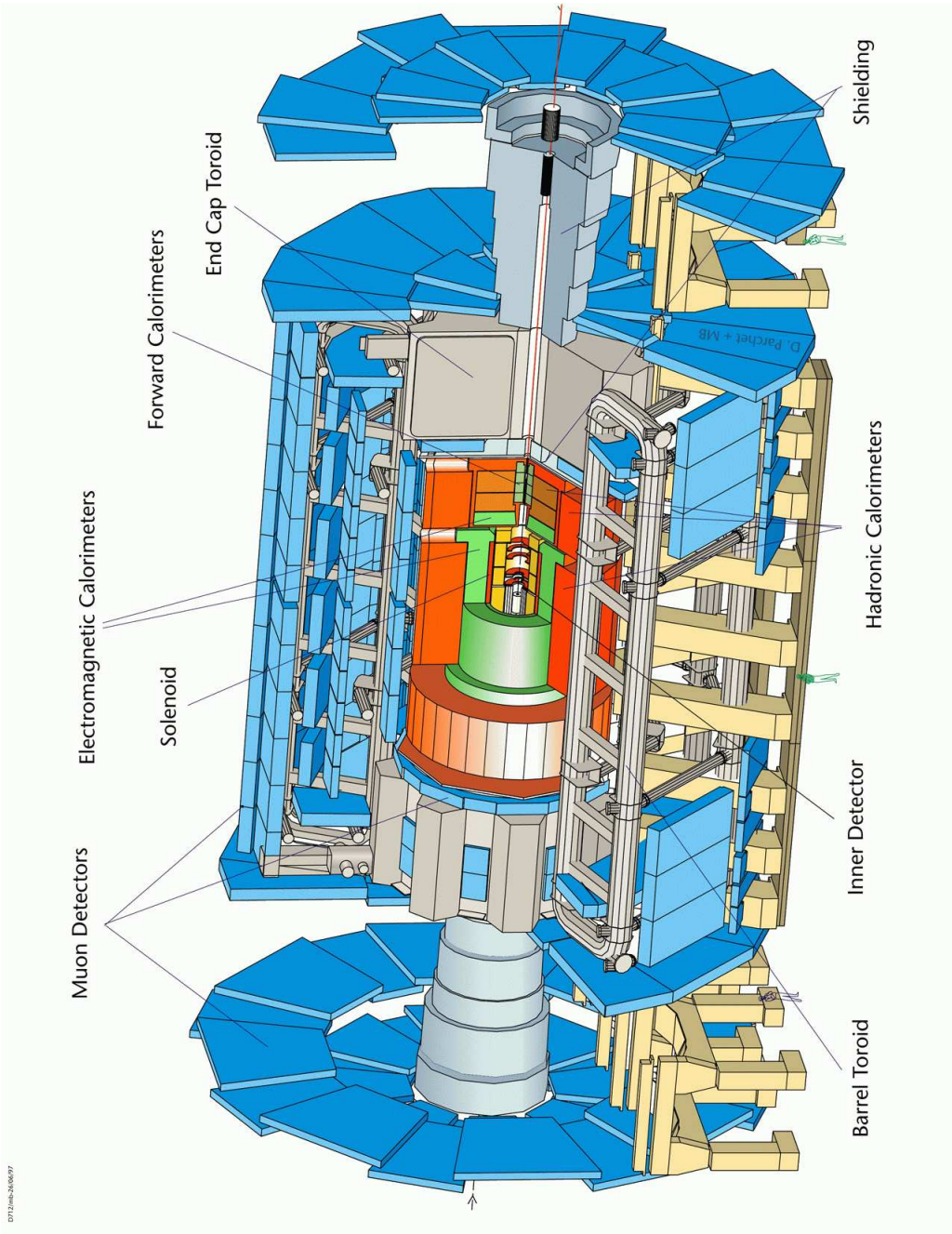

Figure 1.6: The ATLAS detector

A superconducting solenoid generates the magnetic field in the inner region of the detector, while eight large air-core superconducting toroids are placed outside the calorimetric system, and provide the magnetic field for the external muon

spectrometer.

The Magnet System

The overall dimensions of the ATLAS magnet system are $26m$ in length and $22m$ in diameter. In the end-cap region, the magnetic field is provided by two toroid systems (ECT) inserted in the barrel toroid (BT) and lined up with the central solenoid (CS). The CS provides the inner trackers with a field of $2T$ ($2.6T$ at the solenoid surface). Being the CS in front of the calorimetric system, its design was carefully tuned in order to minimize the material and not to produce any degradation of the calorimeter performance. As a consequence of this constraints, the CS and the barrel EM calorimeter share the same vacuum vessel. The operating current of the solenoid is $7.6kA$.

The magnetic field generated by the BT and ECT have peak values of 3.9 and 4.1 T respectively. The eight coils of the BT, as wheel as the 16 coils of the ECT are electrically connected in series and powered by $21kA$ power supply.

The magnets are cooled by a flow of helium a $4.5K$.

All the coils are made of a flat superconducting cable located in an aluminum stabilizer with rectangular shape. The aluminum used in the CS is doped in order to provide higher mechanical strength.

The Inner Detector

The Inner Detector (ID) is entirely contained inside the Central Solenoid, which provides a magnetic field of $2T$. The high track density expected to characterize LHC events calls for a careful design of the inner tracker. In order to achieve the maximum granularity with the minimum material, it has been chosen to use two different technologies: semiconductor trackers in the region around the vertex are followed by a straw tube tracker. Figure 1.7 shows a schematical view of the ID.

The semiconductor tracker is divided in two subdetectors: a pixel detector and a silicon microstrip detector (SCT). The total number of precision layers is limited by the quantity of material they introduce and also because of their cost. In the resulting setup, a track typically crosses three pixel layers and eight SCT layers (corresponding to four space points). The three pixel layers in the barrel have a resolution of $12\mu m$ in $R\phi$ and $66\mu m$ in Z. In the endcaps the five pixel disks on each side provide measurements in $R\phi$ and R with resolutions of $12\mu m$ and $77\mu m$

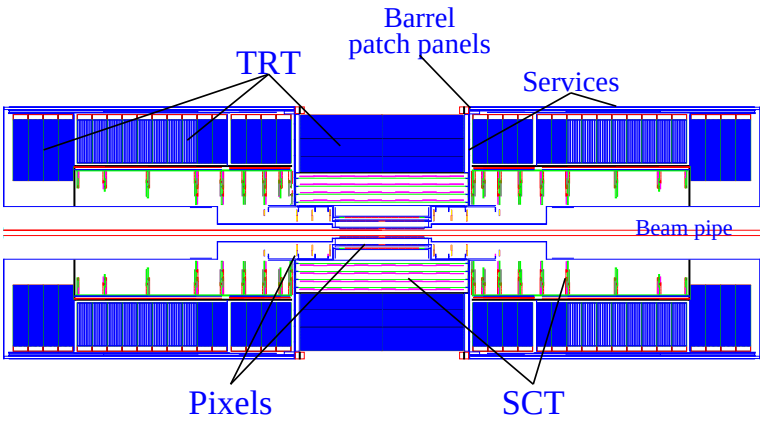

Figure 1.7: ATLAS inner detector

respectively. The innermost layer of pixel detectors in the barrel is placed at about $4cm$ from the beam axis, in order to improve the secondary vertex measurement capabilities.

The SCT detector uses small angle ($40mrad$) stereo strips to measure positions in both coordinates ($R\phi, Z$ for the barrel and $R\phi, R$ for the endcaps). For each detector layer one set of strips measures ϕ. The resolutions obtained in the barrel are $16\mu m$ and $580\mu m$ for $R\phi$ and Z respectively, while in the endcaps the resolutions are $16\mu m$ in $R\phi$ and $580\mu m$ in R.

The straw tubes are parallel to the beam in the barrel while in the endcaps they are placed along the radial direction. Each straw tube has a resolution of $170\mu m$, and each track crosses about 36 tubes. In addition to this, the straw tube tracker can also detect the transition-radiation photons emitted by electrons crossing the xenon-based gas mixture of the tubes, thus improving the ATLAS particle identification capabilities.

The EM Calorimeter

The EM calorimeter is divided in three parts: one in the barrel ($|\eta|$<1.7) and two in the endcaps (1.375 < $|\eta|$<3.2). The barrel calorimeter is divided in two half barrels, with a small ($6mm$) gap between them at $z = 0$. The endcap calorimeters are made up of two coaxial wheels each. The layout of the EM calorimeter, together with the hadronic one, is illustrated in figure 1.8.

The EM calorimeter is a Liquid Argon detector with lead absorber plates and Kapton electrodes. In order to provide a full coverage in ϕ, an accordion geometry

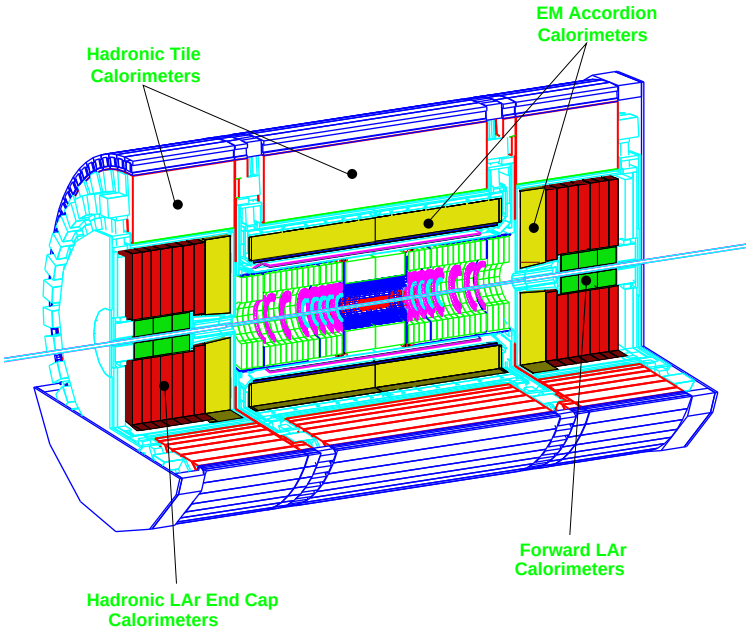

Figure 1.8: The ATLAS calorimeters

was chosen for the internal flayout of the calorimeter. The lead absorber layers have variable thickness as a function of η and has been optimized to obtain the best energy resolution. The LAr gap on the contrary has a constant thickness of $2.1mm$ in the barrel. The total thickness is $>24X_0$ in the barrel and $>26X_0$ in the endcaps.

In the region with $|\eta| < 2.5$ the EM calorimeter is longitudinally divided in three sections. The first region, is meant to work as a preshower detector, providing particle identification capabilities and precise measurement in η. It has a thickness of $\sim 6X_0$ constant as a function of η, is read out with strips of $4mm$ in the η direction.

The middle section is divided into towers of size $\Delta\phi \times \Delta\eta = 0.025 \times 0.025$ ($\sim 4 \times 4cm^2$ at η=0) with square section. At the end of this section the calorimeter has a total thickness of $\sim 24X_0$. The third section has a lower granularity in η (~ 0.05).

The calorimeter cells point towards the interaction region over the complete

η range, and the total number of channels is $\sim$ 190000. A schematic layout of a calorimeter cell is shown in figure 1.9.

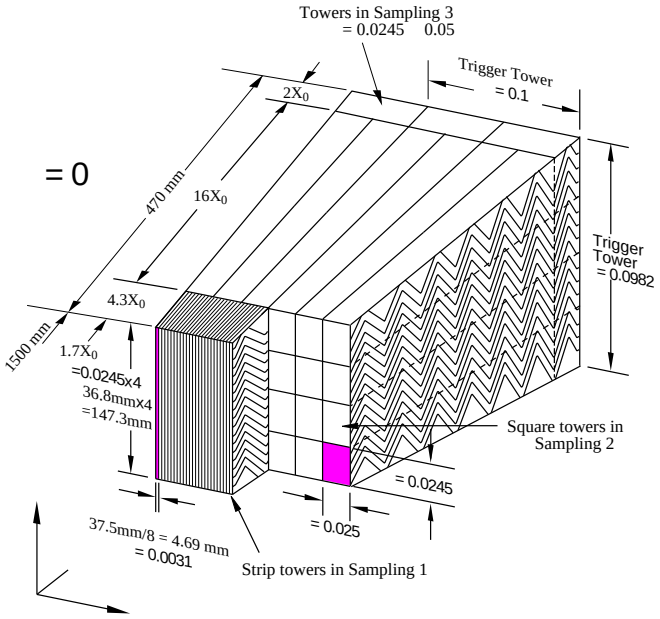

Figure 1.9: Schematic layout of an ATLAS accordion calorimeter cell.

The Hadronic Calorimeter

The region with $|\eta| < 4.9$ is covered by the hadronic calorimeters using different techniques, taking into account the varying requirements and radiation environment over this large η range. The range $|\eta| < 1.7$, corresponding to the barrel calorimeter, is equipped with a calorimeter (TC) based on the iron/scintillating-tile technology. Over the range $\sim 1.5 < |\eta| < 4.9$, Liquid Argon calorimeters were chosen. In this region the hadronic calorimetry is segmented into an Hadronic End-Cap Calorimeter (HEC), extending up to $|\eta| < 3.2$ and a High Density Forward Calorimeter (FCAL) covering the region with highest $|\eta|$. Both the HEC and the FCAL are integrated in the same cryostat housing the EM end-caps calorimetry. The overall layout of the ATLAS hadronic calorimeters is shown in figure 1.8.

The thickness of the calorimeter has been carefully tuned in order to provide good containment of hadronic showers and reduce to the minimum the punch-through into the muon system. At $\eta = 0$ the total thickness is 11 interaction lengths (λ), including the contribution from the outer support ($\sim 1.5\lambda$). This has

been shown by measurements and simulation to be sufficient to reduce the punch-through to just prompt or decay muons, while 10λ of active calorimeter provide good resolution for high energy jets. This characteristics, together with the large η coverage, will guarantee an accurate E_T^{miss} measurement, which is an important parameter in the signatures of many physics processes.

Tile Calorimeter. In the barrel region the hadronic calorimeter is a sampling calorimeter using iron as the absorber and scintillating tiles as the active material. Radially, it extends from an inner radius $2.28m$ to an outer radius of $4.25m$. The tiles are placed radially and staggered in depth, with a periodic structure along z. The tiles are $3mm$ thick and the total thickness of the iron plates in one period is $14mm$.Both the sides of the scintillating tiles are readout with two separate photo-multipliers. The barrel calorimeter is segmented along z into one barrel part and two extended barrels. It is longitudinally segmented in three layers of 1.4,4.0 and 1.8 λ at $\eta = 0$. Azimuthally, the barrel and the extended barrels are divided into 64 modules.

The readout cells, consisting of fibers grouped into a photomultiplier, are arranged along η with a pseudoprojective geometry, i.e. pointing towards the interaction region. The resulting granularity is $\Delta\eta\times\Delta\phi = 0.1\times0.1$, reduced to 0.2×0.1 in the last layer.

Liquid-argon hadronic end-cap calorimeters. Each HEC consists of two independent wheels, with an outer radius of $2.03m$. The upstream wheel is built with $25mm$ copper plates, separated by a gap of $8.5mm$. The gap is equipped with three parallel electrodes splitting the gap into four drift regions of about $1.8mm$. The central electrode is used for the readout. The wheels farther from the interaction point have the same structure, but with $50mm$ plates.

Liquid-argon forward calorimeter. The FCAL is located in a region where a high lever of radiation is expected. It is integrated into the end-cap cryostat and its front face is at about $4.7m$ from the interaction point. In order to reduce the neutron albedo in the ID cavity, the front face of the FCAL is recessed of $1.2m$ with respect to the EM calorimeter front face. This limitation in space, together with the requirement of 9.5 active interaction lengths, calls for a high density design.

The FCAL consists of three sections: the first one made of copper, the other two of tungsten. In each section, the detector has a structure consisting of a metal matrix with regularly spaced longitudinal channels filled with concentric rods and

tubes. The rods are at positive high voltage, while the tubes and the matrix are grounded. The LAr in the gap between is the sensitive medium.

The Trigger/DAQ system

The ATLAS trigger and DAQ system is described in figure 1.10. The trigger is organized in three levels, called LVL1, LVL2 and EF (Event Filter).

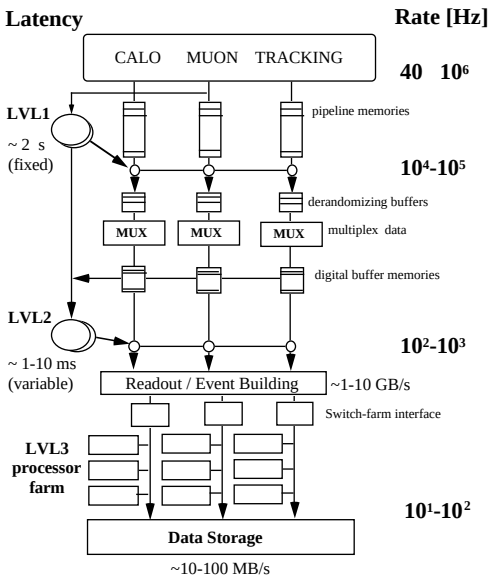

Figure 1.10: Block diagram of the ATLAS Trigger/DAQ system

LVL1 [7] acts on reduced granularity ($\Delta\eta \times \Delta\varphi = 0.1 \times 0.1$) data from the calorimeters and the muon spectrometer; its decision is based on selection criteria of inclusive nature. Example menus are shown on tables 1.3 and 1.4 with the corresponding trigger rate expected at low and high luminosity.

LVL1, whose block diagram is shown in figure 1.11 is divided into four parts: the calorimeter trigger, the muon trigger, the central trigger processor, which is in charge of taking the final decision, and the TTC (Timing, Trigger and Control distribution system), which is responsible for the distribution of the trigger output to the front-end electronics of the subdetectors.

The main task of the LVL1 trigger system is to correctly identify the bunch crossing of interest. In ATLAS this is not a trivial task, since the dimensions of the muon spectrometer imply times of flight larger than $25ns$ and the shape of

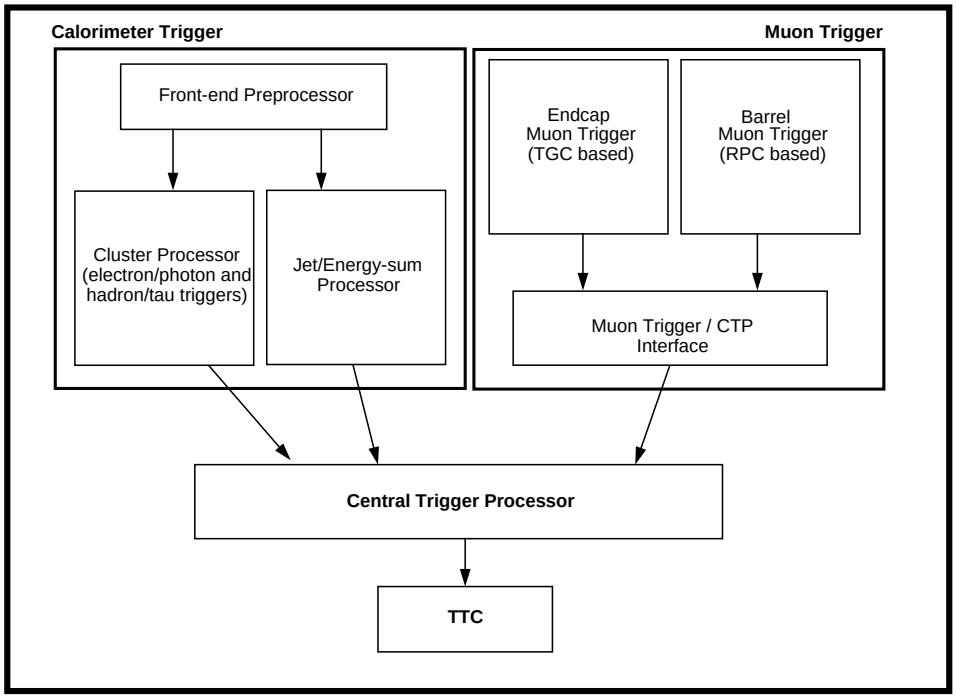

Figure 1.11: Block diagram of the ATLAS LVL1 Trigger system

calorimeter signals extends over many bunch crossings. The LVL1 latency (time spent to take and distribute the decision) is $2\mu s$, with an output rate of $75kHz$, increasable up to $100kHz$ (limit imposed by the design of the front-end electronics).

Events selected by LVL1 are stored in ROBs, Read Out Buffers, waiting for the LVL2 decision. In case of positive decision, events are fully reconstructed and stored for the final decision of the Event Filter. The LVL2 reduces the trigger rate to $1kHz$, using also information from the Inner Detector. It has access to the full data of the event, with full precision and granularity, but its decision is taken considering only data from a small region of the detector, i.e the ROI (Region Of Interest) identified by the LVL1. Depending on the event, the latency of LVL2 can vary from $1ms$ to $10ms$.

The final trigger decision is taken by the Event Filter by means of off-line algorithms; the acquisition rate is required to be less than $100Hz$ for events of $\sim 1Mbyte$.

Table 1.3: Example of LVL1 trigger menu ($L = 10^{34} cm^{-2} s^{-1}$).

Trigger	Rate(kHz)
Single muon, p_t >20 GeV	4
Pair of muons, p_t >6 GeV	1
Single isolated EM cluster, E_t >30 GeV	22
Pair of isolated EM clusters, E_t >20 GeV	5
Single jet, E_t >290 GeV	0.2
Three jets, E_t >130 GeV	0.2
Four jets, E_t >90 GeV	0.2
Jet, E_t >100 GeV AND missing E_t >100 GeV	0.5
Tau, E_t >60 GeV AND missing E_t >60 GeV	1
Muon, p_t >10 GeV AND isolated EM cluster, E_t >15 GeV	0.4
Other triggers	5
Total	≃40

Table 1.4: Example of LVL1 trigger menu ($L = 10^{33} cm^{-2} s^{-1}$).

Trigger	Rate(kHz)
Single muon, p_t >6 GeV	23
Single isolated EM cluster, E_t >20 GeV	11
Pair of isolated EM clusters, E_t >15 GeV	2
Single jet, E_t >180 GeV	0.2
Three jets, E_t >75 GeV	0.2
Four jets, E_t >55 GeV	0.2
Jet, E_t >50 GeV AND missing E_t >50 GeV	0.4
Tau, E_t >20 GeV AND missing E_t >30 GeV	2
Other triggers	5
Total	≃40

Chapter 2

The Muon Spectrometer

One of the most promising signatures of physics at the LHC is the presence of high momentum final state muons. To exploit this potential, the ATLAS detector provides a high resolution muon spectrometer with stand-alone trigger, allowing the high precision measurement of transverse momentum over a wide range of pseudorapidity and azimuthal angle. Figures 2.1 and 2.2 show the conceptual layout of the spectrometer [2]. It is based on the deflection of muon tracks in a system of three large superconducting air-core toroid magnets. In the region with $|\eta| < 1.0$ the magnetic field is generated by a large barrel magnet constructed by eight superconducting coils surrounding the barrel hadronic calorimeter. For $1.4 < \eta < 2.7$ muons are bent by the field produced by two small end-cap magnets inserted at both end of the barrel toroid. In the transition region ($1.0 < \eta < 1.4$) muon bending is provided by a combination of the barrel and end-cap fields.

Physics requirements The muon spectrometer has been designed to provide accurate momentum measurements over a wide energy scale. It will detect the signatures of Standard Model and Supersymmetric Higgs, with the possibility to provide also accurate measurements of low energy muons, such as the ones produced in processes of interest for CP violation studies or B physics. The most important parameters that have been optimized for maximum physics reach are:

- *Resolution.* Momentum and mass resolution at the level of 1% are required for reliable charge identification and for reconstruction of two- and four-muon final states on top of high background levels.

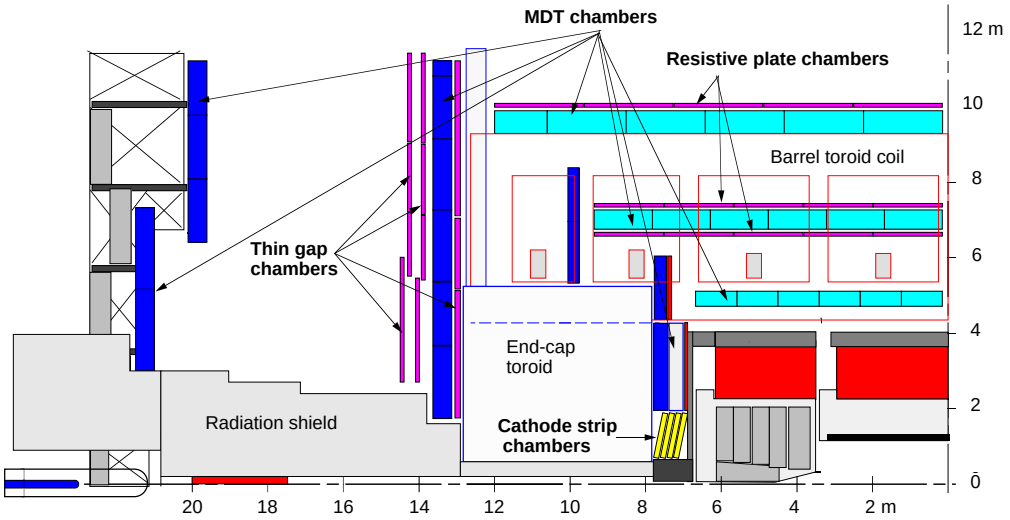

Figure 2.1: Side view of one sector of the muon spectrometer.

- *Second coordinate measurement.* Along the non-bending projections, muon tracks need to be detected with a resolution of 5-10mm in order to obtain a safe track reconstruction.

- *Rapidity coverage.* The pseudorapidity coverage up to $|\eta| \sim 3$, together with the good hermeticity, is important for all physics processes, in particular for rare high-mass processes.

- *Trigger Selectivity.* High mass states, such as the ones that will be studied at the LHC nominal luminosity call for trigger thresholds of 10-20 GeV, while lower thresholds ($\sim$ 5GeV) are necessary to study CP violation and beauty physics.

- *Bunch-crossing identification.* the LHC bunch-crossing interval of 25ns sets the scale for the required time resolution of the first-level trigger system.

Background conditions The expected background can be classified in two categories:

- *Primary background.* This background is principally due to primary collision products penetrating in the spectrometer through the calorimeters, which are correlated in time with the p-p interaction. Sources of primary background are semileptonic decays of light (π,K$\rightarrow \mu$X) and heavy (c,b,t$\rightarrow$

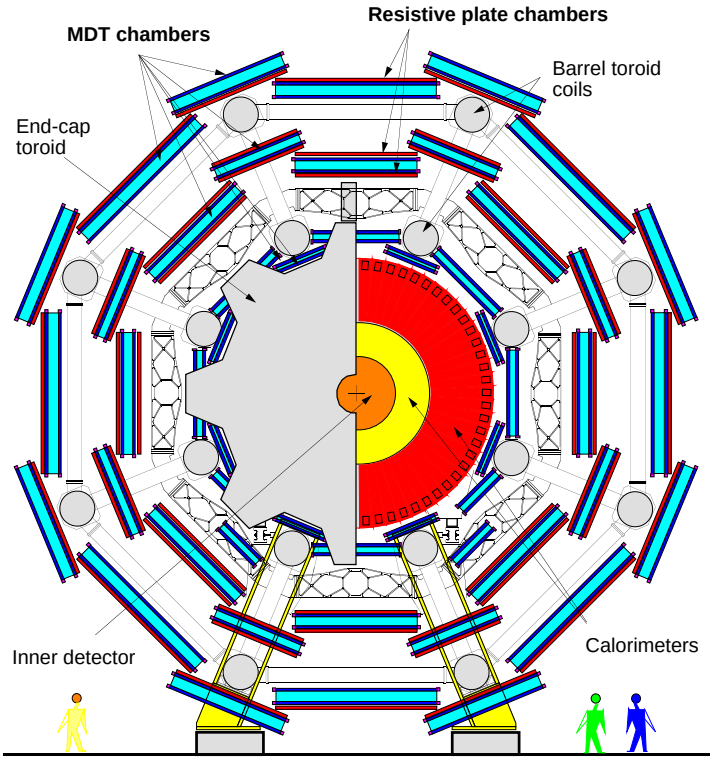

Figure 2.2: Transverse view of the spectrometer.

μX) flavors, gauge bosons decays (W,Z,$\gamma^* \rightarrow \mu$X), shower muons and hadronic punch-through.

- *Radiation background.* This background consist mostly of neutrons and photons in the 1 MeV range, produced by secondary interactions in the forward calorimeter, shielding material, the beam pipe and the machine elements. Low-energy neutrons, which are an important component of the hadronic absorption process, escape the absorber and produce a gas of low-energy photon background through nuclear n-γ processes. This background enters the spectrometer from all directions and is no more correlated in time with the bunch crossing.

Figures 2.4 and 2.3 show the inclusive muons cross sections as a function of transverse momentum and the expected counting rate in the three stations of precision chambers respectively, calculated at the nominal LHC luminosity L=$10^{34} cm^{-2} s^{-1}$. These results, combined with occupancy considerations, guided the choice of precision chambers granularities. Due to the significant uncertain-

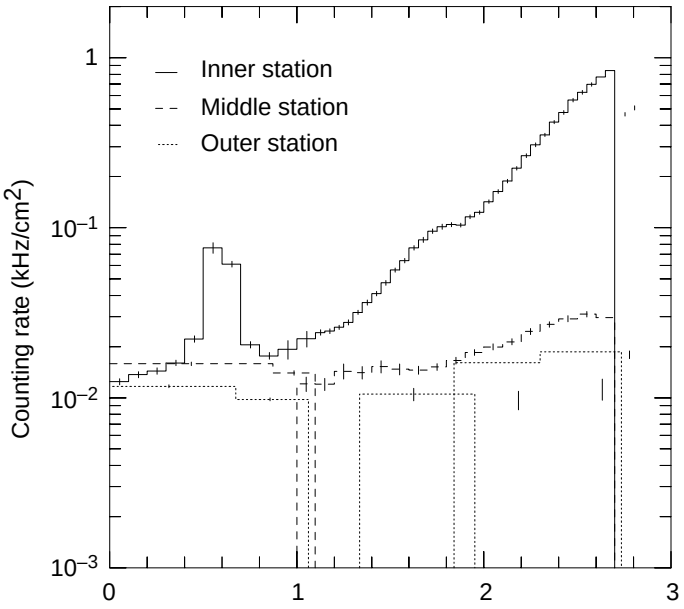

Figure 2.3: Transverse momentum dependence of inclusive muons cross sections

ties affecting the background rates calculations, a safety factor of five has been applied to all calculated quantities before using them in the detector design.

Detector layout Figure 2.5 shows the overall layout of the muon chambers in the ATLAS experiment. The positioning of the chambers is optimized for good hermeticity, and particles from the interaction point traverse at least three stations of chambers [2]. In the barrel, particles are measured at the boundaries of the magnetic field and inside the field volume, in order to determine the momentum from the measurement of the sagitta of the trajectory. For $|\eta| < 1.4$, in the end-caps, the magnet cryostats do not allow the positioning of chambers inside the field volume, and the chosen solution is to arrange the chambers in order to determine the momentum with a point-angle measurement. In the barrel, the chambers are arranged such that they form three cylinders, concentric with the beam axis, at radii of about 5, 7.5 and 10m and covering the range $|\eta| < 1$ The end-cap chambers, covering the range $1 < |\eta| < 2.7$, are arranged in four disks, concentric with the beam axis, at 7, 10, 14 and 21-23m from the interaction point. The combination of barrel and end-cap chambers provides almost complete coverage in η except for the openings at $\eta = 0$ for the passage of cables and services.

The barrel chambers are arranged in projective towers. Within each tower,

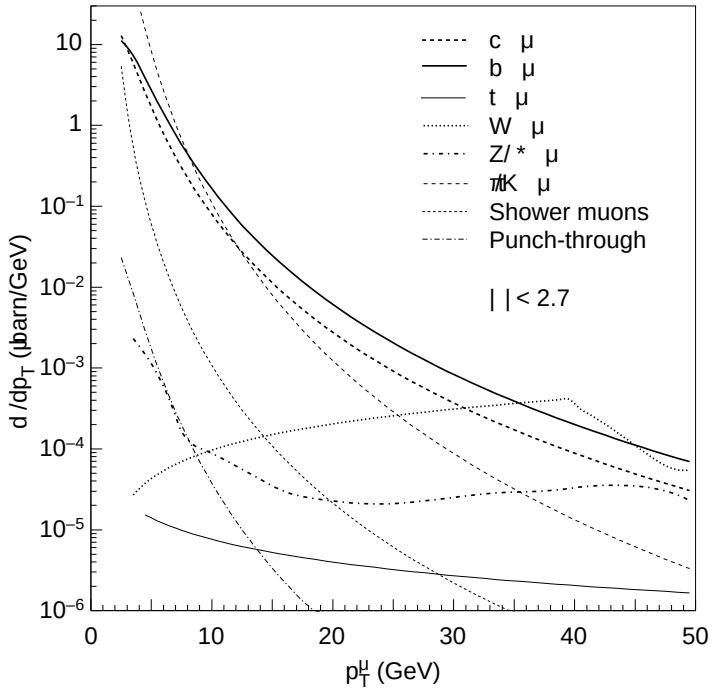

Figure 2.4: Expected counting rates in the three stations of precision chambers, as a function of η.

chambers are connected by alignment rays, monitoring the relative chamber positions. Particles are measured in 2×4 sensitive layers in the inner station and in 2×3 layers each in the middle and outer stations. The spectrometer is azimuthally segmented in 16 sectors, following the eightfold symmetry of the magnet structure.

Monitored Drift Chambers (MDTs) are used for precision measurement of muon tracks in all the spectrometer, except in the innermost ring of the inner station of the end-caps, where particle fluxes are highest, and the precision detector consists of Cathode Strip Chambers (CSCs).

The trigger is provided by three stations of Resistive Plate Chambers (RPCs) in the barrel region, and by three stations of Thin Gap Chambers (TGCs)

Table 2 summarizes the overall characteristics of the muon instrumentation.

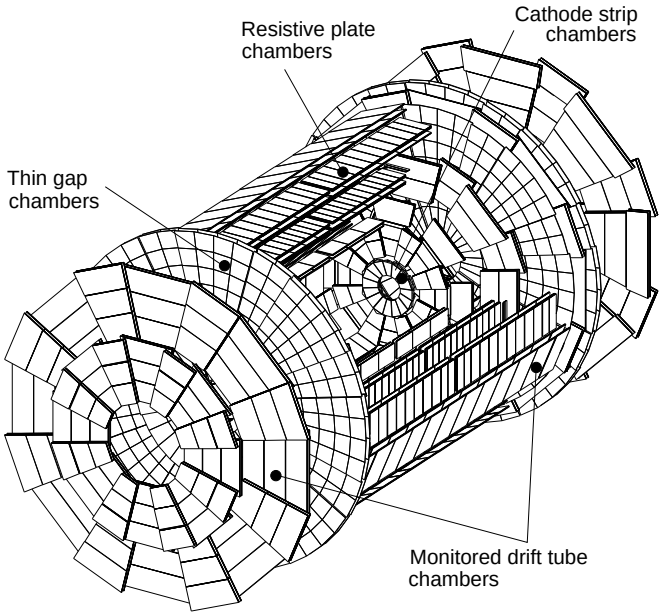

Figure 2.5: Three-dimensional view of the muon spectrometer chambers layout.

2.1 Precision chambers

The muon spectrometer has been designed to allow momentum measurements with a precision $\Delta p_T/p_T < 10^{-4} \times p/GeV$ for p_T>300 GeV. At lower energies, the resolution is limited to a few percent by multiple scattering and by energy loss fluctuation in the calorimeters. Being necessary to obtain such a precision by means of three-point measurements, each point need to be measured with an accuracy better than $50\mu m$. In addition to this requirement, chamber design must guarantee stability of operation for the entire lifetime of the ATLAS experiment, also considering the irradiated environment. Moreover, the total surface to be covered ($\sim 5000m^2$) calls for particular attention to the price of the technologies to be used.

Every muon track coming from the interaction point is measured at least by three stations. Precision measurements are made along the bending direction of the magnetic field by MDTs in all the spectrometer except in the first station in the end-cap and for $\eta > 2$, where the rate and background conditions guided the

	Precision Chambers		Trigger Chambers	
	CSC	MDT	RPC	TGC
Number of chambers	32	1194	596	192
Number of readout channels	67000	370000	355000	440000
Area covered (m^2)	27	5500	3650	2900

Table 2.1: Overview of the muon chamber instrumentation

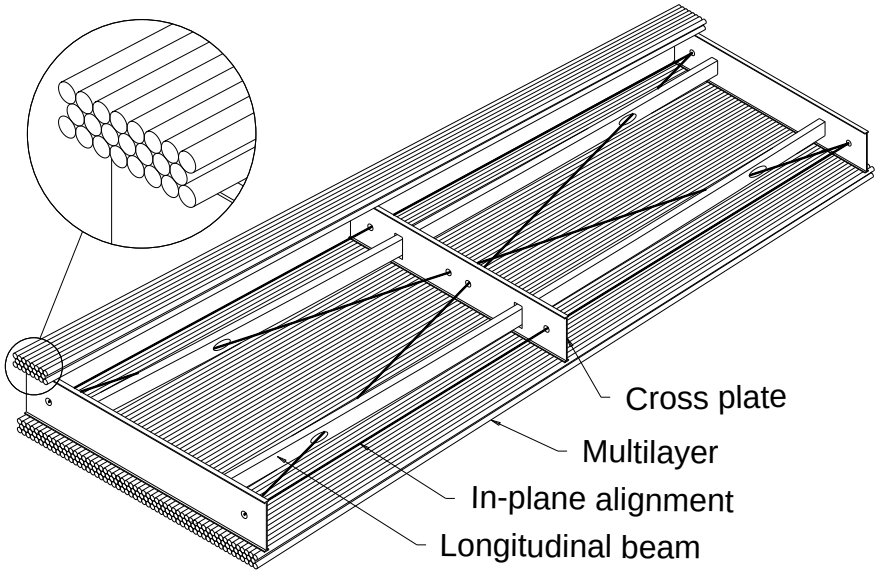

Figure 2.6: Schematic diagram of an MDT.

choice of CSCs.

2.1.1 Monitored Drift Chambers

MDT chambers are made of aluminum tubes of 30*mm* diameter and 400μm wall thickness, with a central 50μm diameter W-Re wire [4] [5]. The tubes are arranged in 2×4 monolayers for the inner stations and 2×3 monolayers for the medium and outer stations. A schematical view of the structure of an ATLAS MDT is shown in figure 2.6. This design allows to improve the single-wire precision and provides the necessary redundancy for track reconstruction. The two multilayers of each station are placed on either side of a special support structure (spacer), providing accurate positioning of the tubes with respect to each other. The support structure also slightly bends the tubes of the chambers which are not

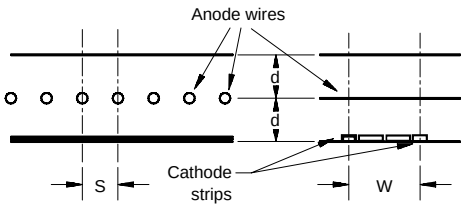

Figure 2.7: Schematic diagram of a Cathode Strip Chamber.

in a vertical position, compensating the gravitational sag of the wires. Most of the components of the alignment system are also mounted on the spacers: once the chambers are installed in the ATLAS detector, all their deformations will be monitored (hence their name) by an in-plane optical system.

Each tube is read out at one end and by a low impedance current-sensitive preamplifier whose threshold is set to a value five times above the noise level. The signal is then processed by a differential amplifier, a shaping amplifier and a discriminator. The leading edge time of the signal can vary as a consequence of charge fluctuations (time slewing). This is why a simple ADC also receives the output of the shaper, allowing for the use of the charge-integrated signal to correct the time slewing. Finally, the signals are sent to TDCs which measure the drift time with a $300ps$ RMS resolution. When a level-1 trigger is asserted, TDC data are transferred over fast serial links to readout drivers.

The magnetic effect on the drift-time drift-distance relation (r-t) is due to a small deviation from the radial drift. The resulting corrections are applied to the r-t relations computed via an 'auto calibration' algorithm.

2.1.2 Cathode Strip Chambers

The large diameter of the tubes of the MDTs make them unsuitable for use in areas where high counting rates ($>200Hz/cm^2$) are expected. Such rates are indeed encountered in the first endcap muon measuring station. In this region, the detector used for precision momentum measurement consists of Cathode Strip Chambers (CSCs) [2].

They are multiwire proportional chambers with a cathode strip readout providing, using charge interpolation, a spatial resolution of $80\mu m$. CSCs cover, in the endcap, the region corresponding to $2 < |\eta| < 2.7$. They are located at approximately $7m$ from the interaction point, occupying the radial space between 881 and $2081mm$.

Figure 2.7 shows a schematic view of a CSC. The anode-cathode spacing d is equal to the anode wire pitch S, which has been fixed at $2.54mm$. The cathode readout pitch W is $5.08mm$. In a typical multiwire proportional chamber signals on the anode wires are read out, thus limiting the spatial resolution to $S/\sqrt{12}$. In a CSCs a higher precision can be achieved measuring the charge induced on the segmented cathode by the avalanche formed on the anode wire.

2.2 Trigger Chambers

The three main requirements of the muon spectrometer trigger system are:

- *Bunch crossing identification.* In order to correctly associate a trigger to a bunch crossing, the trigger detectors must have a time resolution better than the LHC bunch spacing of $25ns$.
- p_T *thresholds*. The need for well defined p_T cut-offs in moderate magnetic fields, calls for a granularity of the order of $1cm$.
- *Second coordinate measurement*. The trigger chambers must provide the measurement of the coordinate orthogonal to the one measured in the precision chambers, with a typical resolution of 5-10mm.

To fulfill these requirements optimizing also the total cost of the system, it has been chosen to use two different technologies: Resistive Plate Chambers in the barrel and Thin Gap Chambers in the endcaps.

2.2.1 Thin Gap Chambers

The structure of Thin Gap Chambers (TGCs) is very similar to the one of multiwire proportional chambers, with the difference that the anode-to-anode distance is larger than the anode-cathode one. Figure 2.8 shows the inner structure of a TGC. When operated with a highly quenching gas mixture (CO_2:n-C_5H_{12}=55%:45%), this chambers work in a saturated mode, thus allowing for small sensitivity to mechanical deformations, which is very important for such a large detector as ATLAS [6].

The saturated mode also has two more advantages:

- the signal produced by a minimum ionizing particle has only a small dependence on the incident angle up to angles of 40 degrees;

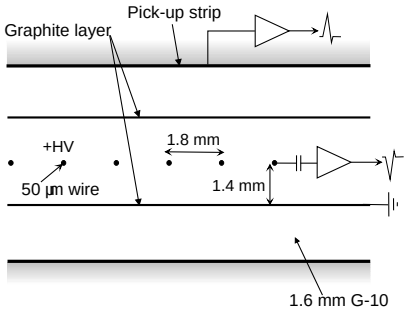

Figure 2.8: Structure of a TGC.

- the tails of the pulse-height distribution contain only a small fraction of the pulse-heights (less than 2%). In particular the response to slow neutrons is similar to that of minimum ionizing particles. No streamers are observed in any operating conditions.

TGCs provide two functions in the endcap: muon trigger and azimuthal coordinate measurement. The middle tracking station of MDTs is equipped with seven layers (one triplet and two doublets) of TGCs, providing both functionalities. The inner tracking layer of precision chambers is equipped with two layers of TGCs, providing only the second coordinate measurement. The second coordinate in the outer precision station is obtained by extrapolation from the middle station. The radial (bending) direction is measured by reading which wire-group is hit; the azimuthal coordinate is obtained from the radial strips.

Since the TGCs are located outside the endcap magnetic field and they can use only a small lever arm ($\sim 1m$), they need a fine granularity also in the bending direction. To obtain the required momentum resolution it has been chosen to vary the number of wires in a wire-group as a function of η, from 4 to 20 wires, i.e. from 7.2 to $36mm$. The alignment of the wire groups in two consecutive layers is staggered by half the group width.

The 3698 chambers (corresponding to a total wire area of $6200m^2$) are mounted in two concentric rings on each endcap: an external one called *outer* or *endcap* ($1.05 < \eta < 1.6$) and an internal one, called *inner* or *forward* ($1.6 < \eta < 2.4$). The forward ring is divided in two logically independent rings at $\eta = 2$. In order to cope with the higher background rate expected in the innermost rings, three different trigger thresholds can be set for the three rapidity regions.

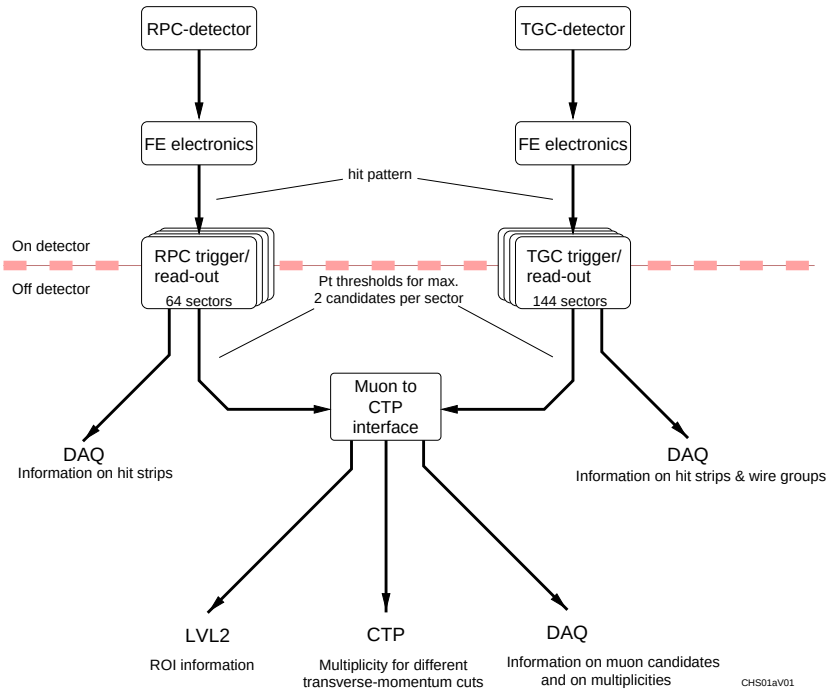

Figure 2.9: Block diagram of the level-1 muon trigger system.

2.3 The level-1 muon trigger

The information provided by the trigger chambers (RPCs and TGCs) is used by a dedicated Muon Trigger System to decide whether muons above a given threshold were produced in a certain event. The sharpness of the p_T cut applied by the trigger is mainly given by the information read out from the detectors in the bending projection. However, the information in the non-bending view helps to reduce the background trigger rate from noise hits in the chambers produced by low-energy photons, neutrons and charged particles, as well as localizing the track candidates in space as required for the LVL2 trigger. In addition, the trigger chamber information in the non-bending view provides the second coordinate measurement for offline reconstruction of muons (the precision chambers give information only in the bending projection).

The basic principle of the algorithm is to require a coincidence of hits in the different chamber layers within a road. The width of the road is related to the p_T threshold to be applied. Space coincidences are required in both views, with a time gate close to the bunch-crossing period ($25ns$). Figure 2.9 shows the block

diagram of the level-1 muon trigger system.

The level-1 muon trigger has to provide to the Central Trigger Processor the multiplicity of muon candidates for each of the six p_T thresholds. This is important so that, for example, a low-p_T di-muon trigger can be maintained at high luminosity. It is foreseen that the threshold on the di-muon trigger will be kept at about $6GeV$ per muon for $L = 10^{34}cm^{-2}s^{-1}$, while the threshold for the single-muon trigger will have to be about $20GeV$ for an acceptable trigger rate. Given the steeply falling muon p_T distribution, it is important that muons should only very rarely be double counted (e.g. in areas of overlapping chambers), giving fake di-muon triggers from single-muon events. It is therefore required by design that at most 10% of the di-muon triggers shall be due to doubly-counted single muons. A detailed description of the working principles and performance of the ATLAS di-muon trigger will be presented in chapter 7.

Chapter 3

The Resistive Plate Chambers

The first publication on Resistive Plate Chambers was in 1981 [8]. In the following years they had great development and now they are widely used in both high-energy and astro-particle physics.

3.1 Detector description

RPC operation is based on the detection of the gas ionization produced by charged particles when traversing the active area of the detector, under a strong uniform electric field applied using resistive electrodes. The electrodes are made of a mixture of phenolic resins (usually called bakelite), which has a volume resistivity ρ_v between 10^9 and $10^{12}\Omega cm$. Glass can be used as plate material as well, and the plates are kept spaced by insulating spacers. The thickness of the plates and the distance at which they are kept are different for different experiments. Here and in the following we refer to the characteristics of RPCs for the ATLAS experiment.

RPCs used in the ATLAS experiment have $2mm$ thick plates, kept at $2mm$ one from each other. The spacers are cylindrical with 12mm diameter and are placed one every $\sim 10cm$ in both directions. The external plate surfaces are coated by thin layers of graphite painting. The graphite has a surface resistivity of $\sim 100k\Omega\square$, thus allowing uniform distribution of the high voltage along the plates without creating any Faraday cage that would prevent signal induction outside the plates (as would happen using, for example, metallic electrodes). Between the two graphite coatings is applied a high voltage of about $10kV$, resulting in a very strong electric field ($\sim 5MV/m$) which provides avalanche multiplication of the primary electrons

generated by ionization by the incident particle. The presence of such a high electric field calls for extreme smoothness of the inner surfaces of the bakelite plates which is obtained covering the surfaces with a thin layer of linseed oil. The discharge electrons drift in the gas and the signal induced on pick-up copper strips is read-out via capacitive coupling, and processed by the front-end electronics.

3.2 Avalanche growth and signal detection

In RPCs the electrons generated by primary ionization are subjected to the strong electric field which make them drift towards the anode. Along their path they collide with other electrons in the medium. Between two consecutive collisions, an electron may increase its kinetic energy enough to generate a secondary ionization, thus starting an exponential multiplication. The mean free path of electrons in the medium is $\lambda = 1/\alpha$, where α is called the *first Townsend coefficient*. Defining n the number of electrons drifting in the gas at a given time, the increment dn obtained during the drift for a distance dx is

$$dn = n\frac{dx}{\lambda} = n\alpha dx.$$

Integrating over a path x, the total number of electrons is

$$N = n_0\, e^{\alpha x} = n_0\, e^{\alpha v_d\, t}$$

where v_d is the drift velocity of electrons in the gas, depending on the gas mixture and on the electric field. Assuming the electric field uniform during the avalanche growth, implies a constant first Townsend coefficient. This is not true when the spatial charge density of the avalanche is large enough to cause distortions on the field generated by the plates. In this conditions α has a dependence on x and the exponential has to be substituted by an integral over x in the previous expressions.

When the avalanche reaches an electron multiplicity of $\sim 10^6$ electrons, its growth slows down due to space charge effects, entering the so called *saturated regime* [23]. For extremely high values of the electronic charge (established by Meek in $\sim 10^8$ electrons for noble gases) the avalanche becomes the precursor of a new process called *streamer*. This is a plasma filament between the electrodes which produces an extremely high current in the gas ($\sim$ 100 times larger than the typical avalanche). The streamer does not evolve in a spark because of

the electrodes resistivity, and it is prevented to propagate transversely an opportune photon quencher in the gas mixture. Streamer signals are therefore greater and easier to detect, but also longer in time and with a higher charge per count. In particular this last characteristic limits the rate capability of the detector operated in streamer mode to a few hundred of $Hzcm^{-2}$. Adopting gas mixtures based on electronegative components allows to retard the appearance of the streamer in terms of the applied electric field [11][12][13]. Finally, the introduction of SF_6 as a quencher removed completely the problem of the streamer, allowing to work in a pure avalanche mode [9].

The main advantage for utilizing resistive electrodes is that, due to their high resistivity, the drop in the applied tension during the discharge is spatially localized. The detector's dead time is due to the time needed to re-charge the gas gap, but it concerns only a small area of the detector surface.

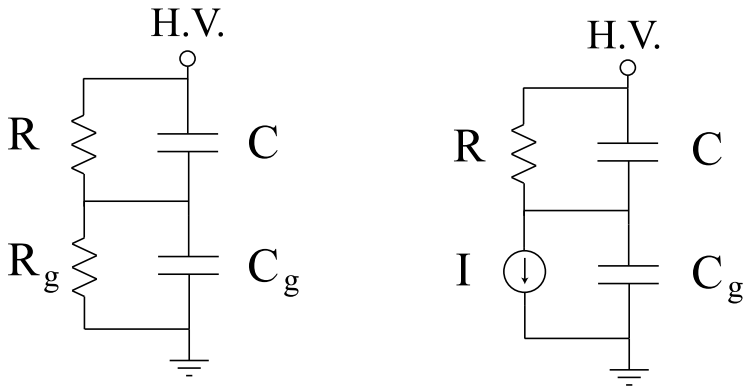

Figure 3.1: Circuital model of an RPC.

An easy circuital model (see figure 3.1), schematizing the RPC structure as two dielectric planar capacitors and taking into account the finite resistivity of the plates, can give an idea of the times involved in the signal formation process. Before the particle crossing, the gas resistance R_g is infinite and the voltage supplied to the graphite coating is also applied to the gas gap. When a charged particle crosses the gap, the avalanche discharge in the gas can be schematized by a current generator which discharges the gas capacitor C_g. The discharge duration typically does not exceed $10ns$. During this time the resistive electrodes work like insulators, and once the charge generated in the gas is balanced, the voltage

applied to the gas gap is null. Then the system goes back to the initial condition discharging the electrodes capacitor:

$$\frac{dq_C}{q_C} = -\frac{dt}{R(C + C_g)}$$

with a characteristic time τ which can be expressed as

$$\tau = \rho\frac{2S}{d}\left(\frac{\varepsilon S}{2d} + \frac{\varepsilon_0 S}{g}\right) = \rho\varepsilon_0\left(\varepsilon_r + \frac{2d}{g}\right)$$

being d the plate thickness, g the gap thickness,and ρ and ε_r the resistivity and the dielectric constant of the bakelite respectively. A typical value for τ is $\sim 10ms$, which is orders of magnitude greater than the signal duration ($\sim 10ns$), and represents the dead time of the detector. It is to be noted that this dead time is indeed limited *just to a small area of the detector*.

The pick-up strips behave as signal transmission lines of well defined impedance and allow to transmit the signals at large distance with minimal loss of amplitude and time infinformationtrips are usually terminated at one end with by front-end electronics and on the other one by proper resistor to avoid reflections. The induced charge is split in two parts, thus reducing the readable signal by one half. The read-out electrode can be described as a current generator charging a parallel RC circuit. The resistor R connecting the line to the ground is half the line impedance. The electrode capacity C is proportional to the pick-up area determined by the spatial distribution spread of the induced charge. The time constant $\tau = RC$ for typical values of these parameters is of the order of tenths of ps, much shorter than the rise time of the signal: the current injected in the strip is at any time proportional to the current of the discharge in the gap.

Assuming the ionization electrons uniformly distributed along the gap depth, n is defined to be the number of ionization electrons per unit length. At a time t all the primary clusters produced at a distance $x > vt$, being v the drift velocity, were absorbed, while all the others had a gain $\sim e^{\alpha vt}$. In RPCs the ion current is essentially invisible and only electrons give a prompt signal. The total number of electrons in motion in the gap at the time t is

$$N(t) = n(g - vt)e^{\alpha vt}$$

thus inducing a current on the pick-up electrodes given by

$$i(t) = eN(t)\frac{v}{g} = evn\left(1 - \frac{vt}{g}\right)e^{\alpha vt}$$

The *prompt* charge q is given by the current integral up to the maximum drift time $t_{max} = g/v$ [14]

$$q = \int_0^{g/v} i(t)\,dt \approx \frac{eng}{(\alpha g)^2}e^{\alpha g}$$

to be compared with the total charge Q flown in the gap

$$Q = \int_0^{g} ene^{\alpha x}dx \approx \frac{eng}{\alpha g}e^{\alpha g}$$

The distance between the gas gap and the read-out electrodes is increased by the thickness d of the resistive plates. A simple calculation in which the plates and the gas gap are treated as three serially connected capacitors leads to one more correction factor on q, giving a total ratio of

$$\frac{q_{prompt}}{Q} = \frac{1}{\alpha g}\left[1 + \frac{2d}{\varepsilon_r g}\right]\frac{1}{2}$$

which takes into account also the splitting of the induced signal between the front-end and the terminating resistor.

3.3 The gas mixture

The gas mixture is crucial in the RPC operation and it must be carefully chosen in order to obtain the required performances. The first consideration to do when choosing a gas mixture for RPCs is whether the detector will work in avalanche or streamer mode.

The filling gas is usually composed by an optimized mixture. To operate the chamber in streamer mode, the gas should provide a robust first ionization and a large avalanche multiplication even at low applied field. One typical choice is Argon, which, providing great avalanche increase with abundance of electrons, sets the ideal condition for the streamer production. If the desired operating regime is avalanche mode, the main component should be an electro-negative gas with high enough primary ionization, but with a low mean free path for electron capture, in order to maintain the number of electrons in an avalanche below the Meek limit.

A gas showing this characteristics is, for example, $C_2H_2F_4$.

The gas mixtures used for RPC operation often contain one more component, with the role of absorbing the photons produced by electron-ion recombinations, thus avoiding photoionization (with related multiplication) and limiting the lateral charge spread. Typically an hydrocarbon shows the characteristics described above.

Significant changes in environmental variables, such as temperature and pressure, alter the characteristics and properties of the filling gas (for example the density ρ), and influence the ionization and multiplication processes. This is the reason why performances at the same applied field but with different environmental conditions are in general different. In order to make meaningful comparison between data sets taken at some distance in time one from another, the applied voltage value are *normalized* according to the formula

$$HV_{eff} = HV_{app}^{T^1,P^1} \frac{T^1}{T^0} \frac{P^0}{P^1}$$

justified with the hypothesis that the gas discharge related phenomena are invariant for any change in P,V,T which leaves the ratio of the voltage over the gas density unchanged.

3.4 RPC working regimes and performances

RPCs are operated in *avalanche* or *streamer mode* [10], corresponding to the two different discharge mechanisms described in 3.2. Typical signal amplitude for an avalanche is $\sim 1mV$, with a duration of about $4ns$ and an average charge of $\sim 1pC$. The amplitude of signals induced by streamers is typically $\sim 100mV$, while their duration is of the order of 10 to $20ns$, producing a $\sim 100pC$ charge.

Avalanche signals need a strong amplification and have high frequency components due to their very short duration, and are therefore particularly difficult to detect. Streamer signals on the contrary do not need any complex signal processing.

When a streamer occurs, both the charge and the detector surface involved in the discharge are larger compared to the ones associated to an avalanche. As discussed in 3.2, this implies a lower rate capability of the detector. Typical rate capabilities for RPCs working in streamer mode are of the order of $100Hz/cm^2$. This value can be increased reducing the charge released in the gas, i.e. working in avalanche mode, or decreasing the plate resistivity.

By carefully choosing the gas mixture it is possible to obtain a stable avalanche working mode, with a large operating voltage plateau not contaminated by streamers. A sophisticated read-out electronic allows to detect the small and fast signals generated by avalanches, thus reaching rates capabilities up to $1 kHz/cm^2$.

Avalanche operation is also safer for what concerns the detector ageing effects, which depend on the total integrated charge.

RPCs spatial resolution depends both on the read-out geometry an electronics. Using an analog readout it is possible to obtain resolution of $\sim 1cm$, but with a digital read-out the resolution is limited by the strip width, typically of the order of a few centimeters.

Concerning time resolution, it is natural to compare RPCs with wire detectors. The drift times in the radial electric field are different for different clusters, depending on their distance from the wire. The signal duration can be as long as hundreds of ns and is fixed by the cluster at maximum distance from the wire. On the contrary, the high and uniform electric field applied to the gas gap by the electrodes is the same for all primary clusters, producing at fixed time the same growth, limited by the distance of the primary clusters from the anode. The signal at any time is the sum of simultaneous contributions from all primary clusters multiplications. The resulting time jitter for detectable signals is always $< 2ns$.

Chapter 4

Ageing test of ATLAS RPCs at X5-GIF

The accelerator background at LHC will be dominated by soft neutrons and gammas that are generated by beam protons at very small angle [15]. Such a heavy background calls for severe requirements on the trigger detector in terms of rate capability and time resolution, crucial for bunch crossing identification. Moreover, almost for all the chambers installed in the ATLAS cavern, it will be impossible to perform any hardware reparation or substitution once the detector is installed. It is therefore crucial that the chambers do not show any abnormal ageing effect which could degrade their performace during the ~10 years of the ATLAS operation.

For this reason an ageing test of three production ATLAS BML RPCs has been performed at CERN. The chambers have been irradiated with photons from a ^{137}Cs source in order to test their rate capability and to integrate a total charge per cm^2 corresponding to $\sim$ 10 ATLAS years including the safety factor of 5, which is applied in the requirements placed on all the ATLAS detectors to take into account the uncertainties in the background rate.

In the following, we will refer to *ATLAS years* as a measurement of the ageing of the detector. One ATLAS year corresponds to a charge of $30mC/cm^2$, which is obtained assuming 10^9 counts per year per cm^2 and an average charge per count of $30pC$. This calculation includes the abovementioned safety factor of 5.

4.1 The X5 beam

The X5 beam is part of the West Area test beam complex at CERN. It can work as a secondary or tertiary particle beam, providing hadrons, electrons or muons of energy between 10 and 250 GeV.

A 450GeV/c primary proton beam, with typical intensities of 2×10^{12} protons per bunch, is extracted from the SPS and directed on the primary target, from which a secondary beam is extracted.

The secondary beam is called H3 and normally consists mainly of pions and electrons, whose energy and polarity may change according to the requirements of the West Area users, ranging normally around 120GeV/c up to a maximum of 250GeV/c.

The H3 beam is split into two branches, each transporting about 10^7 particles per SPS cycle to the X5 and X7 secondary targets. The average decay length

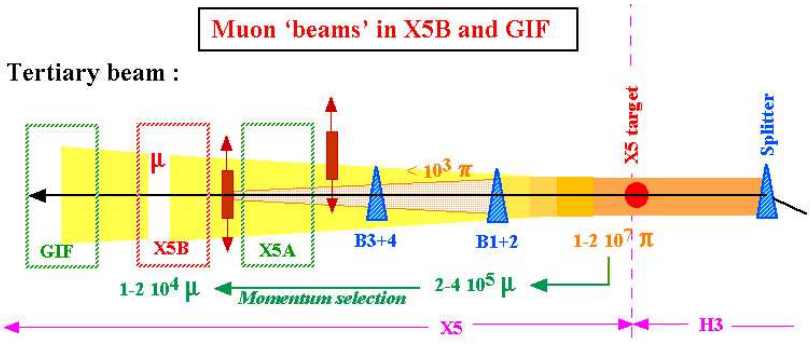

Figure 4.1: X5 Beam from SPS.

of charged pions is $\sim 55m/GeV$. For example at 120 GeV/c the average decay length is about 6600m. Over a length of 100m between the splitter and the first X5 bending, some 1.5% of the pions decay as $\pi \longrightarrow \mu + \nu$. According to the average pion intensity more than $10^5 \mu^{\pm}$ are produced. The pion decay kinematics implies that $0.57 \leq p_\mu/p_\pi \leq 1.0$. The X5 beam will transport these muons if its settings are tuned to momenta in the appropriate range. Muons will always have $80 \pm 20\%$ of the H3 momentum.

A common situation for tracking tests is a high momentum tertiary beam with p_{X5} well above 57% of the H3 momentum (figure 4.1).

In this case typically some 10^4 muons per burst are contained within an area of 10×10 cm^2. The remaining muons are widely spread over several square metres.

4.2 The Gamma Irradiation Facility

The Gamma Irradiation Facility, GIF, located downstream of the final dump of the X5 beam, is equipped with a ^{137}Cs source of 20 *Ci*, emitting in 85% of the decays a single photon of energy $E_\gamma = 0.66 MeV$.

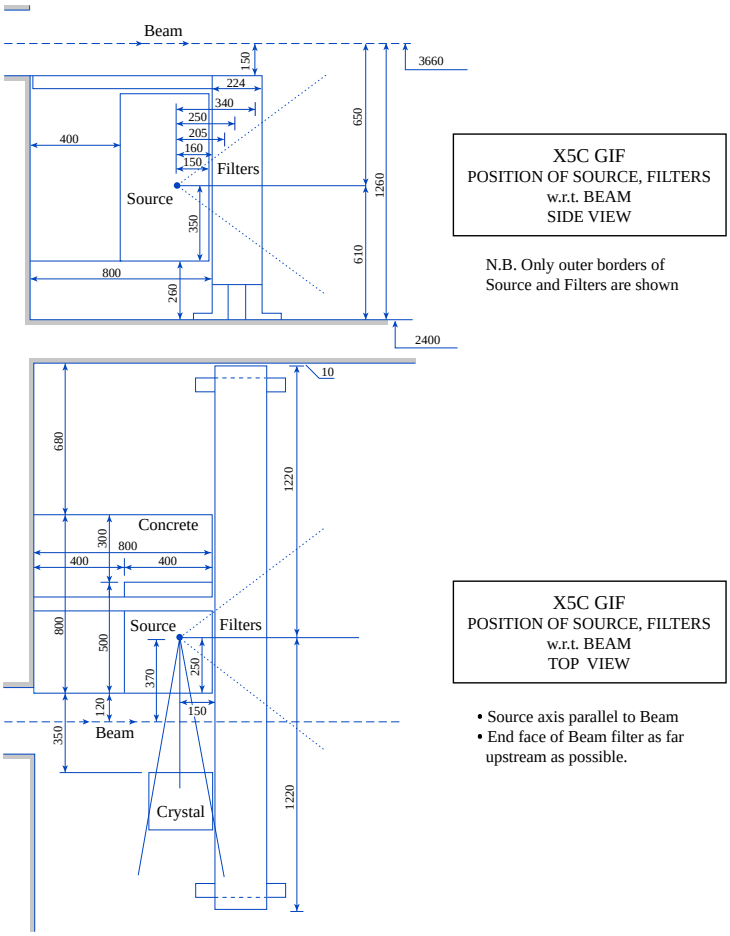

Figure 4.2: The GIF at X5 test beam.

A properly shaped lead filter (see figure 4.3), 4*mm* thick, is put in front of the source opening, in order to make the photon flux uniform over any surface perpendicular to the beam axis. Several overlapping filters, moved by a remote control system, set a variable overall absorption factor (ABS) which allows to modulate the photon flux intensity I, from the maximum value (I=1) to zero (I=0). A detailed description of the position and orientation of the beam, source and filters is shown in figures 4.2 and 4.3.

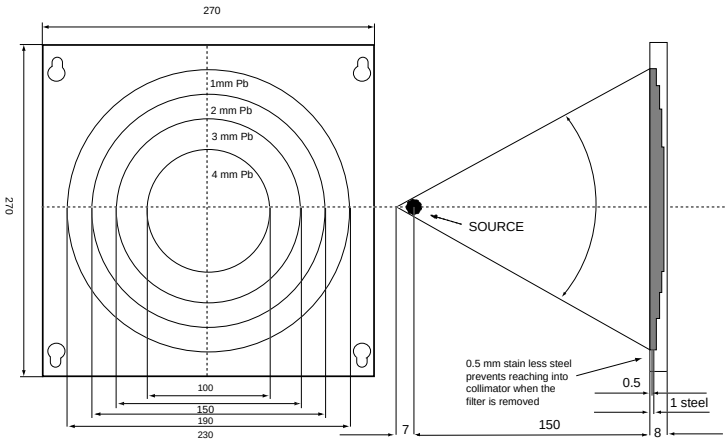

Figure 4.3: Lead plug on front irradiation opening.

The photon sensitivity of the RPC detector is given by the probability of Compton and photoelectric effects on the bakelite electrode surfaces facing the gas volume, convoluted with the energy spectrum of the produced electrons which ionize the gas. The average sensitivity for $E_\gamma = 0.66 MeV$ has been already measured [16] and reaches values close to 0.5×10^{-2}. It is significant to stress that preliminary results of studies [17] about photon flux energy spectrum and spatial uniformity of irradiation at X5 have shown that:

1. The energy spectrum is not monochromatic. The total gamma flux is made of a direct component with $E_\gamma = 660 keV$ and a scattered one. The latter is due to an X fluorescent peak on Lead ($E_\gamma = 85 keV$), to scattering on collimators and filters ($E_\gamma > 180 keV$) and to albedo due to diffusion on the concrete hall's walls. The ratio between direct and scattered components with respect to the total flux depends on the absorption factor of applied filters and is a function of the distance from the source. Figure 4.4 shows the results from an accurate simulation [17]. The simulated spectrum with absorption factor 1 (ABS=1), at $155 cm$ from the source is shown in figure 4.5.

2. The spatial distribution of irradiation is not uniform but it presents a peak around the axis orthogonal to the source front opening, because of steel screws on ABS=1 and ABS=50 absorbers.

A more detailed description of this facility and of the characteristics of the γ flux can be found in [18].

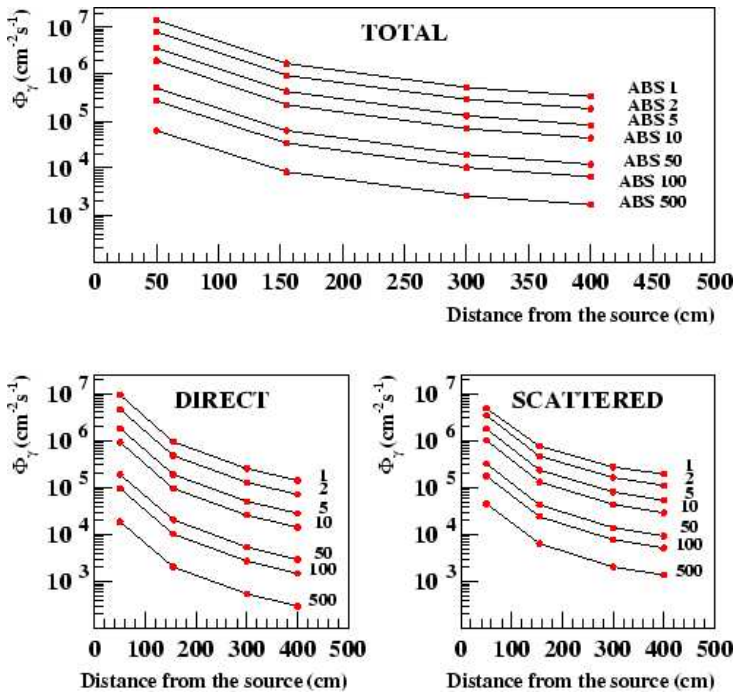

Figure 4.4: Simulated photon flux components as a function of the distance from the source.

4.3 Experimental setup

Three production ATLAS RPC chambers (BML-D) are installed in the GIF area, along the beam line. A schematical view and a picture of the setup are shown in figures 4.6 and 4.7 respectively. The chambers have 2 detector layers which are read out by strips oriented in both the η and φ directions. The chambers are perpendicular to the beam line, with the long side (about 4m) oriented in the vertical direction. For details on the chamber structure, see [2]. The chambers are operated with the ATLAS gas mixture $C_2H_2F_4/i\text{–}C_4H_{10}/SF_6 = 94.7/5/0.3$.

The trigger is provided by the coincidence of three scintillator layers of 33x40 cm^2, each made of three slabs. During the beam runs, the three layers are aligned along the beam line, while for the cosmic rays runs, they are arranged as a telescope with the axis oriented at 40 degrees with respect to the vertical direction, in order to maximize the trigger rate.
Signals from the frontend electronics are sent to a standard ATLAS “splitter board” [7] as in the final architecture foreseen for the trigger and readout electronics, and

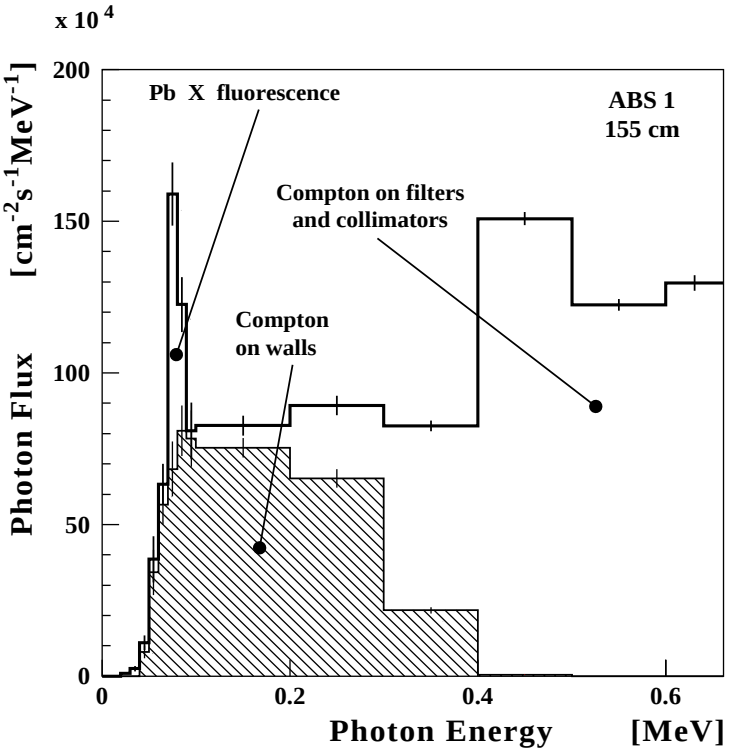

Figure 4.5: Simulated spectrum of the scattered photons at 155 cm from the source on the axis of the irradiation field and for absorption factor (ABS) 1. The three main contributions are indicated: two are from filters and collimators (white area), the other from walls and floor (dashed area). The total flux of scattered photons amounts to $6.4\times10^5 cm^{-2}s^{-1}$, while the flux of direct photons (at $662keV$, not shown) is $8.0\times10^5 cm^{-2}s^{-1}$ [18].

subsequently to TDCs working in common stop mode (see [19]) which record up to 16 hits per event per channel, in a $2\mu s$ gate. Both the leading and falling edges of the signals are recorded. The data acquisition is performed using a LabView^{TM} application.

The DCS system, also implemented using LabView^{TM}, records both the low and and high voltages as well as the gap currents. Gas composition, together with all relevant environmental data such as pressure, temperature and relative humidity are controlled as well. The gas relative humidity, also monitored by the DCS, is set in the range of 30%-50% by bubbling in water a fraction of the total gas flux.

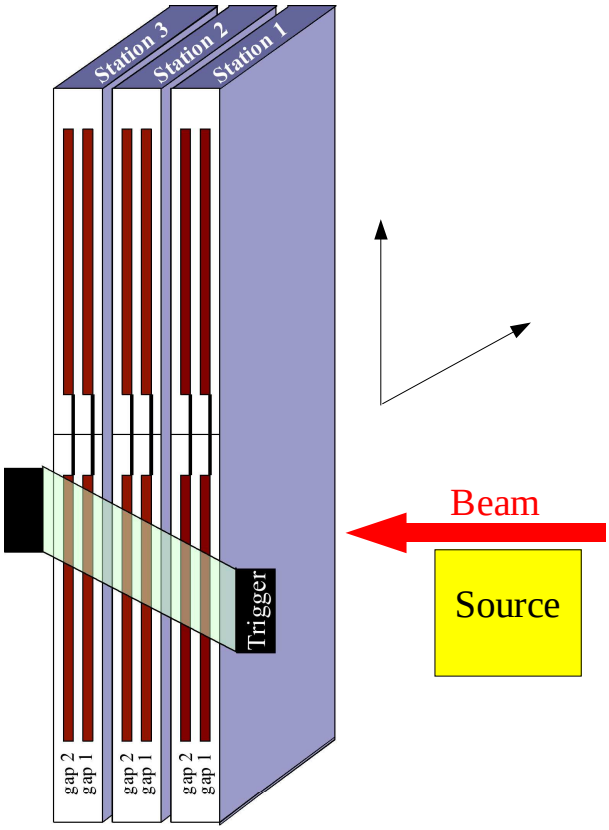

Figure 4.6: Experimental setup at X5/GIF

4.4 Ageing effects in Resistive Plate Chambers

Long time operation of resistive plate chambers is known to produce two main ageing effects, both leading to a decrease in the performace of the detector.

- Changes in the chemical composition of the plates may increase their resistivity, thus reducing the rate capability.

- Moreover, the inner surface of the plates is degraded by continuous operation with fluorine-rich gas mixtures, leading to an increase of the noise in the detector.

Figure 4.7: Experimental setup at X5/GIF. The chambers under test are visible in the background, in their blue support structure. The orange box in the foreground contains the source, while the pink structure supports the lead filters.

Both these ageing effects have been extensively studied during this test, and several techniques have shown their effectiveness in reducing to an acceptable level all the losses in performace related to the detector ageing.

4.4.1 Plate resistivity increase

Systematic tests carried out, in the ATLAS framework, on RPCs of different sizes operated in avalanche mode at high working currents [24], showed a decrease of the rate capability at fixed voltage as the main long term ageing effect. This effect was demonstrated to be due to the increase of the electrodes resistance [21].

Though all RPCs for the LHC experiments are designed with very large safety margins of rate capability, great efforts have been dedicated to the study of the electrode conduction properties due to the very long time of operation foreseen. The electrode resistance increase is found to be due to two main components:

- a long term effect, consisting in a progressive increase of the anodic graphite coating resistivity; the cathodic layer is almost unaffected [22];

- an increase of the laminate resistance which depends both on the total integrated charge and on environmental conditions such as the relative humidity.

In the test described in the following, particular attention has been dedicated to the study of the second of these two effects.

It has long been known ([10]) that the electrical properties of the plastic laminate depend on the environment temperature and relative humidity. Materials such as phenolic-melaminic laminates have a negative temperature coefficient, i.e. their resistivity decreases for increasing temperature. Moreover, when the plates are exposed to dry air circulation, their resistivity gradually increases even by a large factor. This effect is completely reversible once the sample is left at room RH for a sufficient time.

On the other hand, plates kept under high current densities (hundreds of $\mu A/m^2$) for long periods, also show a gradual increase in resistivity which is found to be faster when the plates are operated at lower RH values. This effect of the relative humidity has been shown ([20]) to be *selective*, in the sense that its effect is much more effective if the humidification is performed *on the anode side of each plate*.

These observations suggest that both the gas mixture and the external environment need to be humidified in order to guarantee that the anodes of the two electrode plates are operated in the proper RH conditions. To achieve the necessary control on the external relative humidity, the area surrounding the three chambers under test has been delimited using PET foils. The air relative humidity near the chambers is hence controlled by means of two humidifiers.

4.4.2 Plate surface damage

The quality of the inner surface of the plates is crucial for the operation of RPCs, since any damage of the surfaces translates to a disuniformity of the electric field, thus increasing the noise in the detector.

The gas mixture used in ATLAS RPC will contain a high fraction ($\sim$ 95%) of $C_2H_2F_4$. Long term operation of RPCs with gas mixtures based on fluorine compounds is known to lead to damages to the internal surface of the chambers, due to the reaction of the linseed oil coating layer with fluorine ions produced in the gas during the discharges. A more detailed study of the F^- production in RPCs will be presented in chapter 5.

In order to reduce this ageing effect, particular attention has to be given to carefully tune the gas flow, which has to be high enough to ensure proper removal of F^- ions from the detector. Given the number of gas gaps to be used in the ATLAS detector, the necessary gas flow would be so high that it is not affordable to achieve it without a recirculation system. Such a system will filter the output gas from the chambers and send it again in the gas gaps, together with a small fraction of new gas. During the test described in this chapter, a prototype of such a recirculation system has been used, and its effectiveness tested.

4.5 Measurement techniques

In order to monitor the performaces for the detector, three types of measurements were carried out all along the test:

- quantities such as chamber efficiency, average cluster size and single counting rate where monitored by means of an offline analysis program specifically developed for this test;
- plate resistivity measurements;
- the noise level was measured using the DCS system, in particular measuring the gap currents;

4.5.1 Offline analysis

During the test, the chamber efficiencies were monitored using cosmic rays triggered by the scintillators, while high statistics efficiency measurements were

made when the X5 muon beam was available.

For each event, the muon trajectory is reconstructed.

The scintillator slabs of the trigger system, of size 11x40cm^2, would only allow a very modest tracking, not sufficient to eliminate all accidental hits at very high counting rate induced by the source. The tracking capability is therefore improved using the hits recorded by the RPCs, as described below:

1. hits recorded by the RPC under test are ignored in the tracking;
2. only hits registered in a time window of 25ns around the beam peak are considered useful for the track reconstruction, in order to reduce the probability to use an accidental photon hit in the tracking;.
3. for each electronic channel (i.e. for each strip) a dead time of 50ns is applied by the analysis algorithm, in order to avoid any double counting due, for example, to after pulses;
4. tracks are reconstructed only for events showing a single cluster in at least three layers (out of the five available). This is useful to improve the quality of the reconstructed track eliminating, for example, di-muon events.
5. a track in both the η and φ directions is required.
6. the layer is considered efficient if it shows a cluster aligned to the track within ± 1 strip.

The steps described above are repeated for each gas gap. In the evaluation of the efficiency of each layer, dead strips are not taken into account, i.e. a track crossing a strip known to be dead will not be considered as an inefficiency of the layer. In addition to the efficiency, average cluster sizes are measured for each layer.

Particular importance, in conjunction with the efficiency measurements, has been given to single counting rate measurements. They are performed on the same data sets used for efficiency measurement, taking into account only hits which are found to be not in time with the beam. Figure 4.8 shows, as an example, the time spectrum for the φ layer of Station1, gap 1. The plot refers to a run taken at full source exposure: the time window used for rate measurements is shown.

Data sets were taken with different front end electronic thresholds, source intensities, and operating voltages. The plateaus shown in figure 4.9, for example,

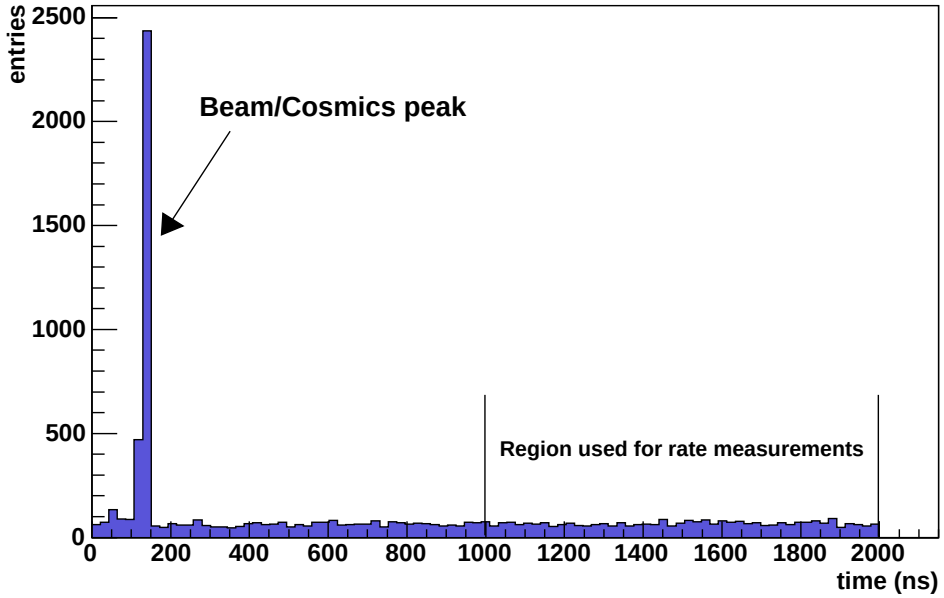

Figure 4.8: Time spectrum for Station 1, gap 1, φ layer under full source exposure. Hits in the time window $1000 \div 2000 ns$ are used for single counting rate measurement

refer to the gap number 1, which is the nearest to the source (at about $2.5m$), after an integrated charge corresponding to 5 ATLAS years (including a safety factor of 5). Figure 4.10 shows, for the same gap, the counting rate as a function of the HV for different irradiation intensities.

4.5.2 Plate resistivity measurements

Two different methods were followed for the resistivity measurements:

HV drop correction. This method is based on the comparison of the efficiency plateaus with and without source irradiation. The current driven under irradiation is much higher than the one just due to the muon beam or cosmic rays. This current produces a significant voltage drop across the plates and the voltage applied to the gas can be written (see [23]) as

$$V_{gas} = V - R_{pl} I_{gap} \tag{4.1}$$

where V_{gas} is the effective voltage on the gas gap, V is the power supply voltage and I is the current driven by the gap.

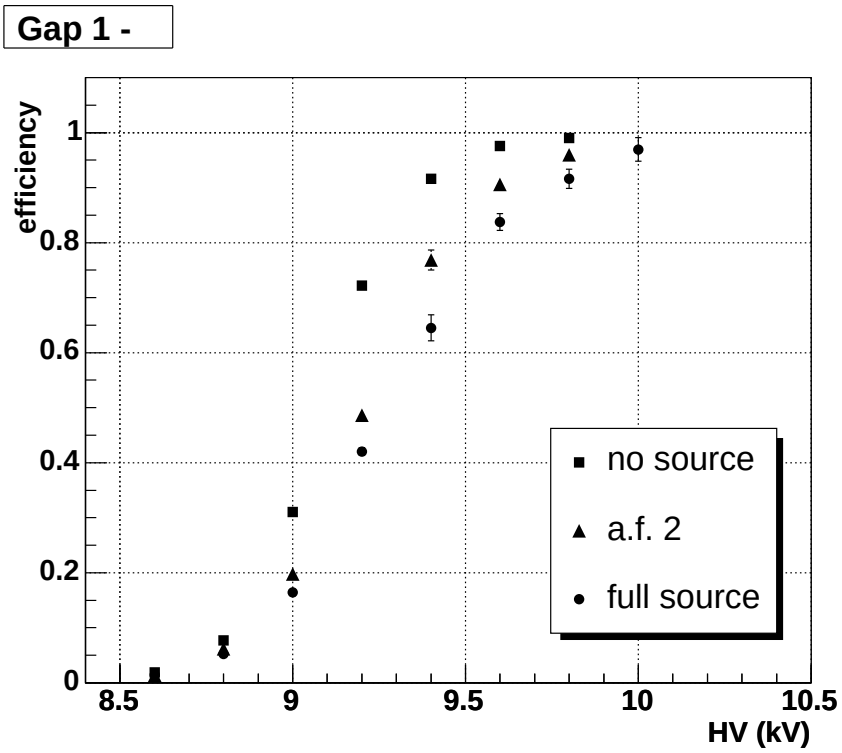

Figure 4.9: Efficiency versus high voltage at different source intensities, as measured with the muon X5 beam.The plot refers to Station 1, gap 1, φ, after 5 ATLAS years of ageing.

This drop causes the efficiency plateaus under irradiation to be shifted at higher HV values, as shown in figure 4.9. This shift allows to evaluate the plate resistivity when the gap current is also measured. Figure 4.11 shows an example of the application of this technique.

I-V characteristic in pure Argon. The standard ATLAS gas mixture is replaced by pure Ar. As shown in figure 4.12, the I-V curve is characterized in this case by a transition region around V=2kV with a fast current increase. For higher voltages a linear current increase is observed. We assume that above the transition voltage, the drop across the Argon remains constant, so that the slope $\Delta V/\Delta I$ in the linear region gives the plates total resistance.

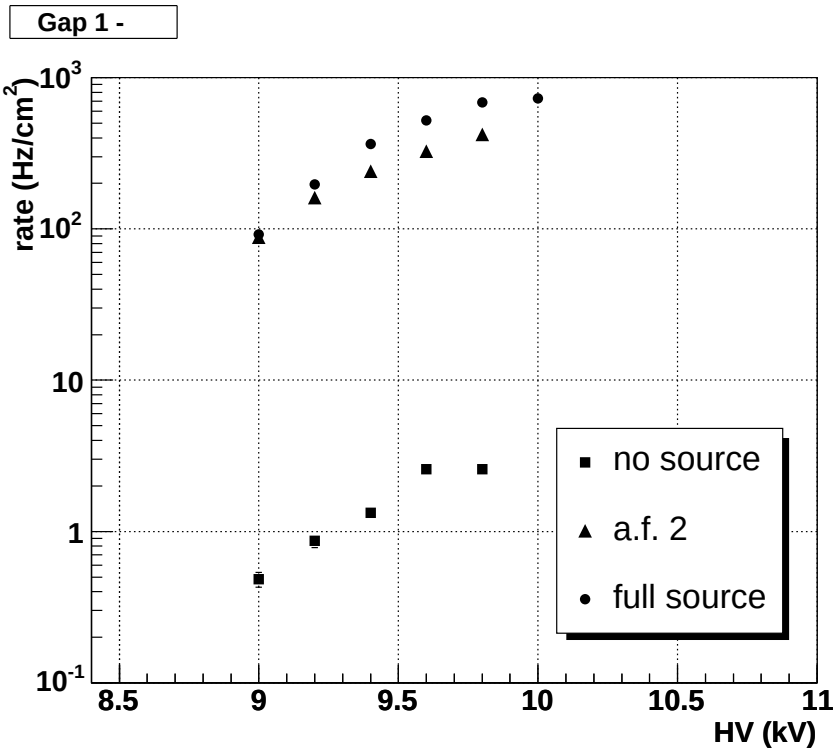

Figure 4.10: Single rate measurement at different source intensities for Station 1, gap 1, η, after 5 ATLAS years of ageing.

4.5.3 Noise level monitoring

It is possible to evaluate the status of the inner surface of the plates using the single counting rate measurements described above. However, being the time between two consecutive data taking periods of the order of two months, it is necessary to use a monitoring tool providing more frequent noise level estimations.

One of the quantities continuously monitored by the DCS system for each gap is the *gap current*, defined as the total current driven by the gas, as read on a $100k\Omega$ resistance put on the ground connection of the gap (see figure 4.13). It is a precise estimator of the number of avalanches in the gap and therefore, when measured without source irradiation and without beam activity, of the noise level.

Gap current measurements as a function of the operating voltage where taken almost daily all along the test.

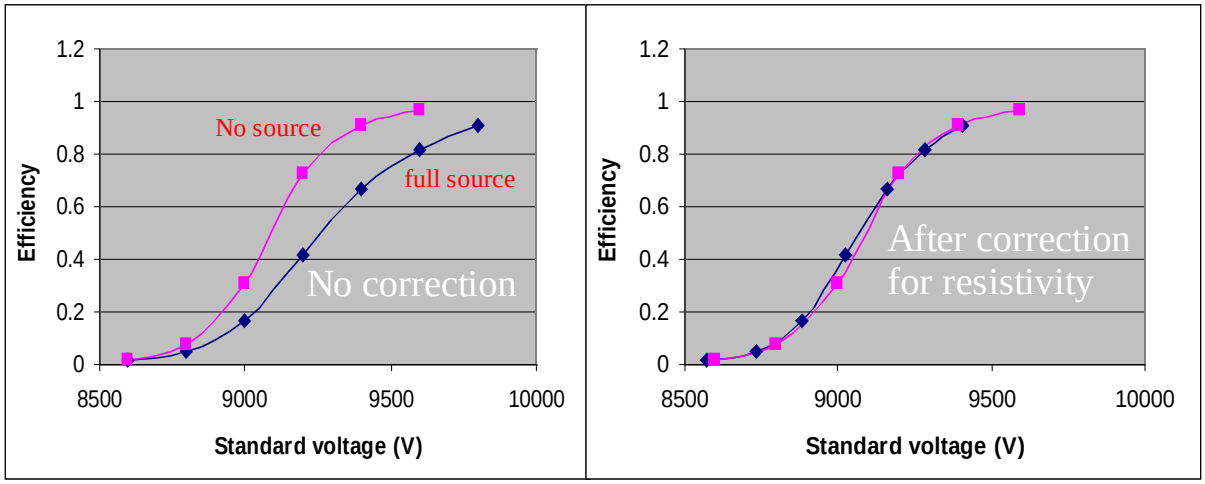

Figure 4.11: Procedure for plate resistivity measurement using efficiency plateaus.

4.6 Experimental results

4.6.1 Plate resistivity evolution

Figure 4.14 shows the evolution of the plate resistivity as a function of time for the six gaps under test. The figure also shows the relative humidity of the gas mixture. Starting from October 2003 the environment surrounding the chambers was put under a constant 50% RH value. The resulting decrease in resistivity is clearly visible in the plot. This effect was shown to be reversible: a short period without humidification of the external air has indeed produced an increase in the plate resistivity, while once the external RH control was restored the resistivities of the gaps showed again a significant decrease.

It has to be noted that the resistivity values corresponding to the two measurement techniques are systematically different. This result is exactly what can be expected considering that the Argon technique measures the *average* resistivity of the plates, using the whole surface of the electrodes for the measurement. On the other hand, the plateaus technique only measures the resistivity on a fraction of the detector surface, i.e. the one covered by the scintillator trigger. The gas input to the chambers is on their bottom side, and the external air humidification is provided by two humidifiers placed on the ground. This implies that the humidification is not constant along the plate surface; in particular, the lower parts of the gaps are better humidified, i.e. they have lower resistivity.

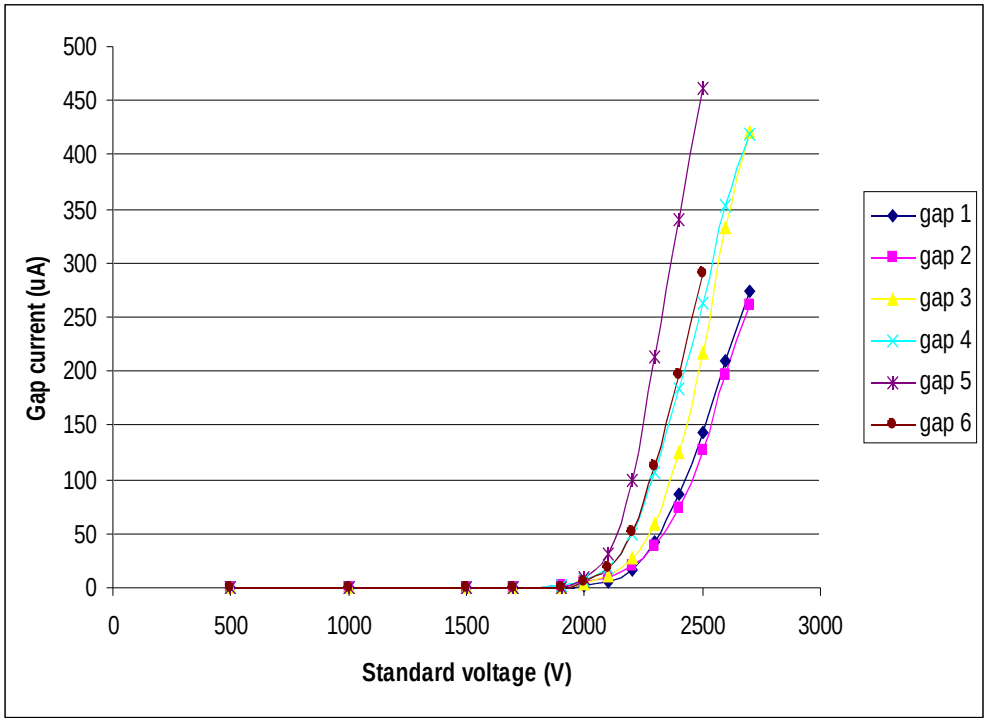

Figure 4.12: I-V characteristics in pure Argon.

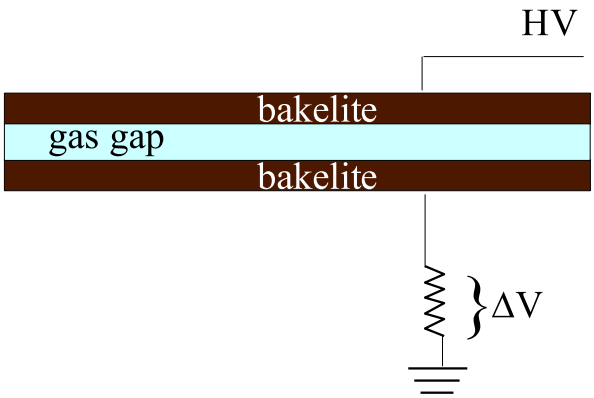

Figure 4.13: Gap current measurement.

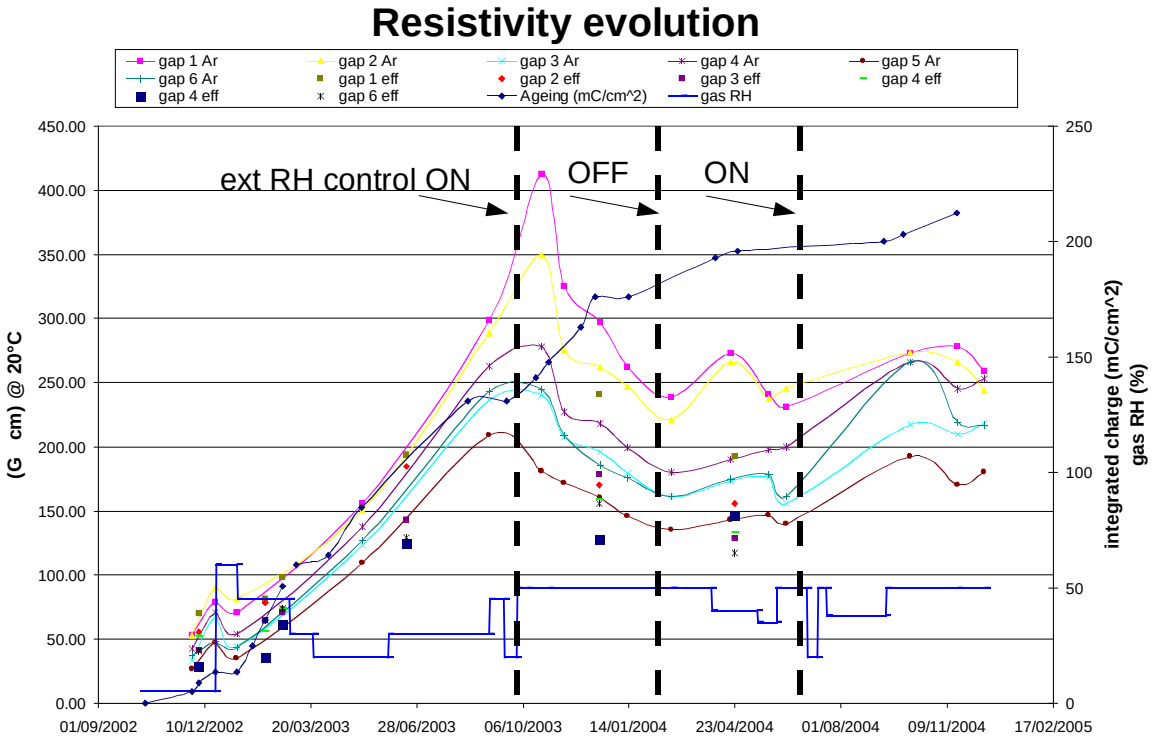

Figure 4.14: Plate resistivity evolution.

4.6.2 Detector performance

Chamber efficiencies at closed source, measured periodically both with cosmics rays and with the X5 beam, did not show any loss along the test.

Figure 4.9 shows the efficiency vs HV plot for Station 1 gap 1 φ at different source intensities. The high current driven by the gaps under source irradiation causes a voltage drop across the plates. Due to this drop, the plateaus show a shift towards higher voltages an a slower raise, compared with the plateaus taken without irradiation. This effect is enhanced in winter by low temperatures (10÷15 °C) which increase the plate resistivity.

The average cluster size also remained stable during all the test.

The rate capability of the chambers was also shown to be largely above the ATLAS requirements. Figure 4.15, for example, shows the rate versus efficiency plot for Station 2 gap 1, φ layer, taken with maximum photon flux. The plot was obtained from data at different HV values after an ageing of ~7 ATLAS years (including a safety factor of 5), and it clearly shows that at rates around $600 Hz/cm^2$ the chambers are still fully efficient. For comparison, the rate expected in ATLAS will be of the order of $20 Hz/cm^2$. For each point, the corresponding HV value is

shown as well.

After about 7 ATLAS years of ageing (including a safety factor of 5), following a serious damage to the chambers caused by a problem in the recirculation system, the gas mixture was changed to $C_2H_2F_4/i\text{–}C_4H_{10}/SF_6 = 84.7/15/0.3$, which is a flammable mixture, and all the chambers were reverted to open flow mode. Section 4.6.4 will describe in more detail the reasons and effects of such a change from the point of view of damage recovery. Concerning the detector performaces, the chambers operating with the new mixture were tested on the X5 beam, thus obtaining useful information on the behavior of the ATLAS RPCs with gas mixtures different from the standard one.

Figure 4.16 shows the comparison between two efficiency plateaus taken without source irradiation with the two different gas mixtures. Station 1, gap 2, φ layer is shown as example. The increase in i–C_4H_{10} concentration caused the working point to be shifted to lower HV values: this shift has been measured and was found to be of $80 \div 100$ V for all the gaps. The same shift was found in the other performance parameters, such as average cluster size and single counting rate. This shift is a well known effect of the change in the gas mixture and is due to the combination of two factors:

- the concentration of a quenching gas such as i–C_4H_{10} is increased: this tends to move the working point towards higher HV values;

- the increase in i–C_4H_{10} is indeed compensated by a decrease in $C_2H_2F_4$ which, being a highly electronegative gas, tends to inhibit the avalanche formation. The result of this decrease is therefore a shift of the working point towards lower HV values.

4.6.3 Gas recirculation

At the beginning of July 2003 the gas closed loop was introduced on 4 out of the 6 tested gas gaps, in order to simulate the real working conditions in ATLAS. The two remaining gaps were left in open flow for comparison. The output gas of the chambers goes through a system of filters and then is sent again in the gaps, together with a fraction of fresh gas. The total gas flow is set at 40 l/h, and the fraction of recirculated gas has been gradually increased as reported in table 4.6.3. The gas at the input and at the output of the chambers was sampled and analyzed in order to find any polluting component related to the chamber operation. The

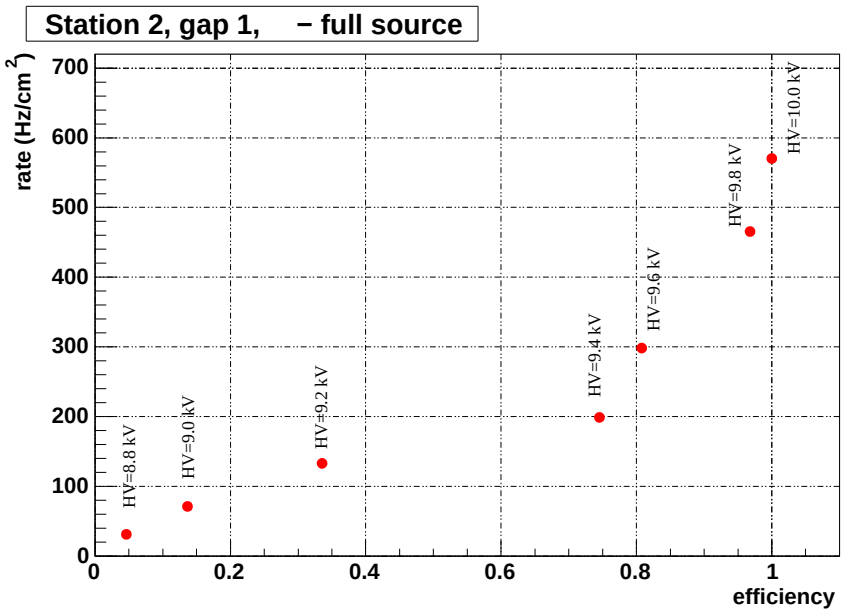

Figure 4.15: Efficiency vs rate plot. The gaps under test showed, after 7 ATLAS years (including a safety factor of 5), a very good detection efficiency even at rates ∼ 30 times larger than the nominal ATLAS rate.

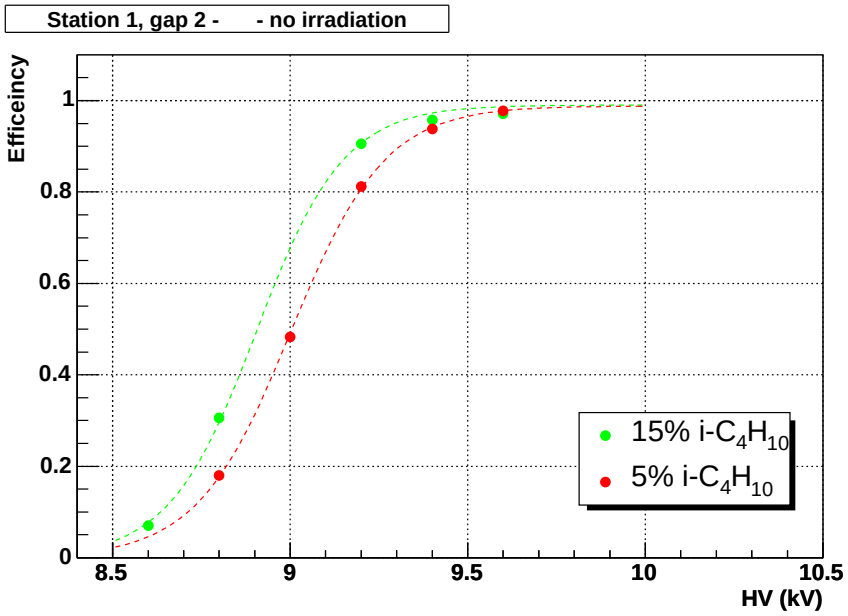

Figure 4.16: Efficiency plateaus with the two different gas mixtures, taken with the X5 muon beam. The plot refers to data taken without irradiation.

analysis of the recirculated gas didn't show any excess of pollutant with respect to open flow operation.

time	fraction of recirculated gas
first 3 months	50%
following 3 days	80%
following 5 days	90%
up to June 2004	95%

Table 4.1: Fraction of recirculated gas with respect to total flux

4.6.4 Noise control and damage recovery

During the test, the frequent measurements of the noise level pointed out two main causes for the increase of the noise in the detector:

- temperature increases have shown to be responsible for increases in the gap currents (at working point);
- any malfunctioning of the gas system, such as insufficient total flow or lack of maintenance of the recirculation system's filters, had a serious impact on the gas gaps, causing rapid increase of the gap currents.

Figure 4.17 shows the variation of the working currents of the six gaps along the test. Current measurements are taken without irradiation. It is clear the correlation between temperature and current variations, in particular for Station1, gap2 (gap 2 in the plot). The current increase, which is amplified in summer, is however completely reversible, as shown in the plot.

Working currents have also proven to be an effective tool to detect any malfunctioning of the gas system. In particular two points are marked in figure 4.17: the first is a current peak in coincidence of a wrong gas mixture, the second one corresponds to the exhaustion of one of the filters of the recirculation system. Both these peaks clearly affected only the gaps operated in closed loop, even if, in correspondence of the second peak, an increase in temperature caused a general increase of the gap currents.

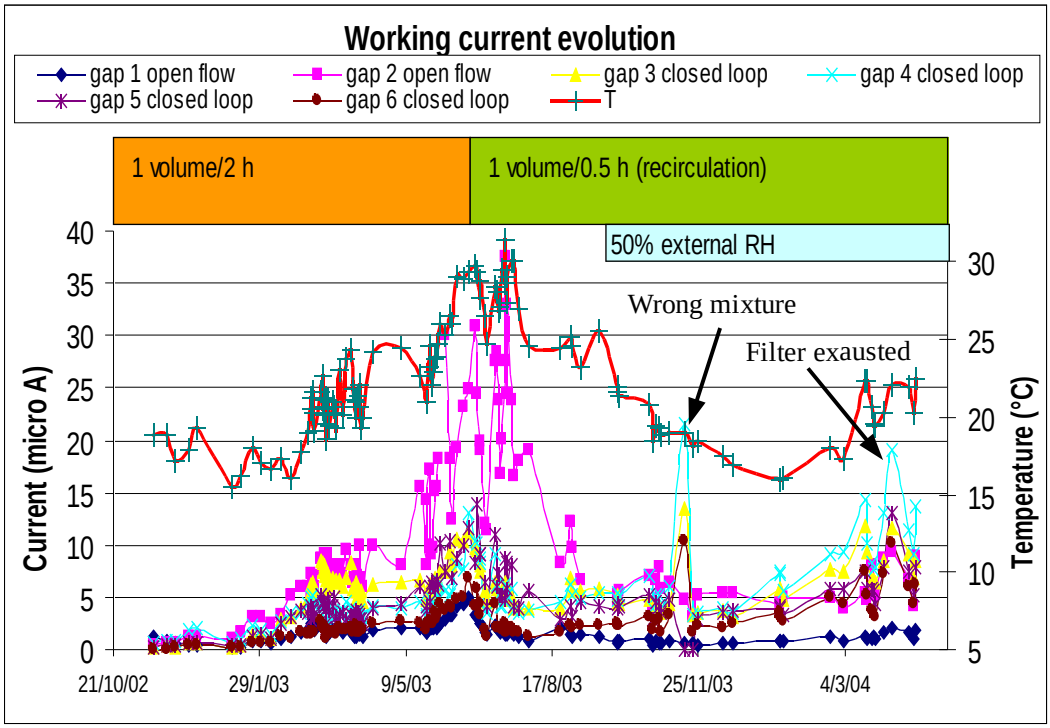

Figure 4.17: Working current evolution. Gap numeration is given here starting from the nearest to the source (gap 1) to the farthest (gap 6). The gas flow (in volumes per hour) is reported, together with the start of the recirculation test. External RH control is indicated as well.

In addition to working currents, a useful parameter for the diagnostics of the plate surface status is the measurement of *ohmic currents*, defined as the gap currents at an HV value such that no avalanche formation occurs, and thus the current measured is only due to conduction through the internal oil coating. Ohmic currents are therefore an indicator of the presence of pollutants on the plate surface, rather than of an actual damage of the surface, and are very sensitive to any problem related to the recirculation system's filters. The typical HV range for ohmic currents measurements is $5 \div 7 kV$. Figure 4.18 shows the evolution of the ohmic currents. A comparison with figure 4.17 clearly shows that ohmic currents have very small absolute values but show larger relative increases as a consequence of gas problems. For example, the effect of filter exhaustion is much bigger on the ohmic currents than on the working currents. Wrong gas mixture didn't have any

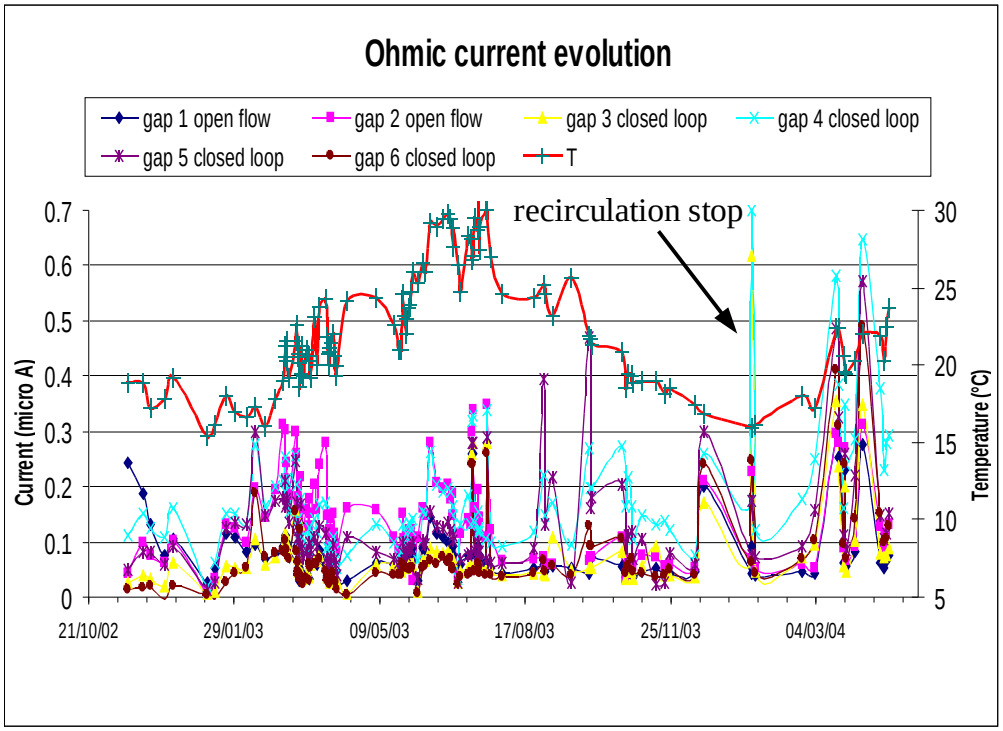

Figure 4.18: Ohmic current evolution. Gap numeration is given here starting from the nearest to the source (gap 1) to the farthest (gap 6).

influence on the ohmic currents, as expected, while a recirculation stop with no major effects on the working currents lead indeed to a high increase in the ohmic currents.

The X5/GIF test was also an important benchmark for testing suitable techniques of damage recovery. The most significant case of recovery followed an accident in which, after an integrated charge corresponding to about 7 ATLAS years (with a safety factor of 5), a malfunctioning of the recirculation system caused the suspension of the gas flow while a problem with the DCS system prevented the HV to be turned off. The result was a three days operation period *under full irradiation* with no gas flow. As a consequence, the chambers showed a very high increase in both ohmic and working currents which prevented the chambers from

reaching full efficiency under full irradiation. At closed source, however, chamber performace was still satisfactory. Figures 4.19 and 4.20 show the increase in working and ohmic currents respectively, during the gas flow suspension.

The recovery procedure consisted in the following steps:

- the chambers were fluxed with pure Argon at 3 volumes/hour for about five weeks, and a sensitive decrease of the gap currents was observed. Nevertheless, the noise level at the working point was still too high to allow efficient operation of the chambers under full irradiation, being still ohmic and working currents greater than their normal values by a factor 3.

- for the following two months the chambers were fluxed with an isobutane enriched mixture ($C_2H_2F_4/i\text{–}C_4H_{10}/SF_6 = 84.7/15/0.3$), keeping their HV at a low value ($7kV$). The decision to increase the isobutane concentration is based on the observation, made in previous tests, about the strong effect of isobutane in recovering a damaged plate surface. Indeed, during the operation with the new mixture both ohmic and working currents returned to their normal values, as shown in figure 4.21, where the values of the currents are plotted as a function of time. For clarity, only the measurements taken at the same temperature are shown.

Figure 4.22 shows the rate versus efficiency plot for Station 1, gap 1, φ, compared with results obtained before the accident. The data were taken with full irradiation. The entity of the damage is evident from the plot: the counting rate increases rapidly when approaching the working point. For some chambers this increase was so rapid that with full irradiation the working point could not be reached at all. The effectiveness of the isobutane treatment is evident form the results obtained after the recovery procedure, which are plotted in the same figure.

4.7 Conclusions

The measurements performed at X5-GIF on three ATLAS production RPCs provided important information on the ageing effects of the gas gaps. As known from previous tests [24], the plate resistivity increased significantly at the beginning of the test, mainly due to the dry environment. Once the relative humidity of the experimental area has been put under control and set around ~50%, the resistivity showed a significant decrease. The performance of all tested chambers remains much above the ATLAS requirements. Indeed, after an integrated charge

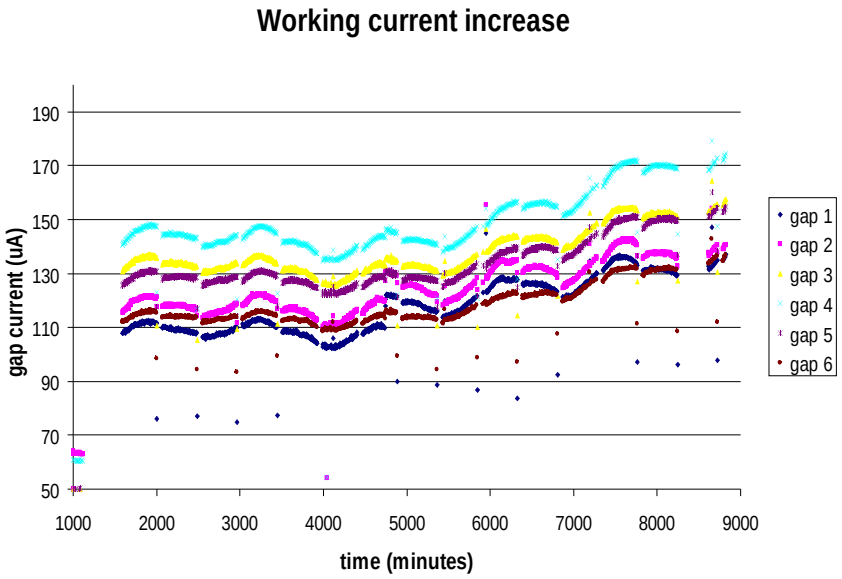

Figure 4.19: Working current increase. Gap numeration is given here starting from the nearest to the source (gap 1) to the farthest (gap 6).

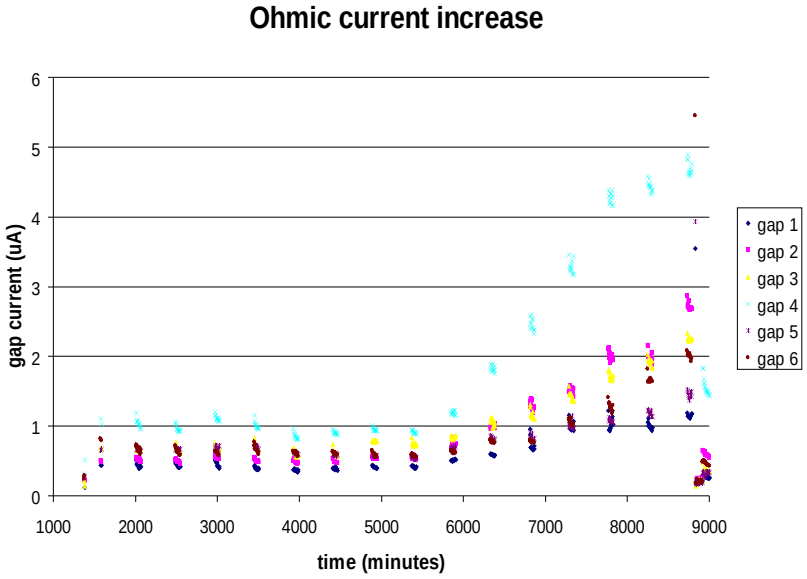

Figure 4.20: Ohmic current increase. Currents are measured here at $7kV$. Gap numeration is given here starting from the nearest to the source (gap 1) to the farthest (gap 6).

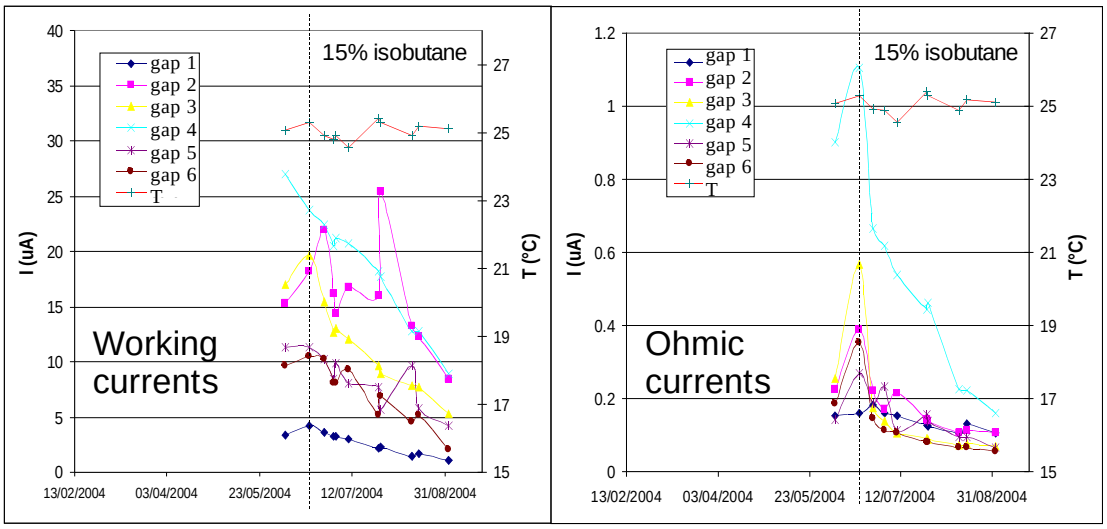

Figure 4.21: Gap current isotherms. The values of ohmic and gap current of the six gaps are plotted as a function of time. Only measurements taken at the same temperature are plotted.

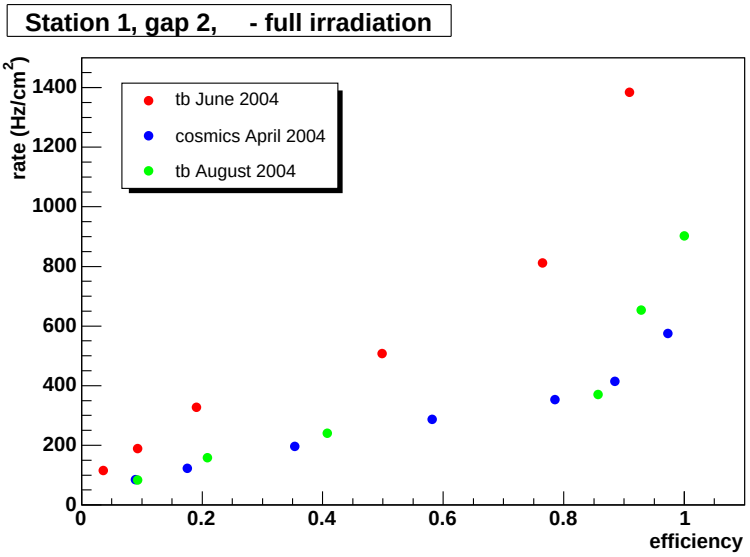

Figure 4.22: Rate versus efficiency plot for Station 1, gap 2, φ. Data before (April 2004) and after (June 2004) the accident are compared. The results of the recovery procedure (August 2004) are also shown.

corresponding to 7 ATLAS years (i.e. $\sim 210 mC/cm^2$, including a safety factor of 5) all the gaps under test showed a very good detection efficiency even at fully opened source, with a counting rate of about $600 Hz/cm^2$.

Both ohmic and closed source working currents were used to monitor the quality of the internal plate surface. Any problem related to the gas system has shown to generate an increase on both currents. In particular, the increase on the ohmic currents was proven to be a very early and safe indicator of gas poisoning. These increases were completely reversible, provided that the gas flow and composition were promptly restored to correct values.

The present gas recirculation system has been proven to be (so far at the level of ~4 ATLAS years of ageing, i.e. $\sim 120 mC/cm^2$) adequate to ATLAS, provided that the filters are properly maintained and changed when necessary.

Damage recovery procedures such as Argon fluxing and low voltage operation with isobutane-enriched mixtures were successfully applied after a critical stop of the gas system which caused major damages to the internal plate surface. ATLAS RPCs have thus shown to be robust enough to tolerate extremely harmful events, on the condition that proper recovery techniques are applied.

Chapter 5

F^- production in RPCs

As already discussed in 3.3, the gas mixture has a crucial role in the operation of RPCs. Most of the RPCs operated in avalanche mode today use as their primary gas component the tetra-fluor-ethane $C_2H_2F_4$ (in the following: TFE). This gas has been shown to allow good avalanche operation, in particular when associated to a small amount of SF_6 [9]. The main disadvantage of using TFE is due to its high content of Fluorine. During an avalanche, it is in general possible that a certain amount of TFE molecules gets broken, thus releasing in the gas other F compounds, such as HF.

Being F one of the most aggressive elements in nature, the presence of F^- ions on the plate surface is dangerous for the integrity of the surface itself. For this reason a significant effort has been made in order to obtain accurate measurements of the F^- production rate in RPCs. In particular, the dependence of the production rate on the operating voltage and on the gas mixture has been investigated.

In this chapter the main results are presented.

5.1 F^- concentration measurement

In this section we present a short overview of the theory and the practical aspects involved in the measurement of F^- concentration.

5.1.1 Chemical Potentiometry

An ion-selective electrode may be defined as an indicator with a relatively high degree of specificity for a single ion or class of ions. It is used in conjunction with a reference electrode, which is defined as an electrode with a potential independent

of the composition of the solution. If a measuring electrode M, and a reference electrode R are placed in a solution with ion activity a_i (to which M is sensitive), the potential E of the resulting cell is given by the Nerst equation

$$E = E^0 + \frac{2.3RT}{nF} log a_i \tag{5.1}$$

where E^0 is a constant for the particular cell at a standard temperature of 25°C, R is the gas constant, T is the absolute temperature, F is the Faraday constant, a_i is the *activity* of the ion being measured. The integer n is related to the number of electrons gained or lost in the electrode reaction, and therefore has a sign associated with it. In many cases, n may simply be described as the valence of the ion being measured.

In the case of a fluoride electrode, equation 5.1 can be expressed (in mV at 25°C) as

$$E = E^0 - 59.16 log a_{F^-} \tag{5.2}$$

5.1.2 Activity and concentration

Analytical composition information may be desired either in terms of the ionic activity, a_i, of equation 5.1, or in terms of the analytical concentration, C_i, as determined by many classically used analytical chemistry procedures.

As already discussed, electrodes and chemical potentiometry perform direct measurement of the ionic activity of a given ion or class of ion in a certain solution. Nevertheless, properly planned ion-selective measurements can provide information on both activity and concentration. The relation between activity and concentration is given by

$$a_i = \gamma_i C_i \tag{5.3}$$

where γ_i is the single ion activity coefficient, which can be derived both theoretically and empirically. In dilute solutions γ_i is frequently close to unity, thus allowing to interchangeably use activity and concentration in equation 5.1. However, in the chemical solutions involved in most analytical problems, γ_i differs significantly from unity. It is principally a function of the ionic strength of the solution, I, defined as

$$I = \frac{1}{2} \sum_i C_i z_i^2 \tag{5.4}$$

where z_i is the charge of an ion. The Debye-Hückel equation gives the correlation between single ion activity concentration and the ionic strength of a solution:

$$-log\gamma_i = \frac{AZ_i^2\sqrt{I}}{1 + B\sqrt{I}} \tag{5.5}$$

where A and B are constants.

5.1.3 Free and total ion concentration

One more important factor which may make the observed ion activity less than the total ion concentration is the tendency for ions in solutions to associate with other ions, to form undissociated molecules. Examples of this kind of reaction are the formation of weak acids, weak bases, insoluble precipitates and complex molecules or ions.

As an example, hydrofluoric acid, HF, is a weak acid and is slightly dissociated

$$HF \leftrightarrow H^+ + F^- \tag{5.6}$$

and obeys the following equilibrium expression

$$K_a = \frac{a_{H^+}a_{F^-}}{a_{HF}} = \frac{a_{H^+}\gamma_{F^-}C_{F^-}}{\gamma_{HF}C_{HF}} \tag{5.7}$$

being K_a the dissociation constant for hydrofluoric acid, and using equation 5.3. Solving for the concentration of the fluoride ion, we obtain

$$C_{F^-} = \frac{a_{F^-}}{\gamma_{F^-}} = \frac{1}{a_{H^+}}\frac{\gamma_{HF}}{\gamma_{F^-}}C_{HF}K_a \tag{5.8}$$

Equation 5.8 shows that measurements of fluoride ion activity can indeed be used to determine the fluoride ion concentration, even in presence of ion recombination, *if* the *p*H and the activity coefficients are adjusted to optimum and constant values.

TISAB (Total Ionic Strength Adjustment Buffer) is widely used in fluoride concentration measurements in order to adjust the conditions of fluoride analysis as defined in equation 5.8. Typical TISAB composition is shown in table 5.1.3.

5.2 Experimental setup

The experimental setup is schematically shown in figure 5.1. A small size RPC ($20\times20cm^2$) operated in streamer mode is irradiated by a photon flux created

Sodium chloride	1.0 M
Acetate acid	0.25 M
Sodium acetate	0.75 M
Sodium citrate	0.001 M
pH	5.0
Ionic strength	1.75 M

Table 5.1: Typical composition of TISAB

by a ^{60}Co source. The output gas from the chamber flows through the TISAB target solution, which gathers F^- ions. The concentration of F^- in the target solution is continuously monitored by a selective fluoride probe. Using a small RPC operating in streamer mode has two main advantages:

- streamer mode operation, together with the high rate induced by the source, produce a strong F^- signal,
- thanks to the small size of the chamber, it is possible to obtain a high number of volume changes per hour (thus minimizing the accumulation of F^- on the chamber surface) while using a small flux (thus maximizing the target capture efficiency).

5.2.1 Measurement technique

The chamber is fluxed with a binary mixture of TFE and isobutane. Fractions of isobutane from 0% to 30% have been used. The F^- probe is calibrated using NaF solutions with concentrations of 0.1,1,10 and 100 $\mu g/ml$. The probe does not show a linear response as a function of $log[NaF]$ over the whole concentration range. For this reason only the three highest points in concentration are fitted with a linear function, while the first and second are connected by a second degree polynomial. The global fitting function is required to be continuous, with its first derivative continuous, over the whole concentration range.

Figure 5.2 shows a typical calibration curve.

Before starting the measurement, the probe is put in the TISAB target, with no gas flowing through it, until it reaches a stable point. This procedure allows to easily spot any pollution of the target solution which could invalidate the measurement.

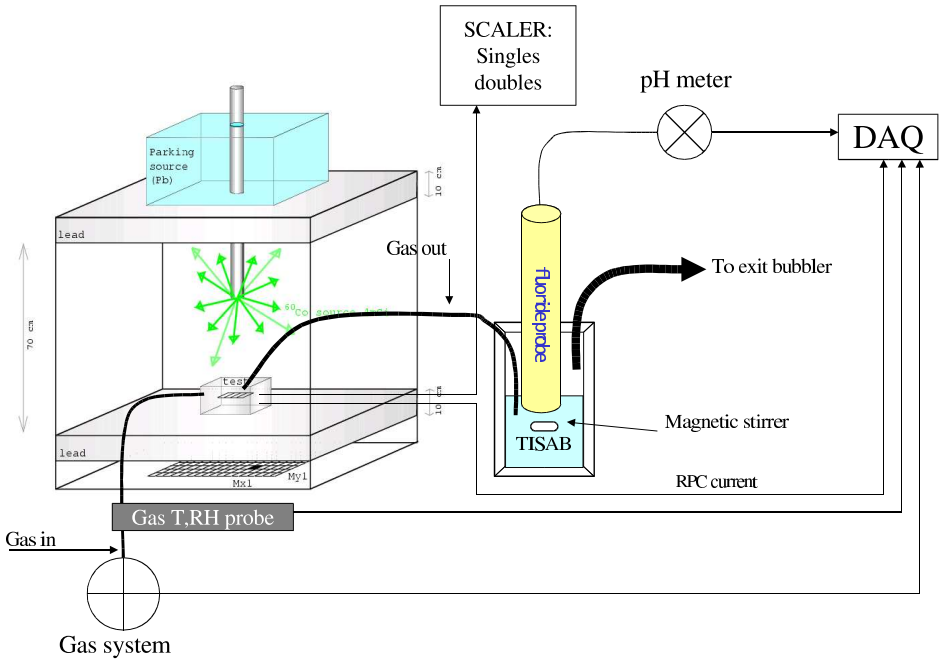

Figure 5.1: Experimental setup for F^- production rate measurement

At this point the chamber is turned on and its output gas sent through the TISAB target. The response of the probe is read out continuously by a dedicated DAQ program. The duration of a typical measurement is of the order of some hours, depending on the operating voltage of the chamber.

After about 24 hours of operation, the chamber is fluxed with pure Ar or pure isobutane. This procedure allows to remove the F^- ions which got captured by the inner surfaces. The output gas is sent through the TISAB target and the extraction rate is measured.

The results of a typical measurement are shown in figure 5.3, where the quantity of F^- gathered in the TISAB target is plotted as a function of time. The effect of an increase of the isobutane concentration during the measurement, is also clearly visible. The behavior is linear, and the corresponding slopes (i.e. the F^- production rates) are indicated.

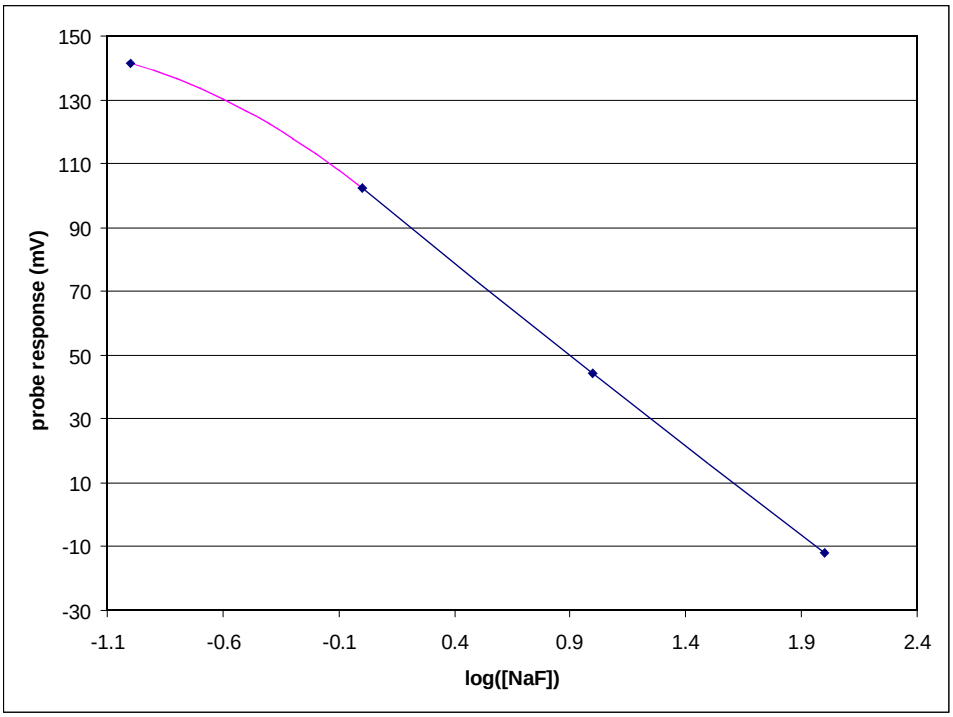

Figure 5.2: F^- probe calibration curve

5.3 Dependence of the F^- production rate on the isobutane concentration

It has long been known that RPCs operated with fluoride compound gases show better performaces in terms of long time operation when the concentration of isobutane in the gas mixture is increased. Being the production of F^- one of the causes of ageing in RPCs, it should be expected that the presence of isobutane can somehow influence the F^- production and accumulation inside the chamber.

In order to test this hypothesis, the F^- production rate has been measured by operating the chamber with different gas mixtures. A chamber operating in streamer mode fluxed with a binary (TFE/isobutane) mixture has been used for these measurements. The results are shown in figure 5.4.

The main consideration which can be done is that at constant total gas flow, the F^- production rate decreases when the isobutane percentage is increased. The data clearly exclude that this decrease is due only to the decrease in concentration of TFE, which in this mixture is the only F^- source. Indeed, when decreasing the TFE concentration from 95% to 80% (i.e. increasing the isobutane from 5% to

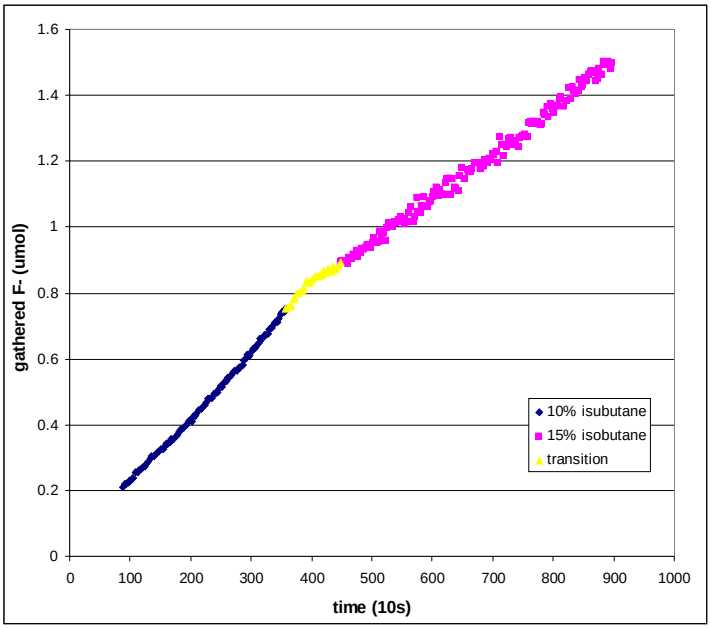

Figure 5.3: Typical F^- production measurement. In this case, the isobutane concentration has been increased during the measurement. The values of the production rates are shown as well.

20%), the F^- production rate is found to decrease by a factor between 3 and 4.

However, it should also be noted that the F^- production rate is somehow dependent on the gas flow. In particular, at constant isobutane concentration, the observed F^- rate is higher when the flow is higher. The difference is greater at lower isobutane concentrations, i.e. at higher F^- production rates. This last observation calls for a systematic study of the dependence of the F^- production rate from the total gas flow. Such a study has been performed, and the results will be presented in section 5.4.

The exact reasons of the influence of the isobutane are still to be understood, but two hypothesis can be done:

- the F^- production is somehow mediated by UV photons. Being the isobutane a quenching gas, its role in this case would be of *production inhibitor*.
- F^- ions can react with isobutane molecules and produce stable compounds. Since the electrode is only sensitive to F in its ionic form, such a reaction would indeed reduce the observed F^- rate. In this case the isobutane would just to *capture and neutralize* the F^- ions, rather than influencing their production.

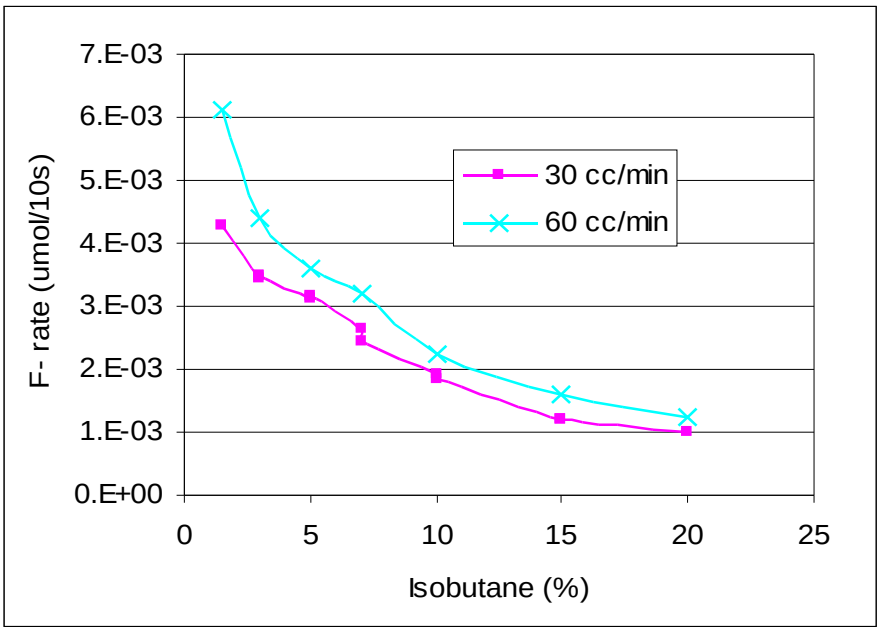

Figure 5.4: F^- production rate as a function of isobutane concentration for two different total gas fluxes

5.4 The effect of the gas flow in F^- production and accumulation

As discussed in section 5.3, the F^- production rate is found to be dependent on the gas flow at which the chamber is operated. In order to investigate this effect, a specific set of measurements was carried on.

The F^- rate measured by the electrode is indeed due to the combination of different effects:

- the actual production of F^- ions in the gas
- the partial accumulation of the ions on the internal surfaces of the plates

Some measurements of the accumulation process can be easily performed. We define the *attachment rate* as the difference between the rate of the actual production inside the chamber and the rate which is measured by the electrode. Whatever the exact chemical reactions involved in the attachment are, some preliminary considerations can be done:

- the attachment rate is likely to be inversely proportional to the gas flow

- it is reasonable to suppose that the attachment rate is proportional to the production rate itself.

In order to study the attachment rate, two identical chambers were serially connected to the same gas line, with the downstream one turned off. The upstream one was on the contrary operated at working point and the F^- rate was measured both at the exit of the first chamber and at the exit of the second chamber. The difference between the two rates is a measurement of the attachment rate in the second chamber. Under the hypothesis that the two chambers behave in the same way for what concerns the F^- attachment, this measure allows to estimate what the attachment in the first chamber is, and thus to calculate the real production rate.

The isobutane concentration in gas mixture and the operating current have been fixed at 10% and $10\mu A$ respectively, and the total gas flow has been set to different values, in the range $5 \div 60 cc/min$. Being ϕ_1 the F^- rate measured after the first chamber and ϕ_2 the F^- rate measured after the second chamber, the the *absorption factor* is defined as

$$A = \frac{\phi_1 - \phi_2}{\phi_1} \tag{5.9}$$

and represents the fraction of F^- which is entrapped inside the second chamber. Figure 5.5 shows the absorption factors measured as a function of the total gas flow. Remarkably the observed behavior *is not inversely proportional to the gas flow*, as clearly shown in figure 5.6, where the same data are plotted as a function of the inverse of the gas flow. The reason of this behavior is still to be understood.

Once the absorption factor has been measured, it is possible to correct the value of ϕ_1 in order to account for the fluorine ions attached into the first chamber. The corrected values, shown in figure 5.7 as a function of the total gas flow, are substantially in agreement with the hyposthesis of a constant F^- production.

As already discussed in section 5.2.1, the chambers used for the tests presented in this chapter were periodically fluxed with pure Ar, in order to remove the fluorine ions from the inner surface of the plates. Figure 5.8 show the F^- concentration in the target solution as a function of time for a chamber fluxed with pure Ar at $100 cc/min$. The current driven by the gap operated in Ar has been switched from 0 to $10\mu A$, thus causing an increase of the extraction rate by a factor 20. The dependence of the extraction rate in pure Ar on the operating current

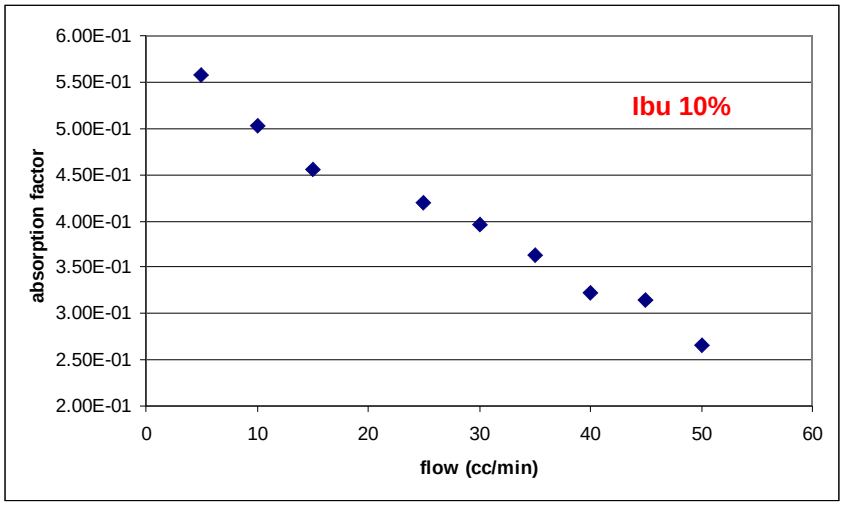

Figure 5.5: F^- absorption factor as a function of the gas flow.

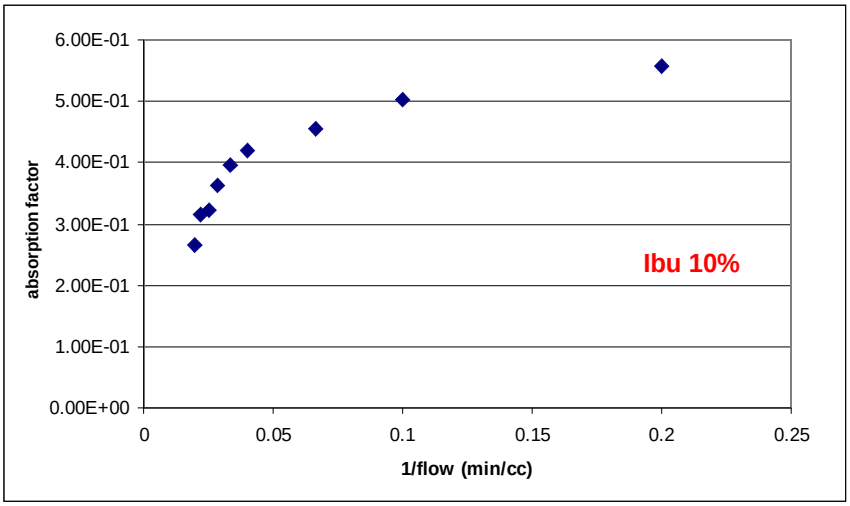

Figure 5.6: F^- absorption factor as a function of the inverse of the gas flow.

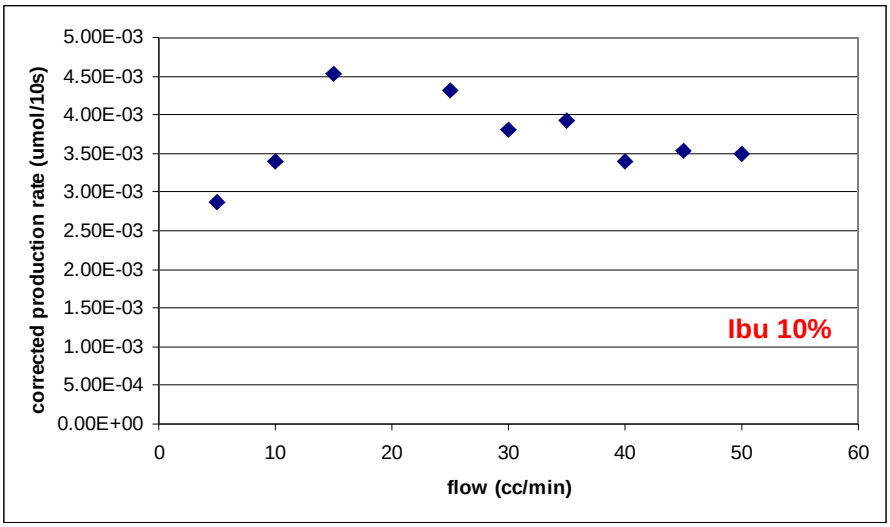

Figure 5.7: F^- production rate corrected using the measured absorption factor, as a function of the total gas flow.

has been found indeed to be linear (in the region above $2\mu A$), as shown in figure 5.9.

5.5 F^- production as a function of the working current: avalanche and streamer working regimes

A clear knowledge of the exact dependence of the F^- production on the working current is of course needed for any long term use of RPCs, in which the operating voltage needs to be chosen in order to minimize any ageing effect due to F^- pollution. Moreover, as discussed in section 3.4 RPCs can be operated, by a proper choice of the gas mixture and operating voltage, in two different regimes: *avalanche* and *streamer*. The study of the F^- production for each regime is of great interest, being for example the streamers characterized by the abundance of UV photons, which is not true for avalanches. Therefore any difference in the production rate between avalanches and streamers can in principle give information on the actual F^- production mechanism.

A dedicated set of measurements has been performed in order to investigate the abovementioned problems. The F^- production rate has been measured for RPCs operated with binary and ternary mixtures, thus working in streamer and avalanche mode respectively. The exact composition of each mixture is shown in

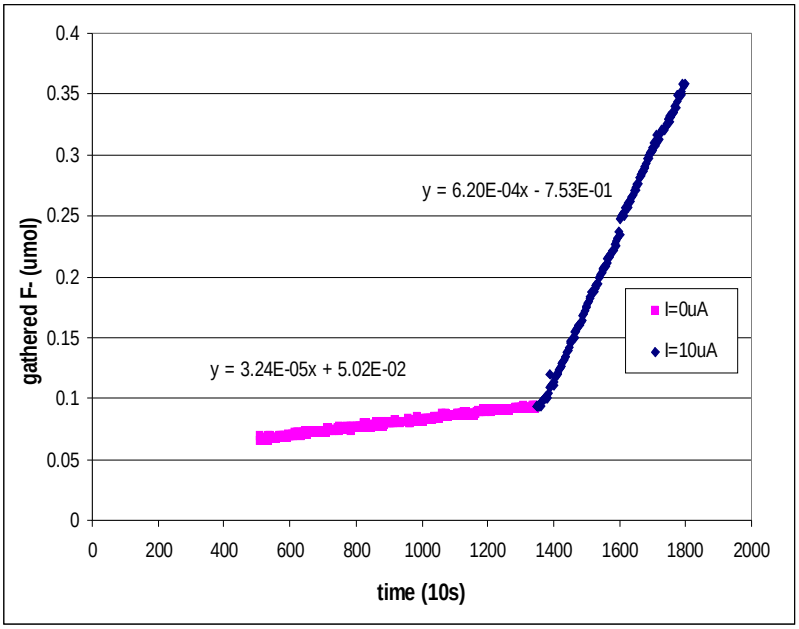

Figure 5.8: Argon fluxing procedure. The effect of the current driven by the gap is shown.

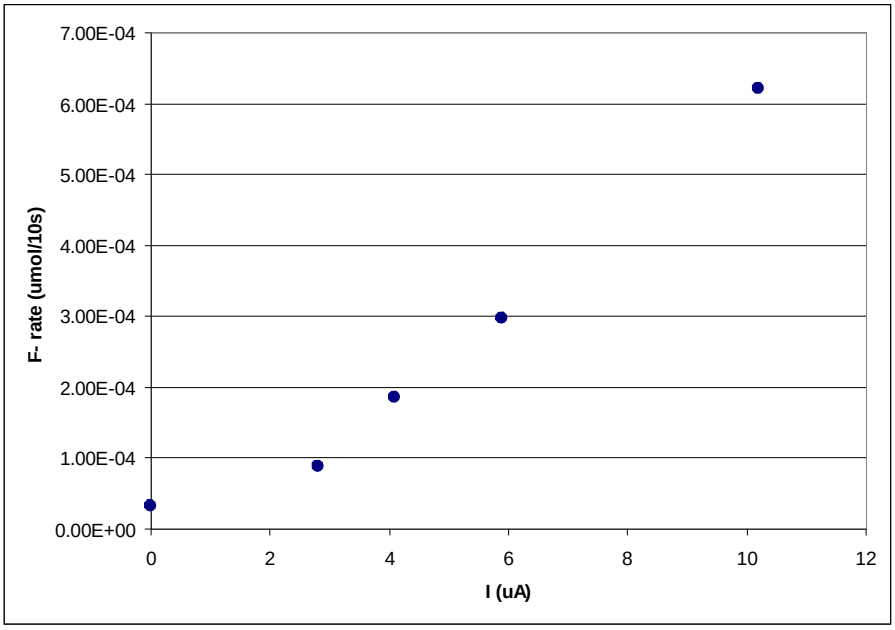

Figure 5.9: F^- extraction rate obtained with pure Ar, as a function of the operating current.

table 5.2. For each mixture, two different measurements of the F^- production rate as a function of the working current were done:

mixture	components	composition
binary	$C_2H_2F_4/i$–C_4H_{10}	90/10
tertiary	$C_2H_2F_4/i$–C_4H_{10}/SF_6	89.5/10/0.5

Table 5.2: Gas mixtures used for avalanche vs streamer comparisons

- measurement at constant source irradiation, in which the current was increased by increasing the operating voltage of the chamber
- measurement at constant working point, in which the current variation is obtained increasing the irradiation rate (i.e. reducing the distance between the source and the chamber). In this case the operating voltage was adjusted in order to compensate the voltage drop across the plates due to the current driven by the gap, thus maintaining a constant working point.

The results are shown in figure 5.10 and they clearly show the following effects:

- at low working currents ($<4\mu A$) the chamber behaves always in the same way, with no dependence on the gas mixture and the operating regime
- at higher working currents the binary mixture shows an effect of saturation of the F^- production rate in spite of the increasing operating current
- the ternary mixture shows a behavior similar to the binary one when kept at constant working point, while the plateau disappears if the operating voltage is increased under constant irradiation, in correspondence with the formation of streamers in the gas. In these conditions, the F^- production rate appears to rapidly increase when the operating voltage is increased.

In the ternary gas mixture there are indeed two sources of fluorine ions: $C_2H_2F_4$ and SF_6. The behavior of the chamber with ternary mixture operated at voltages above its optimal working point allows to conclude that at normal operating voltages the only significant contribution to the F^- production rate is due to the $C_2H_2F_4$. In fact in this region the binary and ternary mixtures produce the same amount of fluorine ions. On the other hand, the presence of SF_6 determines an

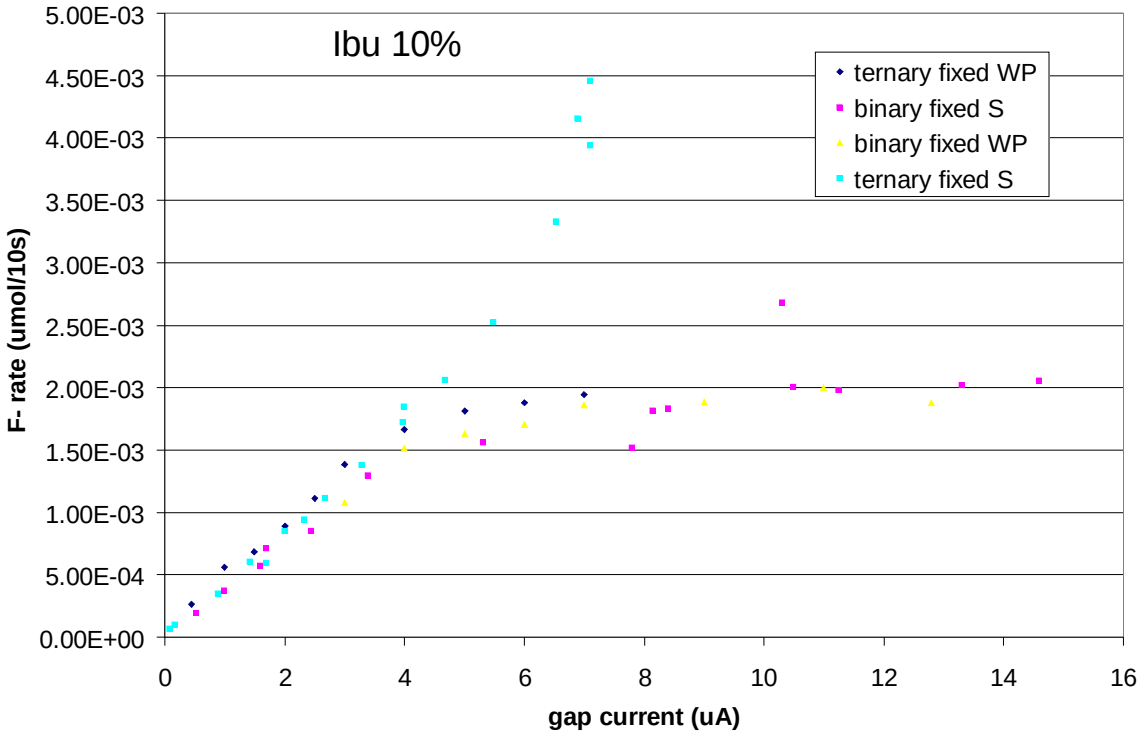

Figure 5.10: F^- production rate as a function of the working currents with different gas mixtures and operating regimes.

increase of the F^- production rate when the HV is increased above the working point, i.e. when the chamber is operated in streamer.

The exact reasons of the presence of the plateau in the F^- production rate as a function of the operating current is still to be understood. However the fact that, at fixed working point, the curves obtained in streamer and avalanche mode are comparable, leads to the conclusion that, whatever the F^- production mechanism is, it is not mediated by UV photons, which are much more abundant in streamers with respect to avalanches.

5.6 Conclusions

The measurements presented in this chapter, while still not allowing a complete comprehension of the F^- production mechanisms in RPCs, can be used to draw some conclusions of great practical interest:

- the isobutane concentration has a crucial role in the production of fluorine

ions, and thus in the ageing of the detector. In particular, higher concentrations have proven to be very effective in reducing the observed F^- production rate.

- the gas flow, on the other hand, has been shown to be an important parameter to reduce the deposit of F^- ions on the inner surface of the gap.
- fluxing the chambers with pure Ar is an effective procedure for removing F^- residuals from the inner surface of the plates. This effect is amplified when the current driven by the gas is different from zero.
- the SF_6, which is fundamental to operate the RPCs in avalanche mode, is on the other hand a major source of F^- ions when operated in streamer mode, in spite of its low concentration.

Chapter 6

RPC simulation in the ATLAS offline framework using the Geant4 toolkit

Simulation has a crucial role in high energy physics. It is indeed widely used for:

- the design of the experimental setup and the evaluation of its discovery potential;
- the development, test and optimization of the analysis and reconstruction tools;
- the measurement of physical quantities such as cross sections.

The simulation toolkit most widely used in the high energy physics community has been for a long time Geant3. It has been continuously developed for 15 years, but its last version (Geant3.2.1) has been released on March 1994 and is written in FORTRAN. It has been used not only in high energy physics simulations, but also in nuclear physics, and in the development of medical applications. One of the disadvantages of Geant3 is the lack of a native implementation of the simulation of the hadronic processes, for which it relies on external packages.

6.1 The Geant4 Toolkit

Geant4 is a completely new toolkit, rather than a new release of Geant3. It is based on an object oriented architecture, implemented using C++. It is in con-

tinuous development, and among its features there is a native implementation of hadronic physics.

The Object Oriented approach ensures code maintainability along the number of years foreseen for LHC experiment. Moreover, the implementation of physical processes has been designed to be highly modular, thus allowing for the easy insertion of new processes.

The core components of the toolkit are known as the Geant4 *kernel*. The kernel is responsible for the simulation, i.e. it completely manages the run, taking care of all the operations needed for the propagation in the simulated detector of the particles generated in each event. In order to carry out all its tasks, the kernel needs to know from the user:

- a geometrical description of the volumes in which the particles will be propagated, together with an accurate description of the materials each volume is made of;
- the list of the physical processes to be simulated for each kind of particle;
- a mechanism to generate the primary vertices of the events to be simulated.

A detailed description of the kernel internals is beyond the scope of this chapter, and can be found in [25] and in the Geant4 documentation, freely available on the Geant4 official web site.

Hit production in Geant4 is provided by *Sensitive Detectors*. If a certain volume described in the geometry is supposed to generate signals when crossed by some kind of particle, it must be associated to a properly implemented Sensitive Detector, which is an instance of a class different from the one describing the "real" geometry (*tracking geometry* in the following). The clear separation between Sensitive Detectors and Geometry classes allows to easily decouple the description of the tracking geometry from the one of the readout geometry. Each time a particle trajectory crosses a volume which can generate hits, the kernel is responsible for calling the corresponding Sensitive Detector, which implements the hit generation algorithms. Hence, the Sensitive Detector generates a list of hits, which are stored for further processing.

The `RPCSensitiveDetector` class has been implemented to provide the generation mechanism for hits generated in the barrel trigger chambers.

6.2 ATHENA: the ATLAS offline framework

ATHENA [26] is a control framework based on the GAUDI architecture originally developed by the LHCb experiment. This architecture has been extended through collaboration with ATLAS, and an experiment neutral implementation, also called GAUDI, has been created. Athena is the result of this kernel framework, together with ATLAS-specific enhancements, such as the event data model and event generator framework. The collaboration between LHCb and ATLAS is in the process of being extended to allow other experiments to also contribute new architectural concepts and concrete implementations to the kernel GAUDI framework.

It is intended that almost all software used in physics, whether for event generation, reconstruction or analysis, will be in the form of specializations of a few specific components, where specialization means adding functionalities to a standard component while keeping its interface the same. Within the application framework this is done by deriving new classes from one of the base classes: `DataObject, Algorithm, Converter`. Anything which has as its origin a concept such as hit, point, vector, trajectory, i.e. a clear quantity-like entity should be implemented by deriving a class from the `DataObject` base class. On the other hand anything which is essentially a procedure , i.e. a set of rules for performing transformations on more data-like objects, or for creating new data-like objects should be designed as a class derived from the `Algorithm` base class.

The role of an algorithm is to take input data, manipulate it and produce new output data. In general, an algorithm will be configurable: it will require certain parameters, such as cut-offs, upper limits on the number of iterations, convergence criteria, etc., to be initialized before the algorithm may be executed. These parameters may be specified at run time via *job options* files.

In ATHENA data objects produced by Algorithms are posted to a common area in memory from where other modules can access them and produce new data objects. The Transient Data Store (TDS) is the mechanism to provide such a common area in the Gaudi architecture: an Algorithm creates a data object and post it into the TDS, thus allowing other Algorithms to access it. Once an object is posted into the store, the TDS takes ownership of it and manages its lifetime according to preset policies, removing, for example, a TrackCollection when a new event is read. StoreGate (SG) is the ATLAS implementation of the TDS. It manages the data objects in transient form, as well as their transient/persistent conversion.

6.3 ATLAS Muon digitization

The Muon Digitization software packages have been completely re-written to operate on Geant4 hits. It is independent of the Geant4 detector simulation, and runs within the ATHENA framework. The Muon Digitization consists of four algorithms, one for each muon technology (XXX_Digitization packages, where XXX = MDT, RPC, TGC, CSC). It provides the production of collections of simulated muon digits out of muon hit collections from the Geant4 simulation, where both the input and the output objects are assumed to be in SG. In the present architecture, muon digits are converted to Raw Data Objects (RDOs) or to byte streams before undergoing the persistent storage. RDOs are the output of the readout electronic, thus are the constituents of the byte stream.

The goal of the muon digitization is to simulate the output signal of the muon detector in ATLAS given the output of the Geant4 detector simulation. The digitization process consists of two steps: in first, the output of the detector simulation, henceworth refereed to as Geant4 hits, is converted to muon digits. In the second step, the muon digits are converted to RDO from which the byte stream (the electronic output) is obtained. The muon digits are objects that can be fed directly in the muon reconstruction, thus are known as Reconstruction Input Objects (RIO). The muon off-line reconstruction dataflow starts from the raw data, the byte stream. The byte stream is read into the TDS as transient RDO data objects. In a subsequent steps, the RDO are converted into RIO (digits and or clusters), through calibration services, pedestal and noise handling, etc. The step RDO→RIO is where the raw data is “prepared” before being fed into the off-line reconstruction. It thus follows that the muon digitization operates in the reverse steps of the off-line reconstruction dataflow, by producing the RIO first, then the RDO (or byte stream subsequently).

6.4 RPC digitization

6.4.1 From hits to digits

RPC hits are generated by the SensitiveDetector (SD) which assigns to them a Simulation Identifier (SimID), uniquely identifying the gas gap each hit is registered in. The position of the hit in the reference system of the gas gap is also stored, together with the time from the beginning of the event, i.e. the time of flight of the particle generating the hit. RPC hits are represented in the simulation

RPCHit	RPCDigit
SimID of the gas gap	OID of the strip
Position of the hit wrt the gas gap	
Hit time (time of flight of the particle)	Global time (tof + strip propagation)

Table 6.1: The information included in RPC hits and digits

code by instances of the class `RPCHit`.

The digitization process takes care of adding to the hits the information necessary for further analysis (for example trigger algorithm simulation and track reconstruction). It translates any SimID to a Standard Offline Identifier (OID), which is used by the other ATHENA algorithms to uniquely identify RPC strips in the muon spectrometer. Using the position information provided by the hits, the digitization can properly calculate the propagation time of each electronic signal along its strip, add it to the time of flight of the hit and assign this *global time* to the digit. The information obtained is stored in a new instance of the class `RPCDigit` and posted in StoreGate for further processing. The main differences between RPC hits and digits are summarized in table 6.1

6.4.2 Cluster simulation

When a particle generates an avalanche in an RPC, charge signals are induced (and detected) on the readout strips. A set of n adjacent strips with signals is called a *cluster* of size n. In the RPC operation, due to possible signal induction on more than one strip, cluster sizes are in general greater than 1, with an average cluster size at working point typically of 1.3. The hit production mechanism provided by the ATLAS Geant4 simulation does not include a tool for proper simulation of clusters. Thus a particle generates hits on only one strip, except when secondaries (for example δ) are produced and detected by neighboring strips.

The impact point along a strip is known to influence the size of the cluster the hit will generate. Figure 6.4.2 shows for example the probability to observe a cluster of size 1 as a function of the impact point of the track along the strip. The strip pattern is also represented. The probability is normalized to the number of clusters with sizes 1 or 2, i.e. for each bin, the complement to unity gives the probability to have a cluster with size 2. From the plot it is clear that, for example, a muon crossing the region between two adjacent strips will most likely generate a cluster of size 2, whereas a track passing in the middle of one strip would induce

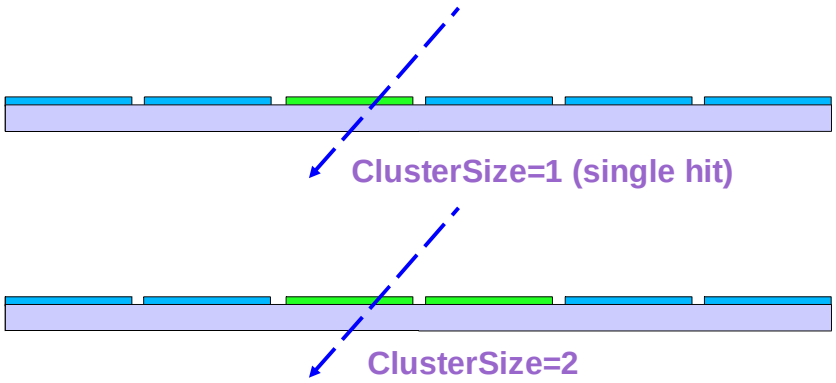

Figure 6.1: RPC clusters

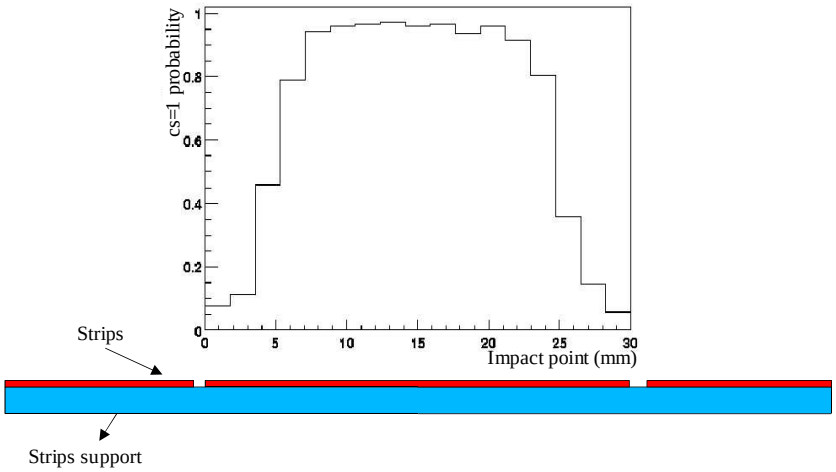

Figure 6.2: Probability to observe cluster size 1 as a function of the impact point along the strip.

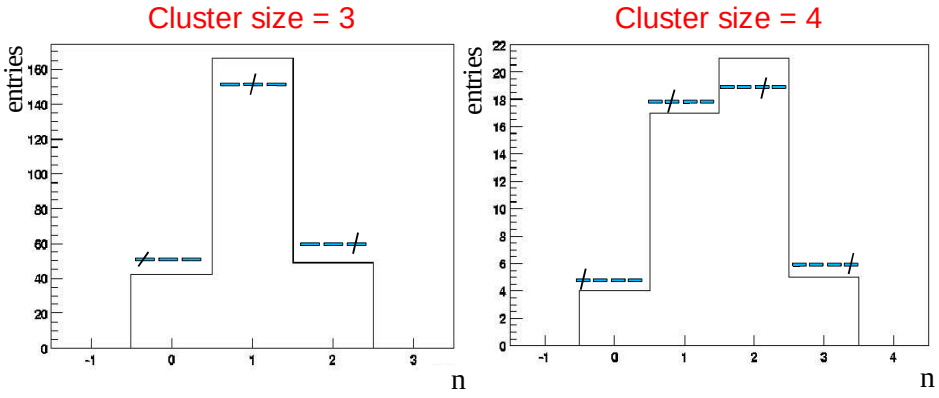

Figure 6.3: Cluster spread distributions for cluster of sizes 3 and 4.

signals on that strip only.

In a small amount of cases, clusters with sizes greater than 2 are also observed.

The digitization algorithm reproduces the observed cluster sizes by generating, when necessary, digits on strips adjacent to the one actually crossed by the particle. Cluster simulation is carried on in three steps:

1. experimental distributions are used to decide, according to the impact point of the particle along the strip, whether the cluster size will be 1 or 2.

2. experimental distributions are used to decide what the final size of the simulated cluster will be.

3. digits are created according to the results of the above steps.

Particular attention needs to be paid to the way the additional digits are created around the one actually crossed by the muon. Figure 6.4.2 shows the cluster spread distributions. For each cluster of a given size, the plots count which strip was actually crossed by the muon. Upon each bin, the corresponding track/strip configuration is showed.

These experimental distributions are hence used to properly create the extra digits.

6.5 RPC digit validation

The algorithm `RpcDigitValidation` has been implemented in order to check the correctness of the hit production and digitization processes. The validation

has been performed generating single muon events in the barrel, with no physics processes activated but transportation. For each event, the algorithm execution proceeds as described in the following:

- for each muon, its direction at the generation vertex is retrieved from the MonteCarlo information. With no physics processes activated, this direction is a good approximation of the muon trajectory.
- for each RPC digit, its distance from the muon trajectory is calculated
- for each of the three RPC layers (Middle-lowPT, Middle-Pivot, Outer), the closest digit to the muon is selected
- the fields of the OIDs of the selected digits are stored in an ntuple, together with the direction of the muon.

The resulting ntuple can be used to validate both the `RPCSensitiveDetector` and the `RPCDigitization` since it can easily spot any mistake in the generation of the SimID and in its translation to OID. For example the directions of the muons not producing any digit, or which produce digits too far from the track can be analyzed. In figure 6.4 the η and φ directions of muons not producing any RPC digits are plotted. These inefficiencies of the RPC system are concentrated, as expected, in regions not instrumented with RPCs:

- the feet of the ATLAS detector
- the ribs of the barrel magnet system
- the central ($\eta = 0$) crack
- the elevators
- the endcap regions ($|\eta| > 1$)

A similar plot has been produced for the outer stations and didn't show any abnormal inefficient region. With the same procedure, it is possible to look for digits which are created in the wrong place.

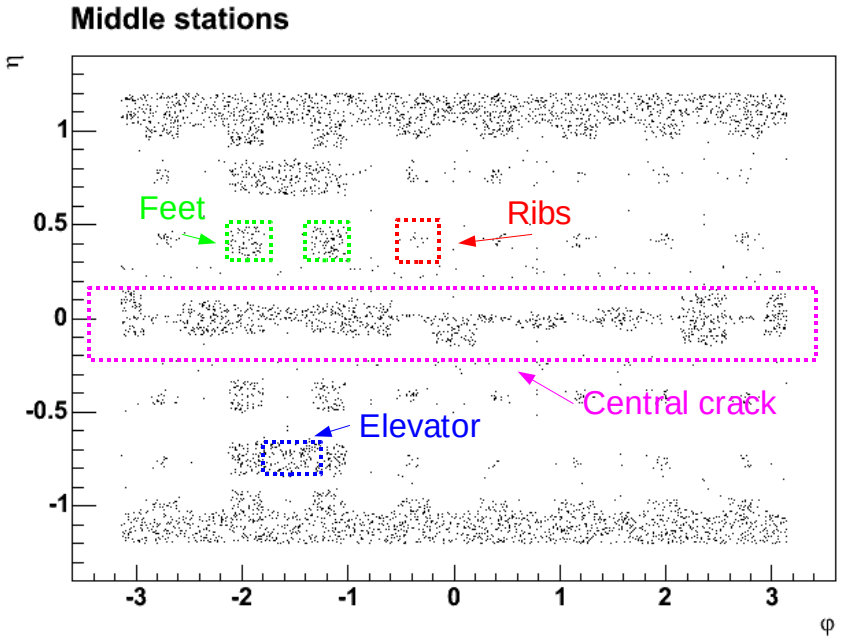

Figure 6.4: RPC digitization validation.

Chapter 7

The di-muon LVL1 trigger in the ATLAS muon spectrometer

7.1 The ATLAS LVL1 trigger implementation

A general description of the Level 1 trigger and of the muon spectrometer has been already given in chapters 1 and 2. As specialized trigger detectors, RPCs are used in the barrel part ($|\eta| < 1.05$) of the muon spectrometer, and TGCs, Thin Gap wire Chambers, in the end-cap.

RPCs are disposed in three stations, two of them (RPC1 and RPC2) cover the internal and external faces of the middle precision chamber and the third (RPC3) is located close to the external precision chamber, as shown in figure 7.1. Each station is composed of an RPC doublet with read-out in two orthogonal views, η and φ, referred as bending and non-bending projections respectively.

The barrel is divided in two half-barrels, symmetric with respect to $\eta = 0$, and azimuthally segmented in octants; each octant is further subdivided in two parts, referred as Large and Small sectors (see figure 7.2). RPC chambers are classified, according to their location, into BML (Large sectors of RPC1 and RPC2), BMS (Small sectors of RPC1 and RPC2), BOL (Large sectors of RPC3) and BOS (Small sectors of RPC3).

The trigger logic is based on coincidences between different stations, one of the inner two stations being chosen as pivot. The two innermost stations are used to trigger low-p_T muons (mainly for b-physics studies), while the outermost is used to trigger high-p_T muons.

The trigger logic is implemented through Coincidence Matrices (CM), to which

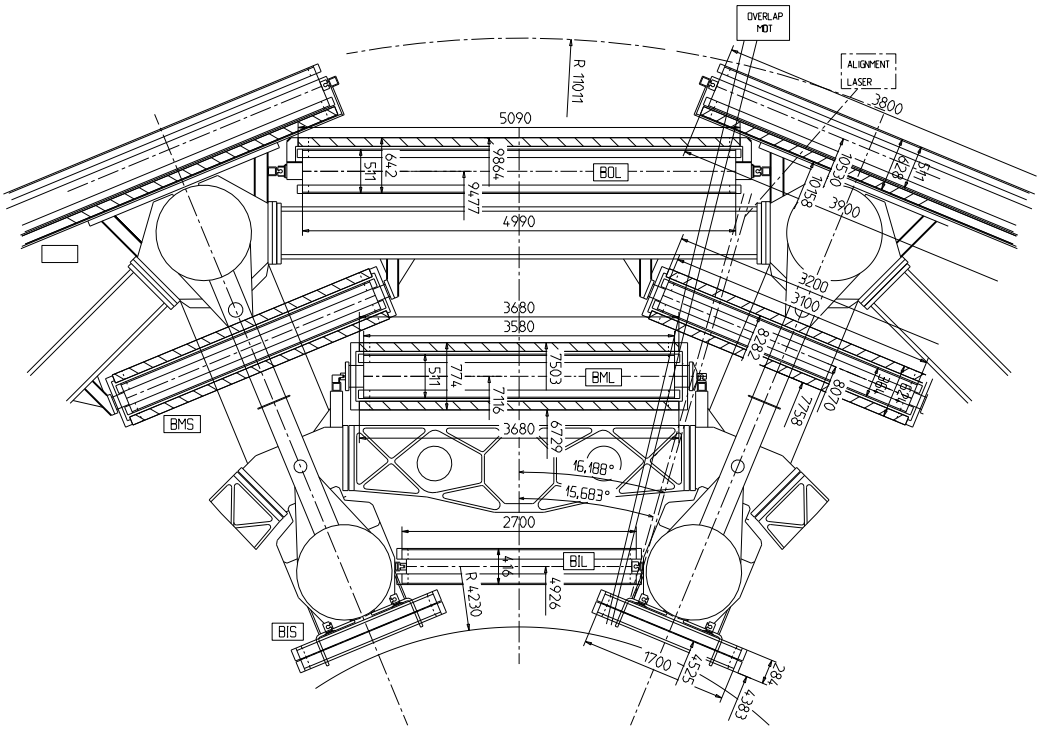

Figure 7.1: View of a standard barrel sector. The RPCs are represented by shaded boxes.

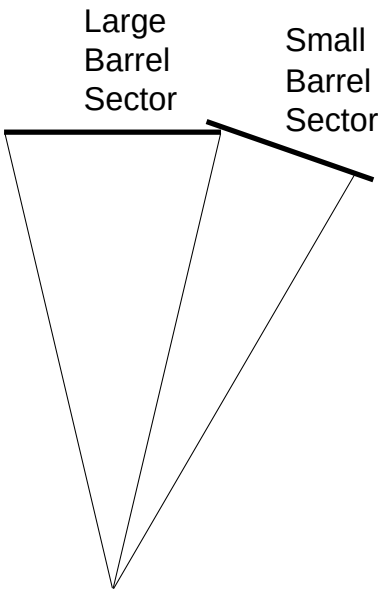

Figure 7.2: Azimuthal view of one half-barrel octant. Small units are placed in correspondence of magnet coils.

the RPC strips are connected. Four CMs, two in η and two in φ, form a Pad. The intersection of one η-CM and one φ-CM within a Pad gives a ROI (Region Of Interest) of size $\Delta\eta \times \Delta\varphi \simeq 0.1 \times 0.1$. The trigger response is given evaluating the so called Coincidence Windows, as schematically shown in figure 7.3. In the barrel, where a muon is seen to leave a hit in both of the low-p_T stations, the projective extrapolation of the hit in station 2 to station 1 can be made assuming the muon path to be a straight line (i.e. the infinite momentum approximation) with the origin at the interaction point. The distance between the extrapolated point in station 1 and the actual hit detected is defined as the separation parameter, d. In the end-cap system the low-pT trigger coincidence is made using station 3 and station 2.

The coincidence windows of the level-1 muon-trigger are designed to offer momentum discrimination by including muons above threshold and excluding those below threshold which will be bent outside the coincidence window. The p_T resolution at fixed threshold in turn is a function of the trigger detector geometry (in particular the lever arm between stations 1 and 2, and station 3), the magnetic field strength and its inhomogeneities, the Coulomb scattering in the central calorimeter and the width of the interaction region.

The sizes of the trigger windows that determine the p_T threshold have been

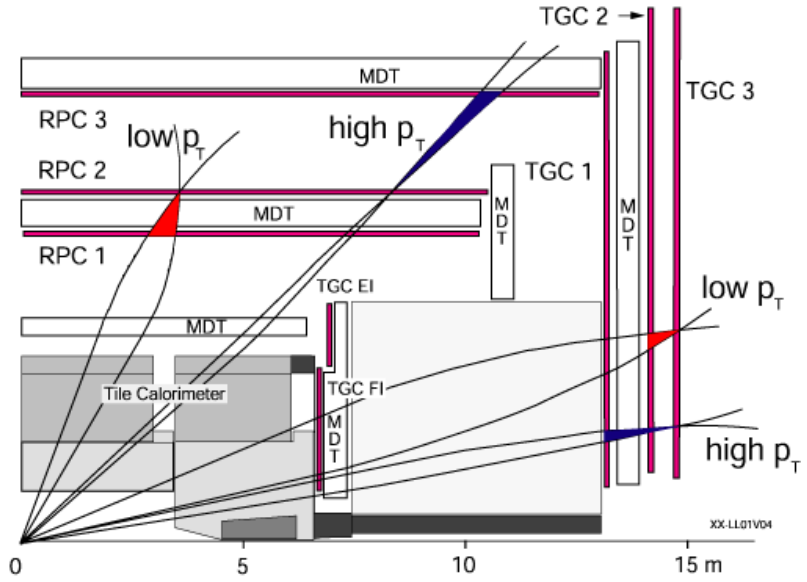

Figure 7.3: Schematic view of the coincidence-window-based muon LVL1 trigger.

computed [27] for the proposed trigger system by tracking single muons through the ATLAS detector using Monte Carlo simulation techniques. The size of a coincidence window is defined such that 90% of the muons of each charge within the detector acceptance, generated with transverse momentum equal to the threshold, are accepted.

The coincidence window is not symmetric around the extrapolated point of the infinite momentum path: muons of a given charge, bending towards high |z| regions (in the barrel) or high r regions (end-cap), cross station 1 at a distance from the extrapolated point larger than that for muons of opposite charge. This effect increases with $|\eta|$ in the barrel and with r in the end-cap. This leads to asymmetric coincidence windows, formed by independent left and right half-windows. The difference between the right and left halfwindow is 7/10 *cm* in the large/small chambers at $|\eta|$ 0.9 in the barrel and 3.5 cm at $|\eta|$ close to 1 in the end-cap. The size of each half-window is evaluated accounting for the relative trigger efficiency of positive and negative muons independently, to minimize possible effects on charge-asymmetry measurements. Figure 7.4 shows the working principle of the coincidence-windows-based ATLAS LVL1 muon trigger.

The CM board produces an output pattern containing the low-pT trigger re-

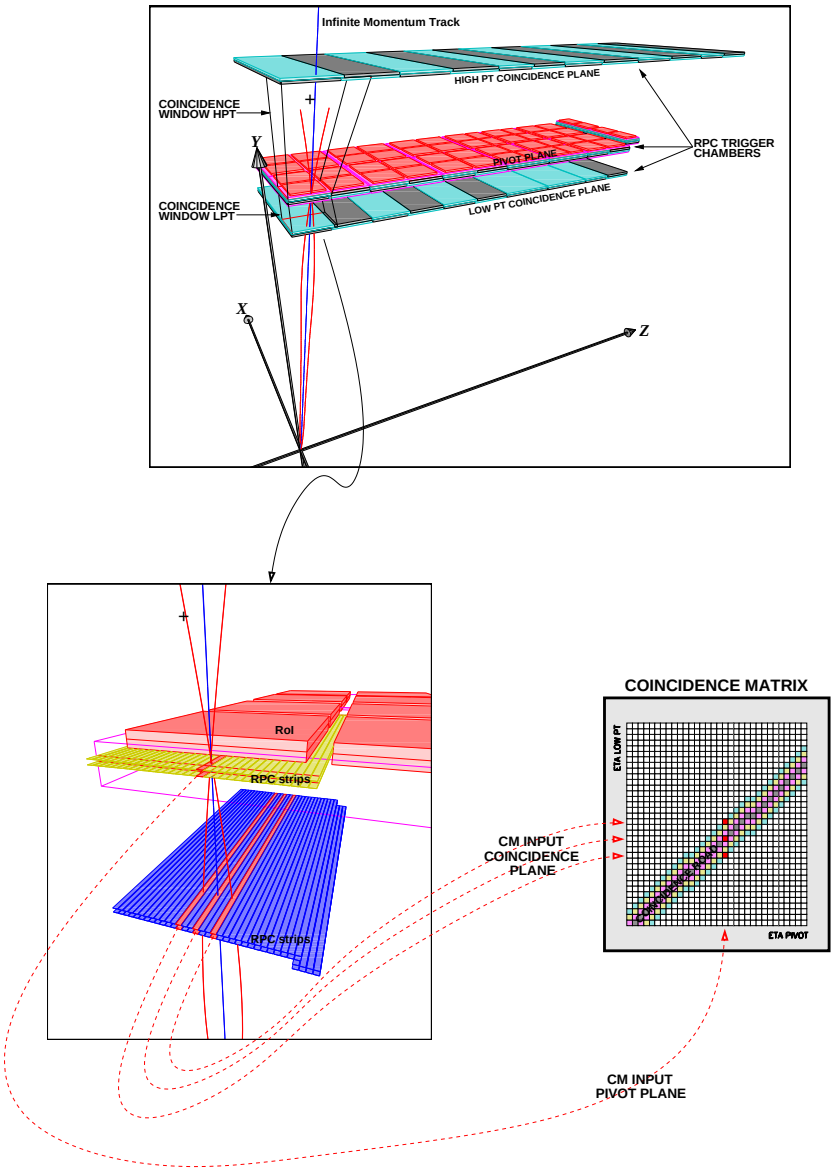

Figure 7.4: Schematic view of the coincidence-windows-based ATLAS LVL1 muon trigger

sults for each pair of RPC doublets in the η or φ projection. The information of two adjacent CM boards in the η projection, and the corresponding information of the two CM boards in the φ projection, are combined together in the low-p_T *Pad Logic* (Pad) board. The four low-p_T CM boards and the corresponding Pad board are mounted on top of the second RPC station. The high-p_T trigger logic receives as an input the hits on the third station and the output pattern of the low-p_T trigger algorithm. The low-p_T Pad board generates the low-p_T trigger result and the associated RoI information. This information is transferred, synchronously at $40MHz$, to the corresponding high-p_T Pad board, mounted on the third RPC station, that collects the overall result for low- and high-p_T.

The high-pT Pad board combines the low- and high-p_T trigger results. The combined information is sent, synchronously at $40MHz$, via optical links, to a Sector Logic (SL) board, located in the counting room. Each SL board receives inputs from seven (six) low-p_T (high-p_T) Pad boards, combining and encoding the trigger results of one of the 64 logic sectors into which the barrel trigger system is subdivided. The trigger data elaborated by the Sector Logic is sent, again synchronously at 40MHz, to the Muon Interface to the Central Trigger Processor (μCTPI), located in the same counting room.

Data are read out from both the low- and high-p_T Pad boards. These data include the RPC strip pattern and some additional information used in the LVL2 trigger. The read-out data for events accepted by the LVL1 trigger are sent asynchronously to Read-Out Drivers (RODs) located in the counting room and from here to the Read-Out Buffers (ROBs). The data links for the read-out data are independent of the ones used to transfer partial trigger results to the SL boards.

Figure 7.5 illustrates the segmentation of the LVL1 trigger system in the ATLAS barrel. In each half barrel, one physical sector is divided in two logic sectors (i.e. it is readout by two SL boards). Approximate RoI, Pad and CM dimensions are shown, as an example, for a small sector.

7.2 Rare beauty decay studies in the ATLAS detector.

In certain rare B decays, the decay products provide a distinctive signature that can be used in the LVL1 trigger. These so-called self-triggering modes include decays of the type $B_{d,s} \rightarrow \mu\mu(X)$, which involve flavor-changing neutral currents (FCNC) and are strongly suppressed in the Standard Model, with pre-

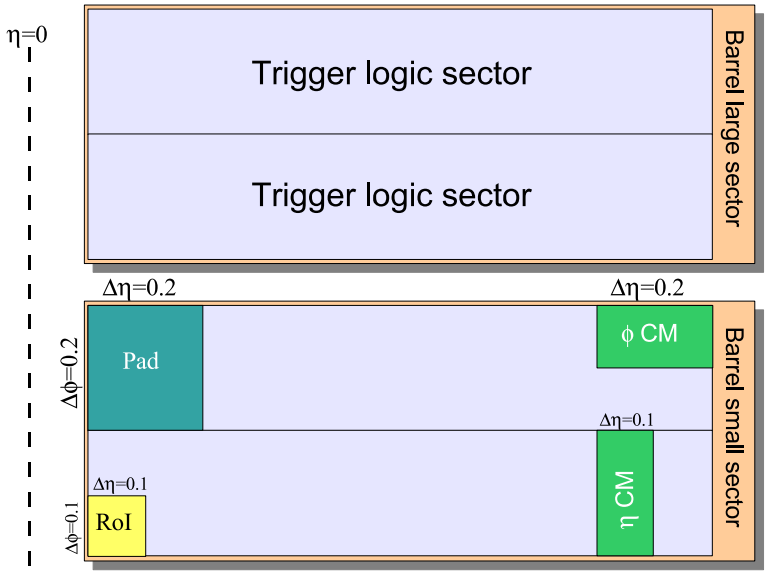

Figure 7.5: Segmentation of the LVL1 barrel trigger.

dicted branching ratios typically in the range $10^{-5} \div 10^{-10}$. The high rate of B-hadron production foreseen in ATLAS will allow a very effective study of these channels.

For the purely muonic decays, ATLAS will be sensitive to branching ratios of the order of 10^{-9} and should be able to measure the branching ratio for $B_s \to \mu\mu$ assuming the Standard Model prediction. Large-statistics samples will be collected for decays of the type $b \to (s,d)ll$ that give final states such as $B_d^0 \to K^{*0}\mu\mu$, $B_d^0 \to \rho^0\mu\mu$ and $B_s^0 \to \phi^0\mu\mu$. This will allow precise measurements to be made of the decay dynamics, as well as of the branching ratios, giving significant constraints on new physics.

These rare decay modes are forbidden at the tree level in the Standard Model, i.e. the decays involve loop diagrams, thus being highly suppressed. In non-standard models of electroweak interactions, FCNC processes can be allowed at the tree level and therefore the branching ratios of these rare decays would be higher. In addition, in the presence of new physics, additional particles may be present in the loops, thus increasing the decay probability.

In the context of Standard Model, the measurement of the branching fractions of the $B \to \mu\mu(X)$ channels is of primary interest. The measurement of the branching fractions of the decays $B_d^0 \to K^{*0}\mu\mu$ and $B_d^0 \to \rho^0\mu\mu$ allows the CKM matrix-element ratio $|V_{td}|/|V_{ts}|$ to be determined. The square of this ratio is useful

Channel	Signal	Background
$B_d^0 \to \mu\mu$	4	93
$B_s^0 \to \mu\mu$	27	93

Table 7.1: Number of expected events after three years at low luminosity ($30\,fb^{-1}$)

Channel	Signal	Background
$B_d^0 \to \mu\mu$	14	660
$B_s^0 \to \mu\mu$	92	660

Table 7.2: Number of expected events after one year at low luminosity ($100\,fb^{-1}$)

also for the estimation of the ratio of the mass differences $\Delta m_s/\Delta m_d$ in the $B_d^0 - \bar{B_d^0}$ and $B_s^0 - \bar{B_s^0}$ systems, complementary to direct measurements of the oscillation periods.

7.2.1 The channel $B_{d,s} \to \mu\mu$

As an example of the difficulties involved in the study of such rare decays, in the following some results obtained from simulated events ([3]) will be summarized.

Simulations were made with the PYTHIA event generator. The Inner-Detector response was fully simulated and the particles were reconstructed in the Inner Detector. The muon reconstruction efficiency was assumed to be 85% for the LVL1 trigger muon, and 95% for the other trigger levels. About 1500 signal events were simulated in each channel, with $p_T(\mu) > 6GeV$ and $|\eta(\mu)| < 2.5$ *for each muon*. About 9000 background events were simulated and reconstructed.

The cuts applied for signal selection are:

- Decay length of $B_0 > 0.7\ mm$
- Angle between p_T of B_0 and the line joining the primary and secondary vertices $< 1^\circ$
- Isolated muons (no charged particles in a cone of 20°)

Tables 7.1 and 7.2 ([3]) show the number of events (for both background and signal) passing the cuts.

From the results reported above, it is clear that it is crucial, in order to increase the significance of the signal for such channels, to increase the signal-to-noise ratio. The muons coming from B-physics di-muon sources are characterized by low ($< 6\ GeV$)p_T values. Figure 7.6, for example, shows the p_T distribution for

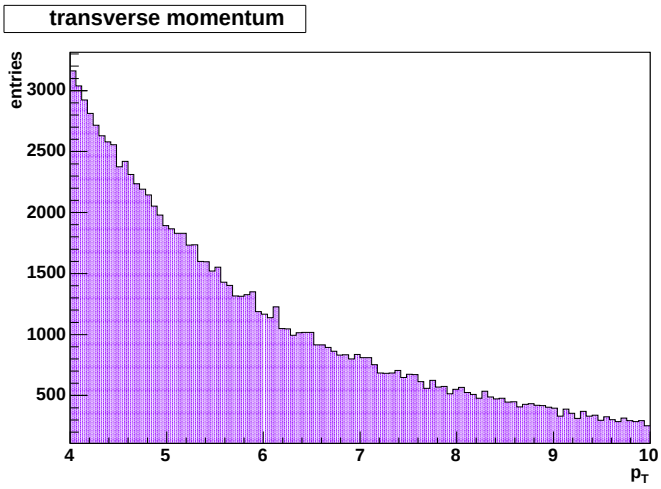

Figure 7.6: p_T distribution for muons coming from $pp \to b\bar{b} \to \mu\mu X$ processes.

muons coming from $pp \to b\bar{b} \to \mu\mu X$ processes. An enhancement of the signal could therefore be obtained reducing the LVL1 muon trigger p_T threshold. Unfortunately, this would also increase the background contamination in the selected sample. One of the possible improvements for the analysis of this kind of decays is the implementation of a di-muon trigger.

7.3 The di-muon trigger

A trigger scheme with the possibility to discriminate events with two muons has been foreseen in the ATLAS experiment, in order to increase the sensitivity of the detector to inclusive di-muon decays, which are the signature of many interesting processes, such as rare B decays. In the following, the results from a study of the di-muon trigger performace in the barrel region are presented.

7.3.1 Geometrical overlaps

In order to increase the trigger acceptance of the muon spectrometer, several regions of overlap between the trigger chambers are foreseen in the detector layout. A muon crossing one of these regions, may generate two different triggers, thus producing a false di-muon trigger. The trigger system must therefore be aware of the geometrical overlaps, in order to reject such fake double triggers.

Three kinds of geometrical overlaps are present in the barrel trigger chambers

layout:

- φ overlaps between two adjacent sectors.
- η overlaps between two CMs belonging to the same pad.
- η overlaps between two CMs belonging to adjacent pads in the same sector.

An example of the first kind of overlaps is shown in 7.7, while the layout characteristics causing the second and third overlap typologies are shown in figures 7.8 and 7.9 respectively.

In order to properly discriminate the fake double triggers, the trigger results from the CM operation can be flagged when the trigger originates from a strip in the pivot plane which is known to be in a region of geometrical overlap. The higher levels of the LVL1 trigger logic (i.e. Pad, SL and μCTPI) will afterwards take care of identify and remove from the trigger results the fake double triggers.

In more detail, the removal of the fake double triggers by different parts of the LVL1 trigger logic proceeds as follows:

- the η overlaps between two CMs belonging to the same pad are solved by the pad itself, which indeed passes to the SL only one of the triggers detected by its matrices, i.e. the one with the highest threshold.
- the η overlaps between two CMs belonging to adjacent pads in the same logic sector are solved by the SL board the pads belong to. The SL collects the triggers from all its pads, and when it finds two triggers in two adjacent pads, both with the eta overlap flag asserted, it ignores one of them.
- finally, φ overlaps between two adjacent sectors can't be solved by the barrel trigger logic, and the μCTPI is designed to deal with such overlaps. It checks the φ overlap flags of the triggers coming from the SL boards and properly removes the fake double triggers. At this stage the overlaps between the barrel and the endcap trigger systems (which will not be analyzed in this work) will also be solved.

7.3.2 Determination of the overlap flags

As discussed above, the trigger system needs to be aware of the strips which are located in geometrically overlapping regions, and hence are likely to produce fake double triggers. This information is stored in each CM configuration file.

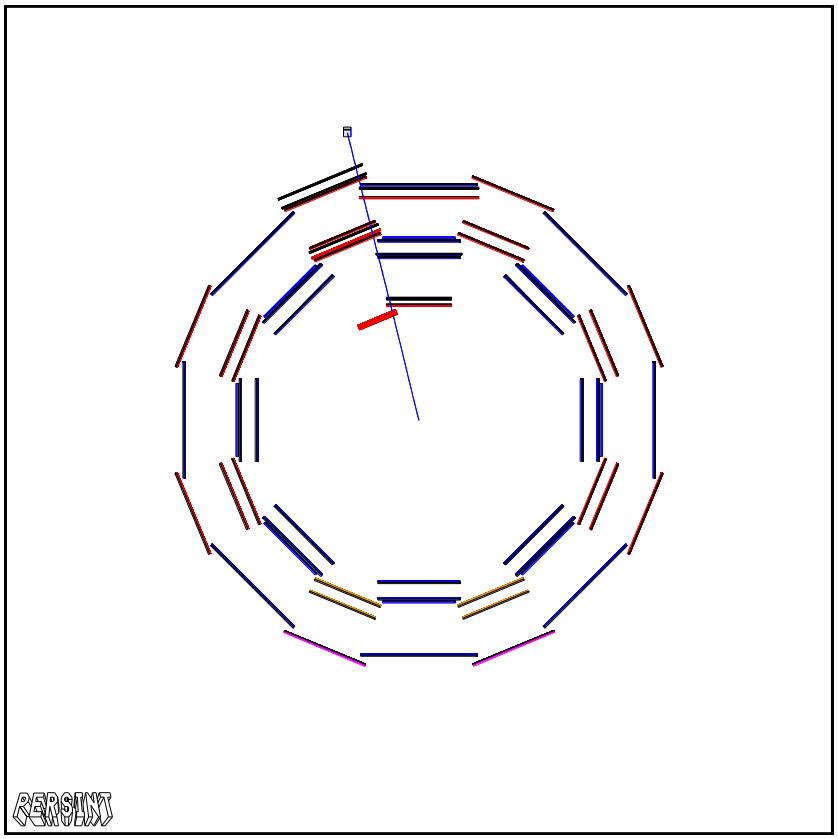

Figure 7.7: Example of a fake double trigger. Due to the geometrical overlap of the chambers along the φ direction, the muon will produce triggers in two different logic sectors.

Once the CM has been programmed, it attaches to each of its triggers the corresponding value of the overlap flag, which is used by the Pad, SL and μCTPI to properly remove double triggers. The overlap flag needs to be determined for each pivot electronic channel, thus calling for an automated procedure.

The chosen technique consisted in simulating the propagation of single-muon events through the ATLAS spectrometer. The simulated response of the trigger system was therefore analyzed in order to locate the events for which two muon triggers were generated. An automatic algorithm located all the events in which double triggers where found. For each of the pivot strips, three quantities are calculated:

1. the *double trigger probability*, defined as the fraction of double triggers given by the strip with respect to the total number of triggers in that elec-

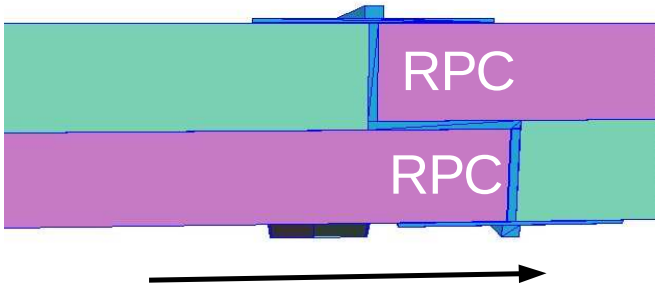

Figure 7.8: Eta overlap between two CMs in the same pad.

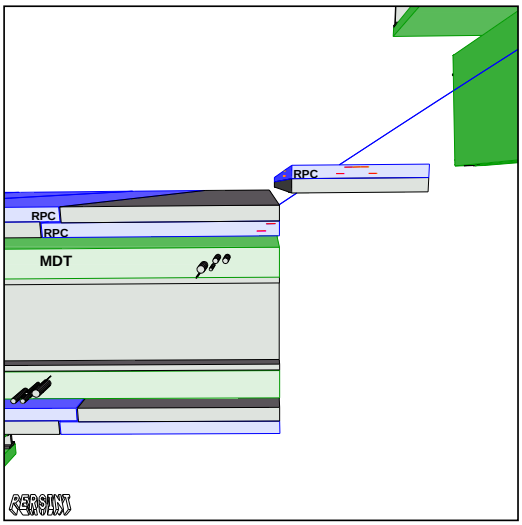

Figure 7.9: Eta overlap between two adjacent pads. A muon track such the one reported here would generate triggers on two different pads in the same sector.

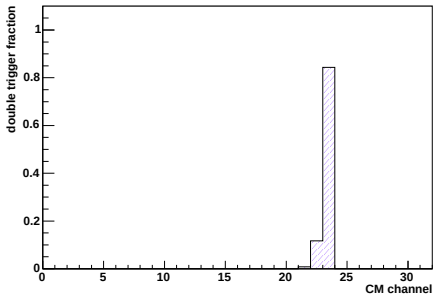

Figure 7.10: Double trigger fraction for the η CM on sector 45, address eta 2. The plot refers to overlaps inside the same pad.

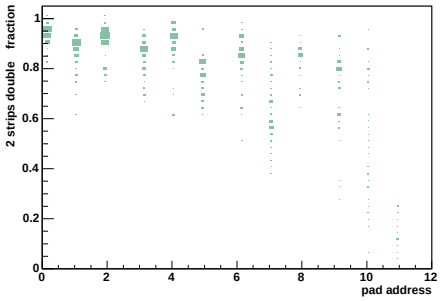

Figure 7.11: Double trigger fraction contained in the two strips nearest to the overlap region for all CMs of all the sectors under study, as a function of the address eta of the CMs, i.e., as a function of $|\eta|$. The plot refers to overlaps inside the same pad.

tronic channel.

2. the *double trigger fraction*, defined as the ratio of the double triggers found in the strip with respect to the total number of double triggers generated in the CM the strip belongs to.

3. the *double trigger contamination*, defined as the ratio of the double triggers found in the strip with respect to the total number of triggers (both single and double) generated in the CM the strip belongs to.

For the analysis were used 4 milions of single-muon events: 2 milions with muons of $6GeV$ and 2 milions with muons of $20GeV$, in order to correctly calculate the overlap flags for both low-p_T and high-p_T triggers. For each energy, the 2 milion events are equally divided in μ^+ and μ^- events so that the bending effect of the magnetic field for both the muon signs is properly considered when calculating the η overlaps. All the events were generated with η cuts so that the muons are in the barrel region. Moreover, the study has been restricted to the η>0 region.

Figure 7.10, for example, shows the double trigger fraction for all the channels of the *eta* CM on sector 45, address eta 2. It refers to double triggers due to the overlaps in the same pad. It is clear that the fake double triggers are indeed concentrated in the same region of the effective geometrical overlap. Figure 7.11

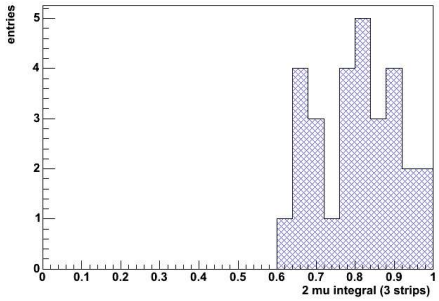

Figure 7.12: Fake double trigger fraction contained in the three strips nearest to the overlap region for all CMs of all the sectors under study. Only CMs with more than 100 entries are considered in this plot.

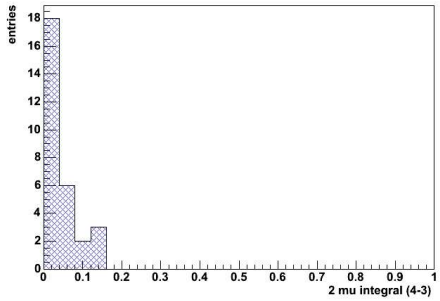

Figure 7.13: Fake double trigger fraction that is contained in the fourth strip near the three considered in 7.12

reports the sum of the double trigger fraction registered by the two strips of each CM which are the nearest to the actual overlap region, as a function of the η address of the pads the double triggers are found in. The η address increases with $|\eta|$, so this plot shows that in the forward regions of the barrel the double triggers tend to interest more than two strips, as expected.

The results obtained for the φ overlaps are shown in figures 7.12 and 7.13. As for the η overlaps, these plots show the fraction of fake double triggers registered in the strips adjacent to the actual geometrical overlap. In particular, figure 7.12 shows that in the majority of the CMs, a fraction of fake double triggers greater than 80% is registered in just three strips, while figure 7.13 shows that typically adding a fourth strip to the three considered in figure 7.12 does not produce a great increase in the fraction of fake double trigger.

The φ fake double triggers were found to be 3.4% of the total φ triggers; this ratio decreases to 1.5% when calculated for the η projection.

Studying the results obtained from the fake double trigger analysis presented above, the following rules for the assignment of the overlap flags to the readout channels has been followed:

- as already discussed, the η overlaps between two CMs belonging to the same pad does not require any flag to be set;

- for the η overlaps between adjacent pads, 7 strips are flagged in the regions

of the spectrometer illustrated in figure 7.9;

- for the φ overlaps, 3 strips are flagged; if they don't account for at least 80% of the fake double triggers in their CM, a fourth strip is added only if it brings the fraction of fake double triggers above 80%

7.3.3 Performance study

Two tests have been performed to evaluate the impact of the overlap flags determined as described above on the performances of the LVL1 muon trigger:

- a single muon sample is used to check the proper removal of the fake double triggers
- a di-muon sample is used to check the amount of real double triggers that are lost due to the overlap removing mechanism.

In addition to the algorithm used to determine the overlap flags, which analyzes the LVL1 trigger results looking for fake double triggers, a dedicated algorithm simulating the overlap solving functions of the μCTPI, has been developed.

These algorithms, applied on the LVL1 simulation results obtained for single muon events, showed that 22% of the fake double triggers was still not removed by the overlap solving routine. This is exactly what can be expected, considering the fact that the overlap flags were chosen in order to eliminate ~80% of the fake double triggers.

The data sample used for the di-muon test are $pp- > J/\psi(\mu\mu)X$ events with thresholds on the p_T of the two muons for the J/ϕ decay set to 6 and 3 GeV. The MonteCarlo information has been used to select the events according to the following criteria:

- the event must present in the final state two muons with p_T>6GeV (muons with lowest p_T would not be triggered anyway)
- both the muons must be in the barrel acceptance range ($|\eta| < 1$)
- the muons must be close to each other in space ($\Delta\varphi < 0.1$ and $\Delta\eta < 0.1$). A double trigger indeed can be lost only in the case both the muons go through the same overlap region.

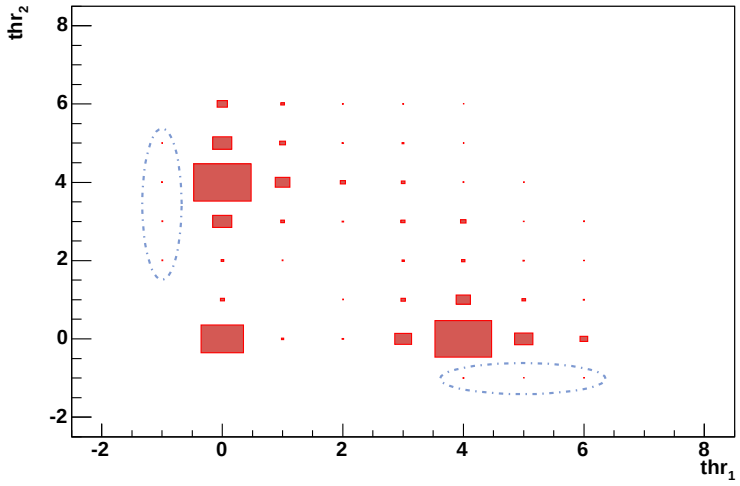

Figure 7.14: Trigger thresholds of di-muon events passing the selection criteria. The ellipses show the cases in which one of the two triggers is considered "fake" by the overlap solving algorithm. The values of 1, 2, 3, 4, 5, 6 reported on the axes correspond to the p_T values of 6, 8, 10, 11, 20 and 40GeV respectively.

In addition to these cuts, in order to consider only clean events, the presence of only two triggers (both with threshold different from 0) is required. The thresholds of the triggers are plotted, one vs the other, in figure 7.15. The value -1 is assigned by the overlap solving routine to the threshold of those triggers it has removed because of the overlap flags: such triggers are indicated by two ellipses in the figure. The fraction of real double triggers which are lost due to the presence of the overlap flags is therefore 0.58% of the total events, and it raises to 2.2% if we consider only the events in which both the muons gave triggers with non zero threshold.

A similar analysis has been also performed on $B \rightarrow \mu\mu$ events, the only difference being that no constraint on the angular separation between the two muons has been put, thus allowing to evaluate the global amount of events that are not properly triggered. The results are shown in figure 7.14. One of the two muons is wrongly considered fake only in the 0.4% of the events giving two triggers.

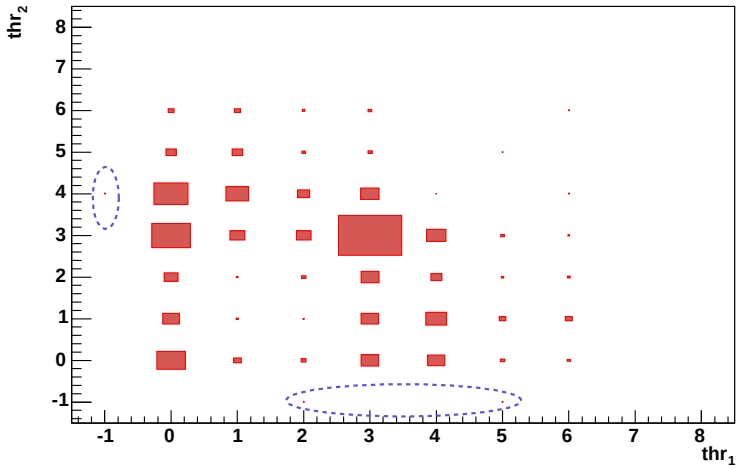

Figure 7.15: Trigger thresholds of $B \rightarrow \mu\mu$ events passing the selection criteria. The ellipses show the cases in which one of the two triggers is considered "fake" by the overlap solving algorithm. The values of 1, 2, 3, 4, 5, 6 reported on the axes correspond to the p_T values of 6, 8, 10, 11, 20 and 40GeV respectively.

7.4 Conclusions

The overlap solving mechanism of the ATLAS LVL1 muon trigger has been for the first time intensively tested with the final detector layout.

The overlap flags, needed by the trigger logic to properly handle fake double triggers due to geometrical overlap of the trigger detectors, have been determined on a strip-by-strip basis by an automated procedure. In the case of φ overlaps between adjacent sectors, it has been shown that about 80% of the fake double triggers occur in the three strips nearest to the overlap region.

A $pp- > J/\psi(\mu\mu)X$ sample has been used to evaluate the fraction of real double triggers which is lost due to the overlap solving logic. This fraction has been measured to be 0.58% of the selected events, raising to 2.2% if only events with both the triggers above threshold are considered.

A study performed on a $B \rightarrow \mu\mu$ sample showed that one of the two muons is wrongly considered fake only in the 0.4% of the events giving two triggers.

Bibliography

[1] "The Large Hadron Collider - Conceptual Design", CERN/AC/95-05

[2] ATLAS Muon Collaboration; “ATLAS Muon Spectrometer Technical Design Report”, CERN/LHCC 97-22.

[3] ATLAS Collaboration; “Detector and Physics Performance Technical Design Report”, CERN/LHCC 99-14/15.

[4] W. Blum; ATLAS internal note MUON-NO-24 (1993).

[5] Detector Physics Group, ATLAS internal note MUON-NO-98 (1995).

[6] K. Nagai; “Thin Gap Chambers in ATLAS”, Nucl. Instrum. Methods A 384(1996) 219.

[7] ATLAS Collaboration; “ATLAS First-Level Trigger Technical Design Report”, CERN/LHCC 97-22 (1998).

[8] R. Santonico and R. Cardarelli; “Development of Resistive plate counters”,*NIM, Nuclear Instruments and Methods in physiscs research* **187** (1981).

[9] P. Camarri et al.; “Streamer suppression with SF_6 in RPCs operated in avalanche mode”, *NIM, Nuclear Instruments and Methods in physiscs research* **A414** (1998).

[10] R. Cardarelli et al.; “Avalanche and streamer mode operation of resistive plate chambers”, *NIM, Nuclear Instruments and Methods in physics research* **A382** (1996).

[11] R. Cardarelli, A. Di Ciaccio, R. Santonico; “Performance of a resistive plate chamber operating with pure CF_3Br,*NIM, Nuclear Instruments and Methods in physiscs research* **333** (1993).

[12] M. Abbrescia et al.; “Resistive plate chambers working at high rate”, *NIM, Nuclear Instruments and Methods in physiscs research* **B44** (1995).

[13] C. Bacci et al.; “Test of a resistive plate chamber operating with low gas amplification at high intensity beams”, *NIM, Nuclear Instruments and Methods in physiscs research* **A352** (1995).

[14] R. Santonico; “Topics in resistive plate chambers ”, *‘Third International Workshop on Resistive Plate Chambers and related detectors’ on SCIENTIFICA ACTA Quaderni del dottorato (Universita’ degli studi di Pavia* **vol IX** (15 maggio 1996).

[15] A. Ferrari and P. Sala; *ATLAS Internal Note* **MUON-NO-162** (1997).

[16] M. Angelone et al.; “Test of a resistive plate chamber under irradiation of photons and neutrons”, *NIM, Nuclear Instruments and Methods in physics research* **A355** (1995).

[17] S. Altieri et al.; “Gamma sensitivity simulation of Resistive Plate Chambers”, *Fourth International Workshop on Resistive Plate Chamber and related detectors 1999 (Bari).*

[18] S. Agosteo et al.; “A facility for the test of large area muon chambers at high rate”, CERN-EP-2000-031, February 16th, 2000.

[19] E. Gennari et al.; “32 channel TDC VME board - User’s Manual”, http://sunset.roma2.infn.it/tdc/tdcboard.ps.

[20] G. Aielli et al.; "Electrical conduction properties of phenolic-melaminic laminates", *Seventh International Workshop on Resistive Plate Chamber and related detectors 2003 (Clermont-Ferrand).*

[21] G. Aielli et al.; "RPC ageing studies"; Proceedings of VCI 2001, *NIM, Nuclear Instruments and Methods in physiscs research* **A478** (2002) 271-276.

[22] G. Aielli et al.; "Further advances in aging studies for RPCs"; *NIM, Nuclear Instruments and Methods in physiscs research* **A518** (2003) 335-341.

[23] G. Aielli; Ph.D. thesis, University of Rome Tor Vergata, February 2001.

[24] G. Aielli et al.; “Performance of a large size RPC, equipped with the final ATLAS front-end electronics, at X5-GIF facility”, *NIM, Nuclear Instruments and Methods in physiscs research* **A456** (2000) 77.

[25] S. Agostinelli, J. Allison, K. Amako, J. Apostolakis, H. Araujo, P. Arce, M. Asai, D. Axen, S. Banerjee, G. Barrand et al.; "Geant4 - A Simulation Toolkit", Nuclear Instruments and Methods A 506 (2003) 250-303

[26] "ATHENA Developer Guide", http://atlas.web.cern.ch/Atlas/GROUPS/SOFTWARE/OO/architecture/General/Documentation/ AthenaDeveloperGuide-8.0.0-draft.pdf

[27] F. Conventi; "The Simulation of the Level-1 muon trigger at LHC", PhD Thesis

[28] M. Virchaux, D. Pomarède; "Persint Manual", http://atlasinfo.cern.ch/Atlas/GROUPS/MUON/ persint/Persint_manual.pdf

Aknowledgements

I would like to express my gratitude to Rinaldo Santonico, for his constant presence during these years of work, and for having introduced me to the research on Resistive Plate Chambers. I am also grateful to Anna Di Ciaccio, who followed me during my activities in the ATLAS software group, and patiently corrected the first drafts of this manuscript. For some of the results reported in this thesis I have to thank Roberto Cardarelli's intuitions and help.

Special thanks are due to Giulio Aielli, Barbara Liberti and Paolo Camarri, for their precious collaboration and friedship in the last three years.

I am also thankful to Luigi Di Stante, Enrico Pastori, Emiliano Paoletti, Luigi Pasquali and to all the technical staff of the INFN-Roma2 ATLAS laboratories for reminding me, with their precious work, of how many things I am just not able to do.

The work on the Geant4 simulation of the ATLAS RPCs has been made easier and pleasant by the collaboration with Adele Rimoldi and Daniela Rebuzzi, to whom I owe my gratitude.

For my work on the ATLAS LVL1 di-muon trigger, I profited from the experience, suggestions and practical help of Leandro Nisati and Alessandro Di Mattia.

Finally my gratefulness goes to my family and my friends, for their love, friendship and patient support.